The violin: A review of timbre and a finite difference model for bending plate waves

Gaurish Dahoe

Bsc Thesis in Mathematical Physics

TU Delft

The violin: A review of timbre and finite difference method for bending plate waves

Graduation thesis for the double bachelor applied mathematics applied physics, submitted to department of mathematical physics at Delft University of Technology

Author
Gaurish Dahoe
(5006791)

Report

August 1, 2023

Supervisor applied mathematics:	Dr. B.J. Meulenbroek
Supervisor applied physics:	Dr. ir. D.J. Verschuur
Committee member applied mathematics:	Dr. B. van den Dries
Committee member applied physics:	Dr. A.F. Otte


TU Delft
Delft
University of
Technology

Cover image by Pyrkosz (2013)

Abstract

Each violin generates a unique sound with a distinct set of acoustic properties. In particular, the Stradivarius violins are said to have a very unique sound. The ultimate goal of this thesis is to aid in recreating the unique sound of the Stradivarius. Though, the field of research surrounding the violin and its acoustic properties is very broad and many aspects of this research, such as subtle structural differences between violins, fall beyond the scope of this thesis. Rather, the goal of this thesis is to provide the tools to find the differences between different violins.

This thesis is split into two parts. In the first part, a literature review, describing the different parts of the violin, is presented along with an overview of different experiments and finite element models, describing the plate dynamics of the violin. In the second part, a model of the violin is devised, with modelling cycles based on consecutive simplification, and implemented in *Python* using finite difference equations and the method of lines. This model is made with the goal to provide a framework for creating a realistic model of the violin where differences in timbre between violins can shown.

In the literature review, four subjects are addressed. First, an explanation on timbre is given with an illustration of its perception. Additionally the timbre of historical and contemporary violins is compared. Second, the radiated sound of the violin is discussed. In specific, the problem with directivity of radiation is brought to attention. Third, an overview of the bridge is given with a strong emphasis on the influence of the bridge admittance on the radiated sound. Last, the corpus is dissected into different parts which are investigated with optical sensors and modelled with the software packages *Comsol* and *Abaqus*.

The model in the second part of the thesis is based on principle of consecutive simplification. To set the groundwork for further iterations of the model, the most important assumptions are kept track off. The method of lines is then used to simulate the vibrations of a wooden square plate using the flexural wave equation as the governing equation of motion. In this simulation, the forward Euler method is used for the numerical time integration.

The steady state solutions of the numerical model are coherent with the analytical solutions to the flexural wave equation. However, the time dependent results diverge from the results shown in the literature study. This is either due numerical time integration method being unstable or due to the physical properties of the wood not being translated by the Stiffness matrix in the model.

Contents

1 Introduction

Either through actively listening or by having music play in the background; everywhere we go, the chances are that music is playing. We might even say that constantly listening to music has become mainstream. This is no coincidence, as people have many different reasons for listening to music. People of all ages, ranging from 8 to 85 years of age, have reported listening to music for a number of reasons: for mood regulation, for self awareness and even to distract themselves from boredom[2, 3]. One may find similar results in their own experience. However, the psychological effects from (background) music reach further than we might realise. An example is the background music in advertisements and stores, which have been shown to influence the consumers cognitive processes, behaviour and ultimately the perception of product brands[4, 5]. These findings are coherent with more general research[6, 7, 8] which suggests that changes in concentration, short term memory and emotions, can be observed when people are exposed to different styles of music.

In specific, when the effects of classical music and modern music were investigated, a discord was found between the two types of music where modern music proves to be significantly more disruptive[9, 10, 11]. The level disruption from hearing music, in these studies, while working or studying is higher when participants of studies listen to music that they particularly like or dislike. Additionally, the level of disruption also increased when vocals were present in the music. Thus, it is apparent that the styles of music influence ones behaviour and cognitive processes differently from one another. There are many more papers on the effects on different styles of music. Though, hardly any papers on the relation between music and cognitive processes consider the harmony in an ensemble caused by the more subtle yet one of the most important characteristics of the sound; the timbre or the 'colour' of the sound produced by different instruments.

Given an ensemble, its timbre will be classified by the timbre of each instrument in the ensemble. However, the effects of timbre and the contrast between different instruments with specific sound colours is largely unknown. To this end, we have to investigate the timbre of each individual instrument. In this thesis, we will focus on the string family, and on the violin in particular, as this is one of the major parts in an orchestra. One specific kind of violin is said to stand out in the string family for its unique sound: the Stradivarius violin. The Stradivarius violins, made by Antonio Stradivarius in the late 17th century and the beginning of the 18th century, are often cited being the best violins obtainable for its extreme timbre and pristine sound. The reputation of the instrument is thus far also reflected in its market value.

Beyond music, understanding the impact of the environment on the properties of waves and their respective harmonics has many applications such as music recognition[12], acoustics in buildings such as theatres[13] and it could even be used for underwater acoustics[14]. Yet, the range of applications does not stop at phonons and can be used for many forms of signal practises.

Timbre provides a good starting point for acoustic interferometry since music is a well known and studied subject of signal transmitting and receiving. On top of this, timbre offers an intuitive look into the physics of waves which other disciplines in the field might not have or might have in lesser degree.

Therefore, keeping both the advances into acoustic interferometry and the cognitive processes as a consequence of background music in mind, the ultimate goal of this research will be to inspect the timbre of the Stradivarius in comparison to the timbre of other violins. This is a vast field of study with many points of interest, so we will narrow the focus down to the corpus (the body) of the violin.

This thesis focuses on the following topics:

- Can listeners distinguish between Stradivari and non-Stradivari violins?
- Can we describe the differences between Stradivari violins and non-Stradivari violins?
- What is the function of the bridge on the perceived sound?
- How is the corpus described in literature?
- We construct a model and a modelling cycle to gradually increase the accuracy of the model in comparison to actual violins.
- How does our model compare to other models and measurements in literature?

To answer the research questions and address the modelling cycle, a literature study is done considering multiple perspectives with respect to the violin. Thereafter, the model is introduced; the the first iteration of the model is implemented and the results are compared with the literature.

We start with a Literature study describing previous models, experiments and meta-analyses. This will be a vast portion of the paper, showcasing previously found results and answering most of the research questions. Based on the literature, we provide the The model and its modelling cycles and numerical implementation given in the Finite Differences and method of lines. Afterwards, the findings are presented and examined in the Results and Discussion and a summary of the literature, results and discussion is given in the Conclusion and outlook. Lastly, extra information and additional derivations are given in the Appendix.

This graduation thesis for the Double bachelor Applied Mathematics Applied Physics is done at the Delft University of Technology under supervision from Dr. B. Meulenbroek and Dr.ir. D.J. Verschuur at the departments of Mathematical Physics and Imaging Physics, respectively.

Acknowledgements

I would like to thank Dr. ir. van der Toorn for the first two months of supervision and for the opportunity to do this project.

Additionally, I would like to thank Prof. Dr. ir. Vuik for assisting with my understanding from the method of lines and numerical methods in general.

2 Literature study

In this section, we give an overview of important acoustic properties and tools needed to determine the differences between violins. We begin with a characterisation of the colour of the violin, timbre, and how the timbre is characterised. This also includes whether listeners can distinguish different styles of violins from one another.

After the introduction to tone colour, the following topics are discussed:

1. The radiated sound
2. The bridge
3. The corpus
4. The internal modes, or cavity modes

In the sections below, we examine the purpose of each of the categories, showcase how the different categories intertwine with one another and relate to the tone colour.

2.1 Timbre and character of the violin

When listening to music, we experience a shift in attention and behaviour[15]. For music with more dynamics and higher beats per minute, there is more attention drainage in comparison to slower and calmer music. At face value, or to the untrained ear, this is all there is. However, there is much more to be explored in a listeners perception of the music and the amount of disruption in concentration a listener experiences.

In the context of the violin, the most prevalent feature of the music/sound effect is a combination of the skill, technique and understanding of the music the violinist has. The differences between players is immense and will often overshadow any other properties of the music or instrument. Though, we must not confuse this with the absence of other properties to investigate. Namely, if one violinist plays two different instruments with roughly the same technique, skill and emotion, the music will still sound slightly different. Of course, it is not possible to use the exact same technique twice, but very experienced players are able to keep their performances up to high standard. Having said that, the other reasons for the differences in sound are therefore composed of two different systems: the violin itself and its environment.

Now suppose the violins are played in the same room with the same temperature, humidity, air pressure, etc., essentially ruling out the environment as a potential factor for different behaviours of the sound. The only cause for the difference in the music will then be the violin itself. The characteristics of these differences is unique to the violin and is constant across violinists as these differences rise from the material properties of the violin. We call this timbre. Timbre, in layman's terms, is characterised by a number of things: the colour of the sound, the warmth of the sound and the roundness of the sound. It can be described in many more ways since there is not an exact definition of timbre. In music, timbre is sometimes even referred to as the soul of the instrument. In fact, there are many more ways to describe timbre. Though, trends do appear when listeners are asked to describe sounds.

Before we can make an analysis of the sounds of different violins, it is important to know how different terms used to describe music relate to one another. Especially given the subjectivity of timbre and ambiguity in the meaning of words describing the feeling of music. Fritz et al. has investigated this in a small sample size study in which the relation between terms often used for timbre, in English, is sought. The results describe antonyms and synonyms, which would not be found in pure semantics and are used coherently by the sample group. The study used sixty-one words, given as descriptions of timbre by nineteen native English speaking violinists and by selecting words found in a violin magazine, *The Strad*, by frequency. These words were then grouped by fourteen other violinists. This data was then shown in two Multi dimensional scaling (MDS) maps. The first one describes the overall sound quality and the second one describes ease of playing. Both MDS maps can be found in Figure 1.

Figure 1a describes the overall sound quality. The axes of the plot are dimensionless and do not show a clear indication of which property is measured. However, we do have a good indication when looking at the grouping of words. First note that the vertical axes has brilliant and dead at the opposite of the spectrum. This is supported with muted and dull at the high end of the spectrum and bright and strident at the low end of the

spectrum. We see that the low end of the spectrum describes music where the dynamics and articulation of the music are prevalent whereas the high end of the spectrum describes music in an attenuated manner. The horizontal axis has warm, rich and mellow at the high end of the spectrum and cold, harsh and metallic at the low end of the spectrum. In musical terms, this indicates a music rich in harmony at the high end of the spectrum and subtle discords at the low end of the spectrum.

Figure 1b describes the ease of playing. On the horizontal axis, the spectrum goes from unbalanced, dead and unresponsive to balanced, clear and alive, indicating enhanced musicality near the higher end of the spectrum. The vertical axis is less evident as the musical interest seems to mitigate near the higher end of the spectrum. However, the spectrum of semantics on the vertical axis shows more ambiguity when translated to musical jargon.

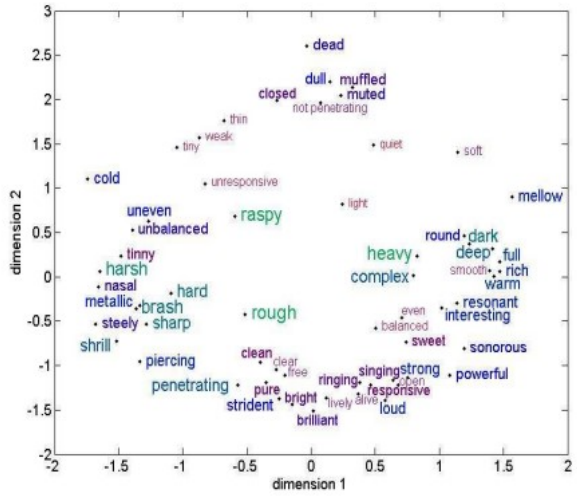

(a) The overall sound quality in the MDS plot with the vertical axes having dead and brilliant at the outer ends of the spectrum and with the horizontal axes having cold and mellow at the ends of the spectrum.

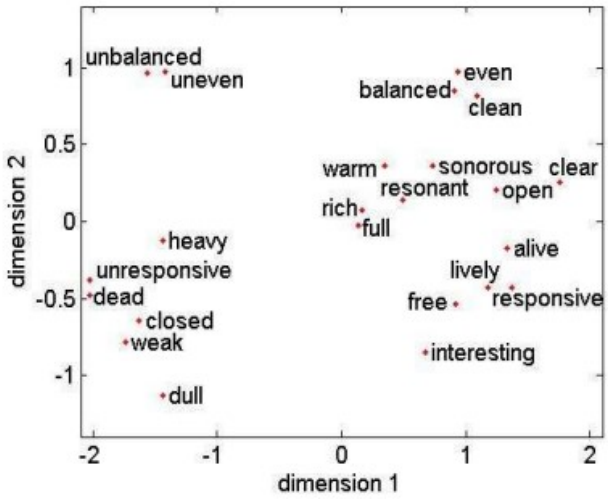

(b) The ease of playing in the MDS plot with the horizontal axes having clear and dead at the outer ends of the spectrum and with a vertical axis which mitigates musical expressiveness near the higher end of the spectrum.

Figure 1: Two multi dimensional scaling (MDS) plots of different descriptors for timbre in violins, after Fritz et al.

Stepanek yields similar results in the sense that violinists will use terms coherently to describe the different sounds. In the paper, five different notes were listened to by eleven violinist in an an-echoic room. Each note was listened to five different times to rank different attributes on a scale of zero to ten. The attributes included sharp, dark, clear, narrow and perceived sound quality, in this order. Using Kendall's coefficient of concordance, a coefficient to measure agreement in a sample size experiment, this resulted in very coherent rankings for the terms dark and narrow specifically. Additionally, dark and sharp were found to be strongly negatively correlated with one another. The paper also mentions that the quality of the violin can somewhat be deduced from the collection of words used to describe the violin. This result was to be expected as the timbre of a violin is largely intertwined with the quality of the violin. This is the case since our sense of quality for a violin is largely based on our perception of the sound it makes, which has a direct relation to the timbre of the violin.

Having said that, all the aforementioned ways to describe timbre in English terms are quite ambiguous. But to describe timbre in an effective way is quite difficult since it is up to interpretation of the individual. In turn, the translation from the English dictionary to a mathematical description is up for discussion, if one can even be found, since we cannot get a general consensus for the timbre of an instrument. After all, it is heavily based on the subjectivity of the listener. However, as Fritz et al. and Stepanek have shown, violinist or experienced listeners tend to gravitate towards the same words, which could very well be part of a deep rooted convention in the musical community or among musicians.

2.2 Distinguishing between violins

The interpretation of timbre is subjective to each listener. However, as shown before, the descriptors for timbre are coherent and can describe musical and acoustic properties. Consequently, a number of attempts has been made to statistically categorise timbre in relation to its descriptors. One of these attempts are the Dünnwald's timbre parameters and simplified versions of these parameters [18]. Each separate parameter describes a type of sound which is affiliated with this parameter. Application of these parameters boils down to, for example, a sound pressure graph compared to specifically defined frequency bands. The radiated sound of the violin is split into several different parts, as illustrated in Figure 2a. The long time average spectrum of a del Gesu violin is divided into sections A-F. The Dünnwald's parameters, along with its timbre descriptors, are then defined as shown in Table 1.

Table 1: Table of the Dünnwald's parameters and their timbre descriptors, after Buen. The L value is the the first air resonance level compared to the top level in the frequency region of $649Hz$ to $1090Hz$, L_{eq} is the sound pressure level as measured in a certain frequency region and L_{max} is the maximum sound pressure level in a certain frequency region.

Dünnwald's parameter (dB)	Description of timbre
Bass: $L = L_{max}(244 \text{ to } 325Hz) - L_{max}(649 \text{ to } 1090Hz)$	high values if the violin contains a rich bass.
Nasality: $L = L_{eq}(190 \text{ to } 650Hz \text{ and } 1300 \text{ to } 2580Hz) - L_{eq}(650 \text{ to } 1300Hz)$	high values if the violin is non-nasal
Clarity: $L = L_{eq}(4200 \text{ to } 6879Hz) - L_{eq}(4200 \text{ to } 6879Hz)$	high values if the violin is clear, low values if the violin is harsh

Buen compares the average-long time average sound pressure of 15 Stradivari violins to the average-long time average sound pressure of 15 Guarneri del Gesu violins, shown in Figure 2b. (Both of these violin makers lived in Italy in roughly the same time period. Both instrument makers are known for the quality of their instruments). The paper finds that although quite similar, the average sound pressure graphs contain only slight differences, which might be picked up by attentive listeners. If Figure 2b is compared to Figure 2a, we see that the differences of the long time average spectra of the Stradivarius en del Gesu violins could be noticed with differences in the sonority and in the brilliance of the sound; creating a first step in relating the long time average spectra or power spectra of the violins to their timbre.

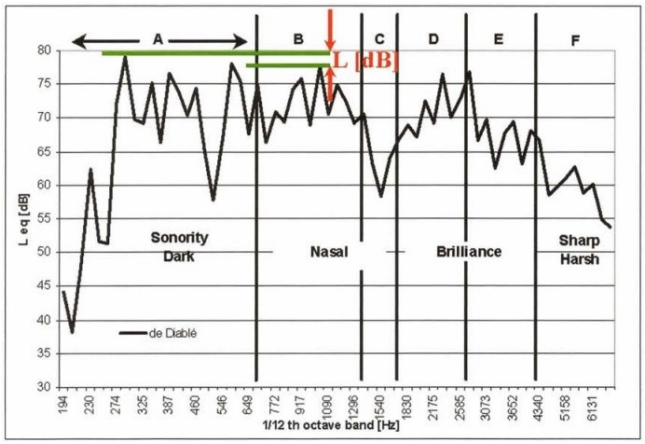

(a) The long time average spectrum of a del Gesu violin, separated into different sections. The L-parameter as used in Table 1 is shown per example. Additionally, a relation between the frequency regions and timbre descriptors is shown.

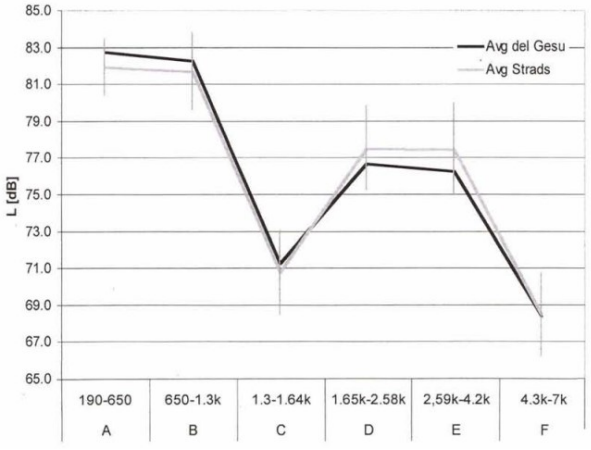

(b) The long time average spectra of the average Stradivarius violin and the average Del Gesu violins. For each type of violin, fifteen violins were used to calculate the average. The errorbars show one standard deviation.

Figure 2: Two long time average spectra of historic violins which are considered to be of quality, showcasing the Dünnwald's parameters and the differences between Stradivarius and Del Gesu violins; after Buen.

Setragno et al. has also done an experimental study into the differences in the acoustic of "quality" and "lesser quality" violins. In this study, fifty violins were chosen; thirteen of which were historical violins, twenty-eight of which were high quality contemporary violin and the rest was made by a violin school (and its students). For each violin in the study, fifteen different excerpts were taken: four on open strings, four with different notes

on a string and seven were parts from several pieces. To start and stop the notes, a root mean square (RMS) energy threshold was used. The remaining audio excerpt was then split into two parts. Parts where the energy is larger than the RMS energy and parts where the energy is lower and decays. This was done because the two different parts contain have different behaviour and contain different information. Especially the decaying part of the sound is notable for historic violins as the paper found that the lowest harmonics retain their power for the first couple seconds after the note started vibrating, losing only about $3dB$ with respect to the note attack (initialisation of the note), whereas contemporary violins lost more than $30dB$ in the same time frame. This coincides with a higher variability in power spectrum (the Z-transform of the auto-correlation function[20]), or in a higher spectral flux as can be seen in Figure 3. As it turns out, spectral flux is at least partially responsible for the violins timbre.

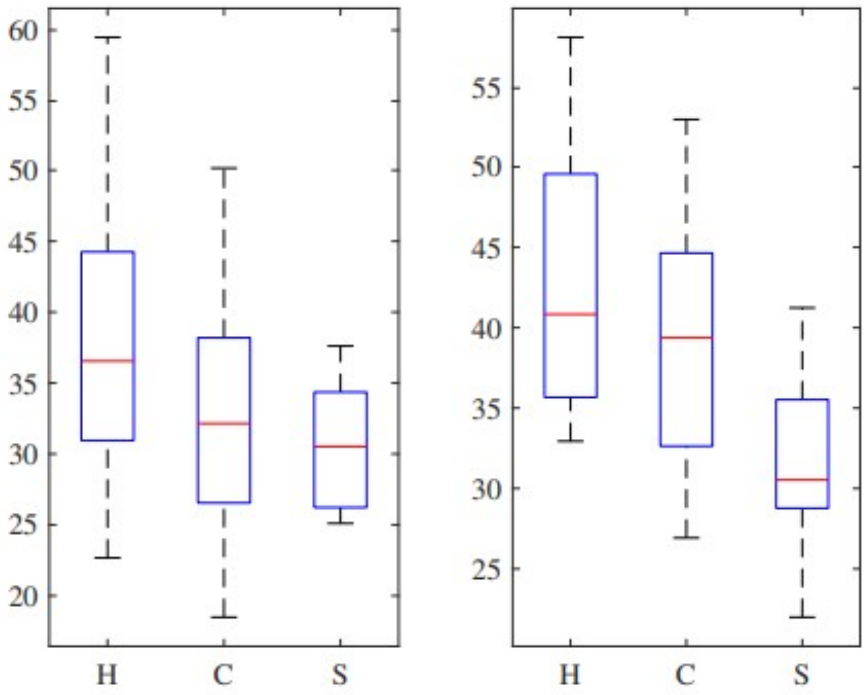

Figure 3: The spectral flux of the A note (on the left) and E note (on the right), both on open strings. The spectral flux is a measure for the rate at which the power spectrum can change. This property makes the historical violins distinguishable from contemporary ones. H are the historical violins, C the contemporary ones and S the contemporary ones made by the violin school, after Setragno et al.

Rozzi et al. did another such study, wherein 70 expert participants, whence the majority was selected no to have prior experience in music, were asked to rate 4 violins (labelled "A", "B", "C", "D") in respect to a reference violin, labelled "X", in 4 set dimensions (openness, brightness, nasality, pleasantness). There were two modern violin (made after 1900), which were A and C. Violin B and the reference violin X were Stradivari violins. Violin D was a cheaper violin of around 300 euros and was crafted by a violin industry. For each participant, a part of the G major scale was first played violin 'X' as reference and then on another violin, for all violins 'A','B', 'C' and 'D'. Then the reliability of the participants was tested with eight trials if the listener gave the same answer for the same scale on the same violin. The results of each participant with a consistency above the 95_{th} percentile were used in the study.

Using a statistical analysis the paper finds results as shown in Figure 4. This can be used in reference to Figure 5 to further decipher the relation between timbre descriptors and the frequency response function of violins. This is also largely coherent with the Dünnwald's parameters. This can be seen in violin 'D' which is very nasal and its frequency response function has a is larger than the Stradivarius violins around $1000Hz$. Similarly, violin 'B' is very open, bright and very pleasant, all of which are closely related to brilliant. For open and bright, this is shown in Figure 1a. In Figure 5, there is a distinctive peak around $1800Hz$ and another around $2900Hz$, agreeing with Dünnwald's parameters. However, violin 'A' seems to oppose this as it also has a peak around $3000Hz$, yet is not described as very open or bright. This could, in part, be explained by the peak around $1000Hz$, making the sound nasal and the peak around $6500Hz$, making the sound sharp or harsh. Nevertheless,

the prevalence of nasality in violin 'A' does hamper accuracy of the Dünnwald's clarity parameter, without assuming nasality or harshness could be dominant over brilliance.

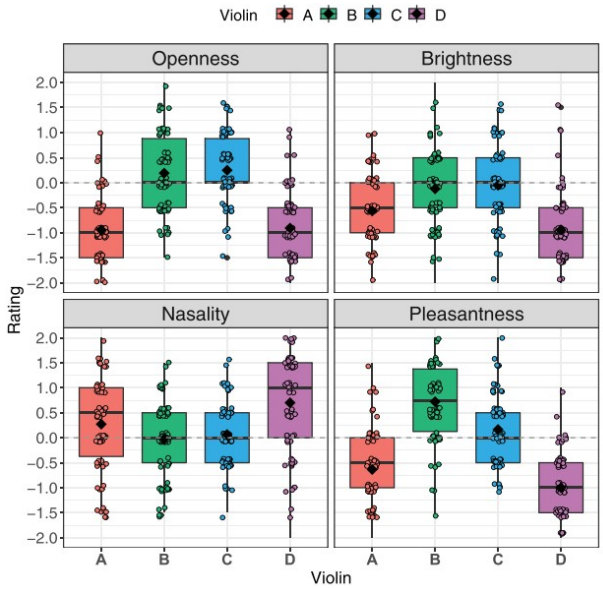

Figure 4: Four violins represented in a box plot for four dimensions as a statistical analysis by 70 listeners. A and C are modern violins, B the Stradivari and D an industry crafted one. A G major scale was played on all instruments with one separate instrument 'X', which is not indicated in the box plot, used as reference, after Rozzi et al.

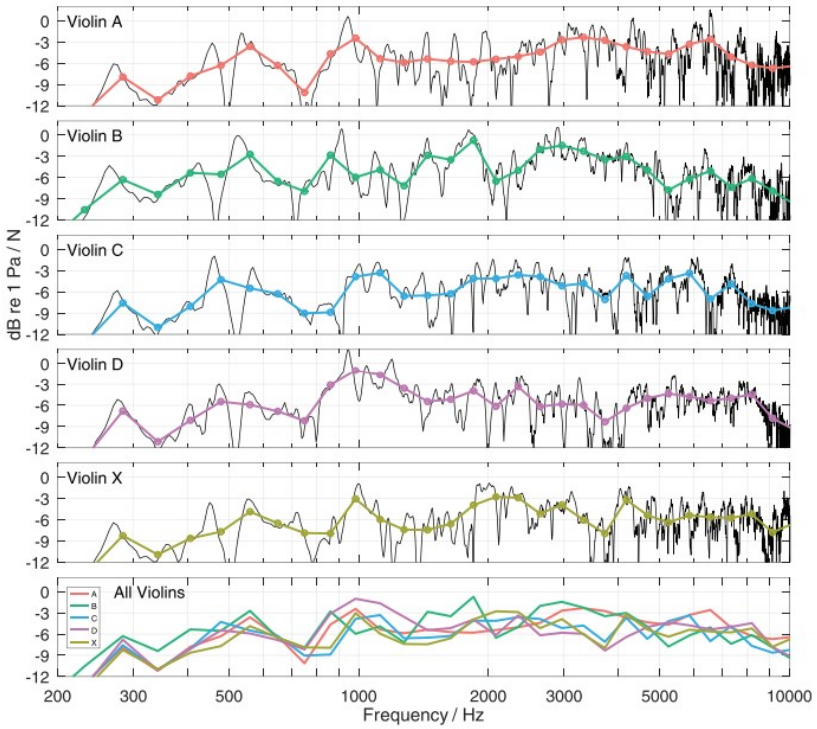

Figure 5: Five frequency response functions, calculated by the root mean square of the sound pressure sampled over intervals of $30ms$ at $48kHz$, of violins. A and C are modern violins, B the Stradivari and D an industry crafted one, after Rozzi et al.

Having seen the differences between violins, both in long time average spectra, power spectra and in statistical analyses, we will now study the cause of these differences and which factors are most important in the uniqueness of the sound we hear.

2.3 Properties of the violin

The differences in timbre and its relation to the power spectrum is not caused by a single part of the violin. However, when studying the violin, we need not examine every part. Bissinger proposes that there are three main systems which can have normal modes. Namely; the corpus (top plate, back plate and ribs), the substructures and the internal cavity modes. Note that no radiation caused by modes of the substructures has been found below a frequency of $4KHz$. In line with this argument, most papers do not even consider the option of other kinds of radiation by the violin. However, this does not mean that the other parts of the violin are not important and we will not yet argue anything else.

Now, when inspecting the corpus as a whole, there are four main different aspects to consider: the radiated sound, bridge, the body of the violin itself (the plates and ribs) and internal modes. Many papers adhere to this concept as they specifically study only one of the four aspects. We will showcase each of the four different aspects and display the key relations between the interwoven systems.

2.3.1 Radiation

On a surface level, the sound we hear is radiated by the violin and we can measure this radiated sound for further analysis. Yet, this is not all there is to sound radiation. Namely, we must be careful when using the term "radiation" as the term is often used to refer to spherical radiation caused by a point source or, more formally, isotropic omnidirectional radiation. However, the acoustic radiation of the violin is by no means spherical and thus forms a problem for comparative research.

2.3.1.a Measured directivity patterns

To investigate the directivity of the radiation, Otcenasek and Stepanek have done an experiment to find the directivity of timbre. Their method describes a violin player, surrounded by microphones in circles with a diameter of $3.2m$ or $1.6m$ with the violin player at its centre. There are 7 circles of microphones, named "A1", "A2", "A3", "A4", "A5", "B1" and "B2". Each circle consists of 16 microphones named "M1" all the up to "M16". See Figure 6a for the layout of the microphones. One of the results yielded in the paper is set of sorted terms

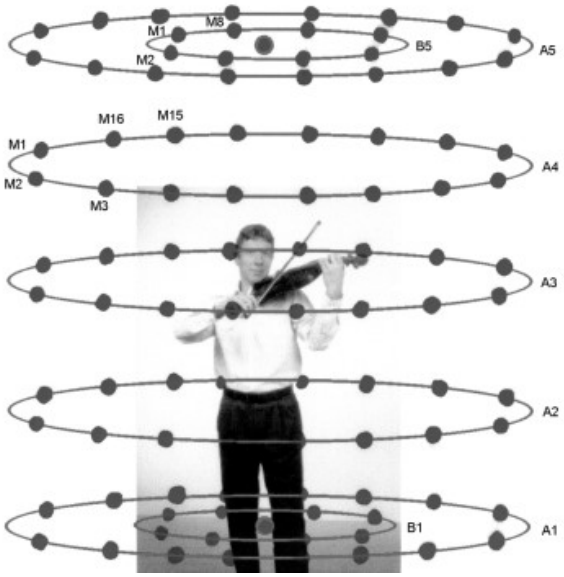

(a) The layout of microphones to detect directivity patterns of sound radiation when playing the violin.

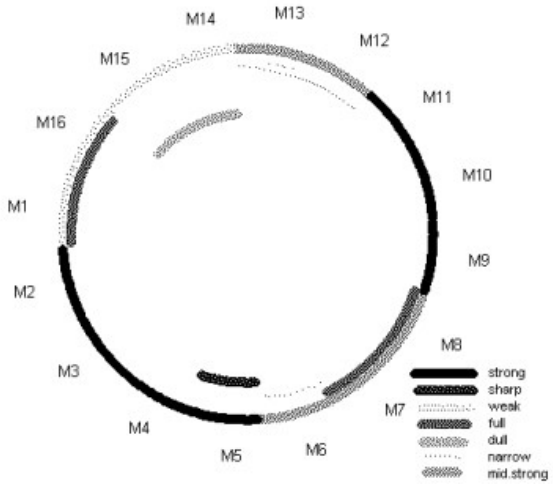

(b) A schematic of terms used in the sound sorting for each microphone.

Figure 6: The layout of microphones described by the method (a) and one of the results to describe violin timbre directivity (b), after Otcenasek and Stepanek.

used to describe the timbre of the sound measured by each microphone of a circle for each sample measured. An example, in this case D_4 and circle $A2$, are shown in Figure 6b. We see that the descriptors of sound pressure and timbre are not spherically constant over ring $A2$. Therefore, the place where the sound is recorded or heard plays an important role for the timbre.

Another, major factor for the timbre is the distance from the violin from which the sound is measured. Perry shows this in his thesis, where he researches the sound radiation from string instruments. Though the paper predominantly focuses on guitars, a number of interesting experiments were done for the violin. One of which is the measurement of radiation efficiency against frequency, near the treble side of the bridge. The plot for monopole, dipole and the total radiation efficiency is shown in Figure 7.

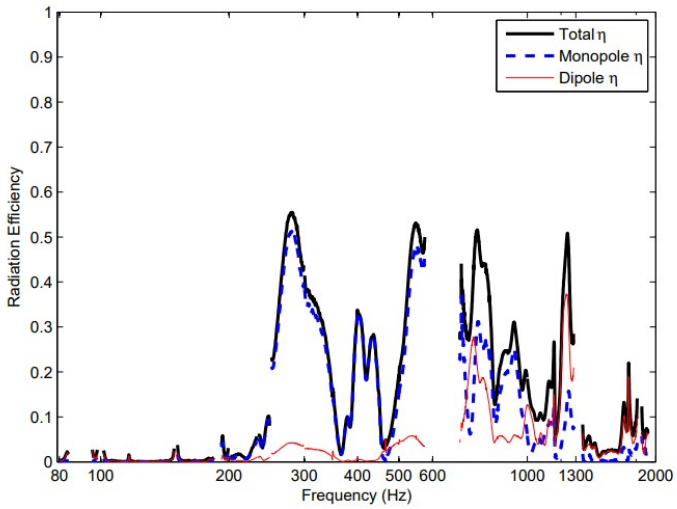

Figure 7: Radiation efficiency measured near the treble side of bridge on a violin for the monopole, dipole and total radiation [24].

There are two notable remarks to made when looking at Figure 7:

1. The monopole radiation dominates the dipole radiation for frequencies of $1kHz$ and lower. However, the dipole efficiency becomes dominant for frequencies higher than $1kHz$.

2. The total radiation efficiency is clearly larger than the monopole radiation efficiency, but adding the monopole and dipole efficiency yields a result which is very close to the total radiation efficiency. This leads us to believe that, for frequencies below $2KHz$, the radiation is predominantly described by monopole and dipole radiation.

2.3.1.b Describing directivity patterns

Now, we have seen that the sound radiation when playing the violin is neither isotropic nor can be solely described by a monopole. Though, the monopole radiation is significant in more ways than one. Namely, besides the overarching prevalence of the monopole radiation at low frequencies, $< 1kHz$, the omnidirectional point source radiation can serve as "the norm" or "the standard". It follows that, measuring the directivity of the acoustic radiation, yields a description of the directivity patterns expressed in deviation from the norm[25].

The sound radiation of the violin can be largely described by isotropic means at low frequencies $< 1kHz$, [26]. This is supported by Figure 7. Though in general, the sound radiation is influenced by many independent factors. This causes a problem in measuring radiated sound. Many models have been made to give a solution to describe the radiation in specific situation, most of which have the violin mounted to a setup without interaction from a player. Though the posture of the player has been shown to influence directivity patterns[25].

The problem of inconsistent measurements can be fixed by creating conventions for measuring or creating a mathematical measures to evaluate the radiation. One such initiative has been taken by Pezzoli et al.. In the paper, a comprehensive study on the radiation of violins is given and the paper proposes a set of metrics which can be used to compare directivity of sound radiation.

Now it suffices to study the separate parts of the violin with respect to radiation. Cremer argues that the radiation of the string will be overshadowed by the radiation of the corpus. In addition, Bissinger notes that any substructures, such as the bridge, pegs, and ornaments, have not been proven to radiate sound in a significant matter. Although Bissinger does not say that the bridge, pegs and ornaments have been proven not to radiate significantly, we shall assume this to be the case. Therefore, we assume that the corpus is the most prevalent radiator of the violin. Hence, describing the radiation and its directivity patterns of the corpus should

suffice in describing the radiation of the violin as a whole.

There is one other matter to be addressed in terms of radiation. The majority of papers comparing different violins to each other do not consider directivity patterns. Yet, as shown before, Distinguishing between violins (2.2) does not seem a problem for most listeners as they coherently use similar sets of terms to describe violins and were able to distinguish between contemporary violins and historical violins. We only give two examples of studies distinguishing the sounds of violins. However, the Stradivari violins are known to be somewhat distinguishable from other violins, though never specifying the place of the listener in respect to the violin. Even though shown not to be the case, assuming that the listeners are always at some random point around the source of radiation may lead one to believe that the exact directivity patterns are of negligible influence to the sound of the violin when comparing two violins.

We want to note that, through the rest of this paper, the term radiation will be used as an average taken over spherical shells at a certain radius from the violin unless otherwise specified. In other words, we assume the violin to be a point source with isotropic radiation. This is solely done to combat ambiguity introduced by papers which neglect to specify any terms of direction.

2.3.2 The bridge

The radiated sound of the violin is arguably the most important part of the violin. However, the vibrations in the string have to be radiated somehow. This is not done by the string itself and is mainly done by the corpus[27]. That being said, the string is not directly connected to the corpus and the vibrations have to travel to the corpus first.

Hence, without any prior knowledge, we can deduct two ways in which the system can propagate the vibrations from the string to the corpus. Either through the fluidum surrounding the string, or through parts of the violin the string comes in contact with. Neville H. Fletcher notes that Savart (1840) described that a solid, non-carved piece of wood glued to a violin at the place of the bridge will produce almost no sound when the violin is played. If the wood is carved to create feet, the sound gets a little better. Then, when the lateral slots of the bridge are made, only then will the violin produce a decent sound. A schematic of the bridge is given in Figure 8.

This implies that the fluidum around the string, in most cases air, will not suffice to propagate create any vibrations to the corpus. It also follows that the pegs do not propagate the vibrations to the corpus. Only rightly carved bridges will propagate the waves to the corpus. This makes the bridge one of the most important parts of the violin.

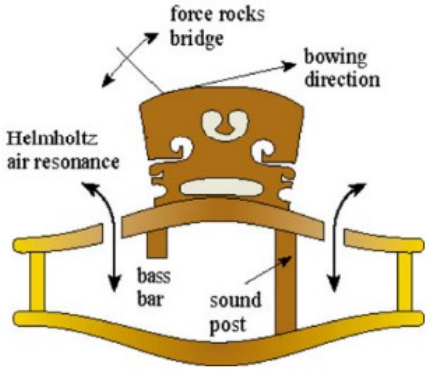

Figure 8: Schematic of the bridge of a violin, after[29]. The schematic shows the bridge placed on top of the top plate, which is connected with the ribs, the back plate. The bass bar and the soundpost are also connected to the top plate and break the symmetry of the violin.

Now, we know that the bridge is important and that the shape of the bridge matters. However, the shape of the bridge seems quite arbitrary at first. By Neville H. Fletcher, we know that feet and two lateral slots in the bridge are needed. The reason for the rest of the topology of the bridge is still unknown. Yu et al. has derived the equations behind the vibrations of the bridge and has numerically created a topological optimised version of the bridge, shown in Figure 9. For the optimisation, the structural response was given by

$$\boldsymbol{I}\ddot{\boldsymbol{U}} + \boldsymbol{C}\dot{\boldsymbol{U}} + \boldsymbol{K}\boldsymbol{U} = \boldsymbol{f}, \tag{2.1}$$

where $\boldsymbol{I}$, $\boldsymbol{C}$, $\boldsymbol{K}$ and $\boldsymbol{f}$ are the mass matrix, dampening matrix, the stiffness matrix and the vector representing external force respectively. Additionally, $\boldsymbol{U}$ is the generalised displacement vector. Then, the optimisation problem

$$\begin{aligned} &\textit{Maximise} && S_D + S_E - S_C - S_F \\ &\textit{Subject to} && \boldsymbol{f}_i^T \boldsymbol{u}_i \leq C_i \end{aligned} \tag{2.2}$$

is posed along with three extra constraints which are beyond the scope of this thesis. Here, C_i is the material compliance, the inverse of stiffness, in the $i-$direction. Additionally, the notation S_j refers to the band average frequency response in frequency domain A to F. These frequency domains coincide with the frequency domains of Dünnwald's parameters describing sonority, nasality, brilliance and harshness as shown in Figure 2a. The second plot in Figure 9 thus shows the optimal design of a bridge to enhance brilliance and attenuate nasality and harshness in the radiated sound of the violin.

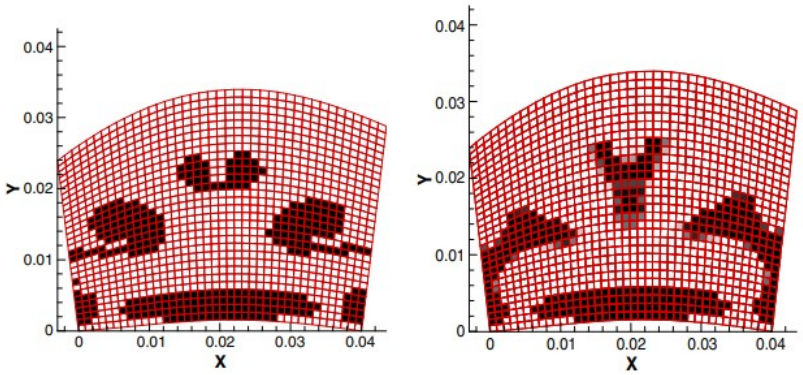

Figure 9: On the left is a typical bridge as seen in modern and historic violins. On the right is a numerical topologically optimised version of the bridge, after Yu et al. This bridge is shown as placed on top of the corpus, normal to the plane of the top plate.

The shapes in Figure 9 are subjectively quite close to one another and at least have some resemblance. This only goes to show the importance of the bridge and its current shape on most violins. Namely, it acts as good, and even near ideal, propagator of waves (made of wood) to the corpus and its separate components.

2.3.2.a Bridge admittance

The topology of the bridge is important for similar, indirect, reason. It is indeed true the current bridges resemble a bridge where the band average frequency response of the bridge hill, regions D and E in Figure 2a, to the corpus is optimised. Analogously, the reason why we require this to be optimised is because the measure in which the bridge conducts the vibrations to the corpus, or bridge admittance, is highly correlated to the radiated sound. Both Figure 11a and Figure 11b show the bridge admittance and radiation of a violin plotted against the frequency on a logarithmic scale. In both cases, it is very apparent that a strong correlation does indeed exist between the bridge admittance and the radiated sound. This is in agreement with the idea that only the bridge is directly coupled to the corpus and only the corpus is radiates significantly to the surrounding fluidum. The coupling between the bridge and corpus the is showcased in Figure 10.

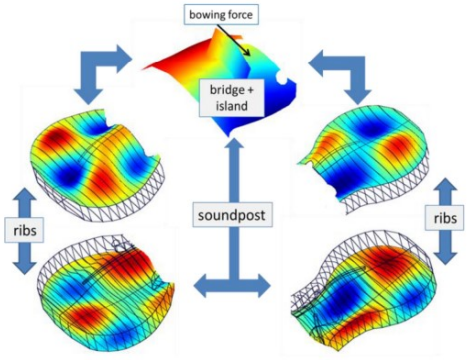

Figure 10: Schematic of coupling between modes localised on different parts of the violin [31]

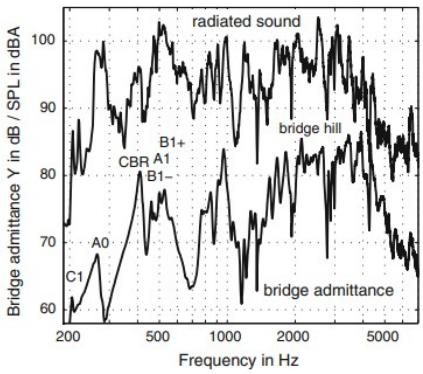

(a) bridge admittance and sound pressure level of a Stradivarius[32].

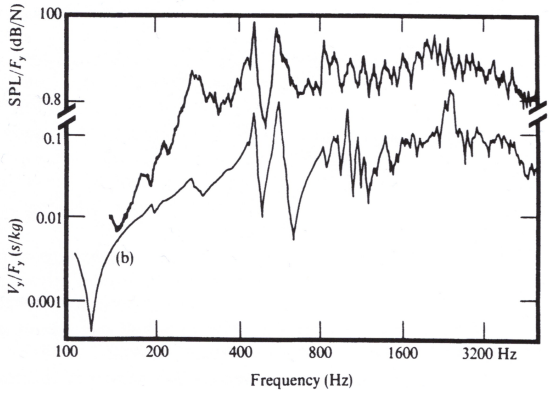

(b) bridge admittance and sound pressure level of an unknown violin [28].

Figure 11: Bridge admittances and sound pressure levels of two violins plotted against the frequency.

Notice that the frequency responses of the two violins in Figure 11a and Figure 11b are remarkably similar. Another simple example of frequency responses is given in Figure 12, where the bridge admittances of two different violins are given. One of which is an expensive and a high quality violin: "del Gesu" by Giuseppe Guarneri, the other is a violin of low value. The bridge admittance, is plotted against a range of frequencies in the hearing bandwidth. It is important to note that the two lines (continuous and dashed) are remarkably similar but are plotted using data from two entirely different quality instruments. We cannot make a clear distinction between the two lines, neither (judiciously) guess which bridge admittance belongs to which violin a priori. Therefore a rough analysis or indication of modes, frequency responses, or sound radiation will not suffice to investigate differences between specific instruments [26], but a thorough analysis is needed.

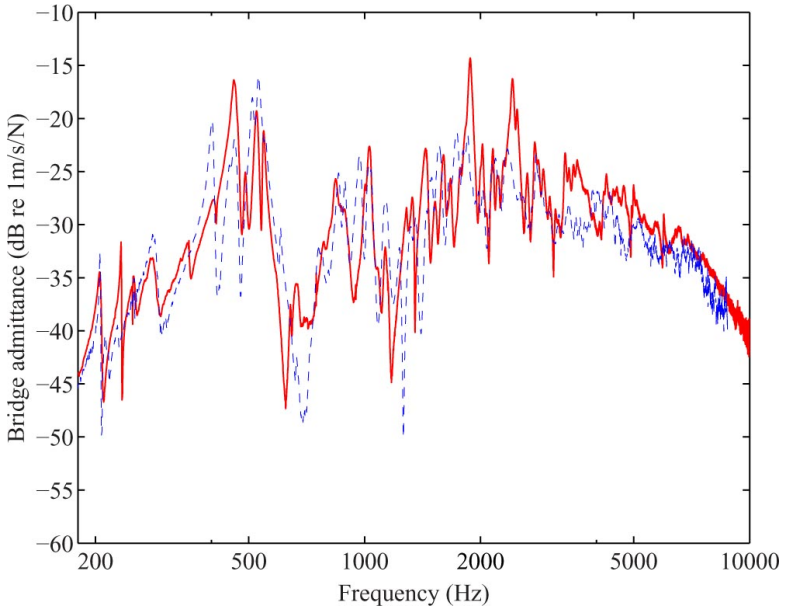

Figure 12: Drive point admittance at the bridge of an anonymous violin of low value (red) and at the bridge of the 'del Gesu' violin by Giuseppe Guarneri (blue) [26].

Though we cannot distinguish the two violins beforehand, we can obtain useful information from this graph. If we look at low frequencies, roughly up to $1KHz$ in magnitude, distinct peaks or spikes are visible. However, from $1KHz$ onward, the spikes become less separable from one another as the frequency increases. This means that describing the radiated sound in terms of modes, while strictly all that is needed mathematically, becomes more difficult and less useful in practice.

2.3.2.b Validity of the bridge admittance's behaviour

However, there is a matter of importance before diving deeper into analysing Figure 12. The paper does not describe how it was sampled or how the timbre is described. Hence, there is a lot of missing information which is needed for the plot to provide us with further insight into the timbre. Namely, any string instrument player may tell you that the bowing of the string can be done in a number of ways. For example, the 'heaviness' of the elbow, the direction of the bowing and the place on the bow being played with are important factors influencing the radiated sound. Even the note being played can create a different timbre from other notes. Further information on material properties and the mathematical equation behind bowing the string and its effects on the bridge and radiated sound are investigated by Askenfelt, Young and Gough but fall outside the scope of this thesis. Namely, due to the absence of information on the obtained data, and possibly the lack of awareness considering the influence of such parameters on radiated sound, we must assume that both violins in Figure 12 were played by the same violinist with as much of the same technique as possible, nullifying any differences made by external factors such as technique and the material properties of the string.

There is one more thing to consider in the acquisition of the data in Figure 12. What did the violins sound like? Is it coincidence that the plots are alike or did the cheap violin have a relatively high sound quality? No audio files nor description of the timbres is given. So we are left to guess what the difference between violins was. Fortunately, Woodhouse also shows Figure 13, plotting the bridge admittances five different 'typical' violins. All of these plots share a similar shape, not too different from the shape of the bridge admittances found in Figure 12. Considering that picking at least five instruments with the same timbre is unprecedented, we can quite reasonably assume that the bridge admittances of any randomly chosen violin will probably follow the same pattern.

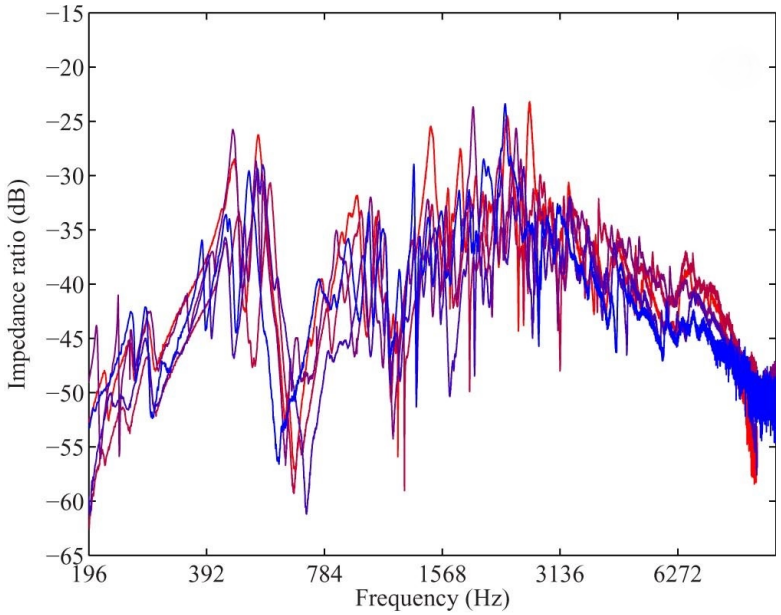

Figure 13: Bridge admittance of five (classical) violins as a function of frequency. The vertical axis is the impedance ratio divided by $0.34\frac{Ns}{m}$ [26].

The number of instruments is nowhere near large enough to construct any form of confidence interval with a statistic if the instruments where randomly chosen, neither do we have any information on the chosen violins to give an indication on the quality or timbre of the instruments. However, to Woodhouse's credit, we can check our hunch in some form. The shape of a guitar's corpus, in very low order approximation of any kind, roughly resembles the shape of the violin's corpus. Therefore, if we find the same kind of impedance ratios for the guitar, our hunch is disproved. However if we find another shape of impedance ratios for the guitar, though our suspicion concerning violin bridge admittance patterns is not necessarily proved, we can make the assumption with more conviction than before. The impedance ratios for guitars is shown Figure 14.

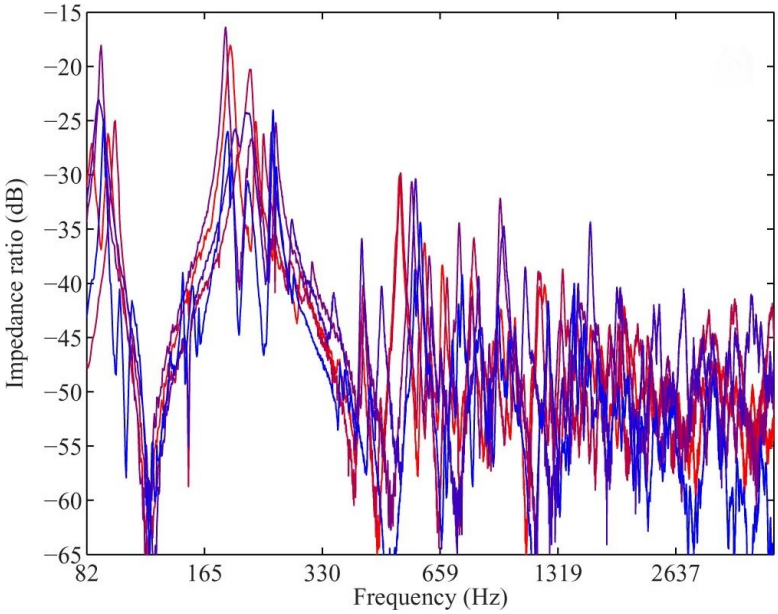

Figure 14: Bridge admittance of five (flamenco) guitars as a function of frequency. The vertical axis is the impedance ratio divided by $0.70\frac{Ns}{m}$ [26].

The impedance ratio for guitars is shown to be entirely different than those found in the violins. So we are inclined to make the argument that the bridge admittance shape is either unique to violins or is common in all violins.

Now we must note that guitars have another kind of bridge and are played very differently than violins. Therefore, if both instruments were struck similarly on an open string, in addition to our low order approximation in corpus shape, we could argue that this serves as supporting evidence to the importance of the bridge on the radiated sound.

2.3.2.c Changes in behaviour of the frequency response

As mentioned before, the behaviour of the admittance changes around $1kHz$. This is because the bandwidth of each mode will go up as frequency increases. However, the distance between each mode does not increase at the same rate. As a result, the modes will become less distinguishable as the frequency increases. This similarity between the bridge and the radiated sound is also present in this perspective. The average sound pressure level of 5 different Stradivari violins is shown in Figure 15. In the plot, the signature modes are shown below $1kHz$. Around $1kHz$, the peaks become less distinguishable whereafter the bridge hill is formed around $2kHz$. In this plot, it is very clearly visible how the language of modes ceases to be useful when analysing higher frequencies. This shows a lot of similarity to Figure 12. Therefore, we can be fairly certain that having a useful language for the bridge admittance will be key to describe the radiated sound.

Like most physical phenomena, this is change of behaviour not a sudden change. Rather, it changes gradually over differences in frequency. Thus, also in a similar fashion to most physical phenomena, we define a dimensionless constants as a(n) (informal) measure for the practicality of the language of modes. Using these dimensionless constants, though not yet defined without loss of generality, will serve us as indicators and will ideally sketch a domain or domains where certain mathematical tools will be accurate within a margin.

Having said that, there are two reoccurring dimensionless constants in literature:

- The modal overlap factor
- The statistical overlap factor

The modal overlap factor and the statistical overlap factor can be defined alongside one another. The constants are described to be the factors relating all respectable violins in a single model[36]. The modal overlap factor[37] is defined by:

$$M = \frac{\text{bandwidth of modes}}{\text{modal spacing}}. \tag{2.3}$$

In the case of the violin, the modal spacing stays roughly constant while the damping bandwidth of the modes increases[36]. Thus, the modal overlap factor increases. Though, the modal overlap factor does not suffice in explaining the whole picture. For example, when modelling a subsystem with ρ mass per unit length as $\rho = \rho_0(1 + \epsilon U)$ for U a random Gaussian and ϵ arbitrary, then the modal overlap factor depends only weakly on the arbitrary constant and thus does not account for its random nature. The statistical overlap factor[37] does take this into account. It is defined as:

$$S_n = \frac{2\sigma_n}{\langle \omega_{n+1} - \omega_n \rangle}. \tag{2.4}$$

Here, ω_{n+1} and ω_n are the $n+1$'th and the n'th natural frequencies respectively with σ_n the standard deviation of the n'th natural frequency. Manohar and Keane show that the statistical overlap factor can be related to the frequency region where oscillations in statistics disappear. Though, to further characterise the bridge admittance for high frequencies $\geq 1kHz$ using the modal overlap factor, statistical overlap factor and maybe even the statistical energy analysis framework[26] are necessary, more in depth research needs to be done on this topic in regard to the violin to reach any significant results.

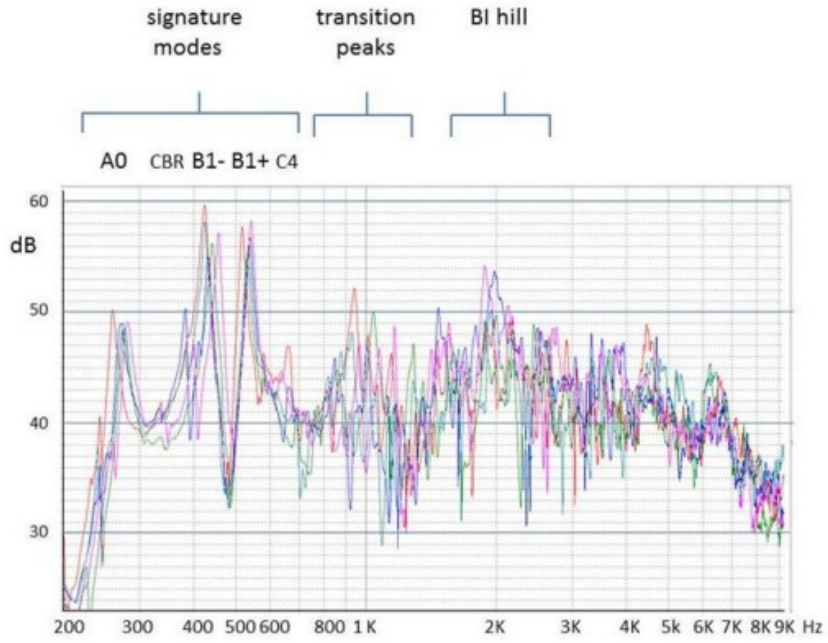

Figure 15: The plot of the average sound pressure level across 5 different Stradivari violins [38].

2.4 Bending plates

As shown before, the bridge and the radiated sound caused by a violin are strongly correlated. But, the corpus still plays an important role in the radiation of the sound. As shown in Figure 51, the corpus of the violin consists mainly of the top plate, bottom plate, ribs, sound post and bass bar. By the logic Cremer uses for strings in respect to radiation, the top and bottom plates of the corpus will be the predominant radiators. Deconstructing the corpus yields us a bare coupled system. The plates are coupled to each other by the ribs. However, before searching the intertwined equations of a coupled system, we shall first consider the bending wave equation on a thin plate and other possible theories to describe bending plates.

In the first section, we will discuss the equations of motion for isotropic bending plates which are derived by using the bending moment with generalised boundary conditions and initial conditions. Then, we will show three specific kinds of boundary conditions which are applicable to the corpus of the violin.

In the second section, we show other feasible theories for thin plates and skim over the principles of their dynamics. Additionally, we take a closer look at the Classical Kirchhoff theory and an application thereof: Chladni patterns.

For the Chladni patterns, we showcase differences between violins of different quality and a theoretical nodal lines in compared to measurements. For the thin plate theory (Classical Kirchhoff theory), the equations of motion are described whereafter a the numerical results for some plates with astounding detail. Namely, the plates are not only guitar shaped plates, a comparison is made to guitar plates with f-holes and with a sound post, making it the most realistic results we have seen so far.

2.4.1 Equations of motions

A priori, suppose we have some plate Ω with thickness h and lies in the (x, y)-plane. Neville H. Fletcher gives the derivation for a bending bar, which it extends to the equations for a bending plate. Now, Neville H. Fletcher states that a stiff membrane can behave plate like. In a sense, this is logical as reducing the bending stiffness from a bending plate yields a membrane. However, Neville H. Fletcher does state a different equation for the wave equation of a membrane than for the flexural wave equation on a thin plate, or bending plate. First, the bending wave equation on a thin bending plate and on a membrane are given by

$$\frac{\partial^2 U}{\partial t^2} + \frac{Eh^2}{12\rho(1-\nu^2)}\nabla^4 U = 0 \tag{2.5}$$

and

$$\frac{\partial^2 U}{\partial t^2} = \frac{T}{\sigma}\nabla^2 U + \frac{Eh^2}{12\rho(1-\nu^2)}\nabla^4 U = 0 \tag{2.6}$$

respectively. Here, U is the displacement along the z-axis (out of the (x, y)-plane), T is the tension, h the thickness, E the Young's Modulus, ρ the density, ν Poisson's ratio and σ the mass per unit area. Second, the generalised boundary conditions are given by

$$\Big[\sum_{i\in\mathbb{N}} \alpha_{i,1} D^{(i)}_{\vec{n}_{(x,y)}}\big(U(x,y,t)\big)\Big]_{(x,y)=(x_{\partial\Omega},y_{\partial\Omega})} = f_1(x_{\partial\Omega}, y_{\partial\Omega}, t) \tag{2.7}$$

and

$$\Big[\sum_{i\in\mathbb{N}} \big(\alpha_{i,2} D^{(i)}_{\vec{n}_{(x,y)}}\big(z(x,y,t)\big)\Big]_{(x,y)=(x_{\partial\Omega},y_{\partial\Omega})} = f_2(x_{\partial\Omega}, y_{\partial\Omega}, t), \tag{2.8}$$

where $D^{(i)}_{\vec{n}}$ is the i'th directional derivative with respect to $\vec{n}$, $\alpha_i \in \mathbb{R}$ and $(x_{\partial\Omega}, y_{\partial\Omega}) \in \partial\Omega$ where the directional derivatives exist. Additionally, the boundary conditions require that f_1 and f_2 are sufficiently smooth functions. Note that each boundary needs two boundary conditions since there exists a second order derivative, with respect to time, of the displacement U. Finally, the initial conditions are given by

$$U(0) = v(x, y) \tag{2.9}$$

and

$$\frac{\partial U}{\partial t}(0) = w(x, y), \tag{2.10}$$

where $v(x, y)$ and $w(x, y)$ are also required to be sufficiently smooth functions.

Generally, the boundary conditions can depend on many factors, however in the case of a plate, we can consider three specific kinds of boundary conditions at the boundary $\partial\Omega$. This is especially important for different geometries of the plate.

We consider three kinds of ends[39]; namely the free end, the supported end and the clamped end. Let $\vec{n}$ be the normal vector at $\partial\Omega$. Then, the free end describes $\frac{\partial^2 z}{\partial n^2} = 0$, $\frac{\partial^3 z}{\partial n^3} = 0$for all$(x, y, z) \in \partial\Omega$. Similarly, the supported end is described by $z = 0$, $\frac{\partial^2 z}{\partial n^2} = 0$ and the clamped end is described by $z = 0$, $\frac{\partial z}{\partial n} = 0$. In both the latter cases, $(x, y, z) \in \partial\Omega$.

In the case of a violin, there is one clamped edge, since one edge is held at the chin while playing, for each plate and the rest are free edges (or actually coupled with the other plate). Therefore, the cantilever plate should give an interesting perspective on the bending of a plate.

2.4.2 Other feasible theories for analysing thin plates

Classical Kirchhoff theory is arguably one of the most mainstream theories for bending plates. However other theories for the bending of plates do exist, three of which are the Reissner plate theory, the Mindlin plate theory and the Kirchhoff-Love plate theory.

Reissner and Mindlin plate theories
Wang et al. explains and inspects the relationship between the Reissner and and Mindlin plate theories. The paper shows that the stress resultants of the theories are different. Though for cantilever plates with the exact same shear forces result in coherent in stress resultants in both theories. Therefore this might be a viable option for the violin plates which, as mentioned before, strongly resembles two coupled cantilever plates.

The biggest difference in Reissner and Mindlin plate theories is the bending moment in the i-direction caused by forces in the i-direction, M_{ii}, in plates and the resulting difference between the Mindlin sum and the Reissner sum, which is used to derive a bending wave equation.

Using a superscript $\mathbb{R}$ for Reissner plate theory and a superscript $\mathbb{M}$ for Mindlin plate theory, we get

$$M_{ii}^{\mathbb{R}} = D\left(\frac{\partial \phi_x^{\mathbb{R}}}{\partial x} + \frac{\partial \nu \phi_y^{\mathbb{R}}}{\partial y}\right) + \frac{\nu h^2}{10(1-\nu)q} \tag{2.11}$$

and

$$M_{ii}^{\mathbb{M}} = D\left(\frac{\partial \phi_x^{\mathbb{M}}}{\partial x} + \frac{\partial \nu \phi_y^{\mathbb{M}}}{\partial y}\right), \tag{2.12}$$

where phi_i is the change of slope with respect to the normal, D is the flexural plate rigidity, ν is Poisson's ratio and h the plate thickness. Using these bending moments for the bending wave equation, we yield

$$\nabla^2\left(\frac{\partial \phi_x^{\mathbb{R}}}{\partial y} - \frac{\partial \phi_y^{\mathbb{R}}}{\partial x}\right) = \frac{10}{h^2}\left(\frac{\partial \phi_x^{\mathbb{R}}}{\partial y} - \frac{\partial \phi_y^{\mathbb{R}}}{\partial x}\right) \tag{2.13}$$

and

$$\nabla^2\left(\frac{\partial \phi_x^{\mathbb{M}}}{\partial y} - \frac{\partial \phi_y^{\mathbb{M}}}{\partial x}\right) = \frac{12\kappa^2}{h^2}\left(\frac{\partial \phi_x^{\mathbb{M}}}{\partial y} - \frac{\partial \phi_y^{\mathbb{M}}}{\partial x}\right), \tag{2.14}$$

where κ is a constant introduced in Mindlin plate theory. From these bending wave equations, we see that setting $\kappa^2 = \frac{5}{6}$ yields the similar results for the bending wave equation.

Kirchhoff-Love plate theory
Asakura et al. derives the nonlinear boundary conditions for Kirchhoff-Love plate theory. The bending wave equation is presented in the paper as a set of three equilibrium equations which are given by

$$D\nabla^4 U_z + \zeta D\frac{\partial}{\partial t}\nabla^4 U_z + \rho h\mu\frac{\partial U_z}{\partial t} + \rho h\frac{\partial^2 U_z}{\partial t^2} = q, \tag{2.15}$$

$$\frac{E}{1-\nu^2}\left(\frac{\partial^2 U_x}{\partial x^2} + \nu\frac{\partial^2 U_y}{\partial x \partial y}\right) + G\left(\frac{\partial^2 U_y}{\partial x \partial y} + \frac{\partial^2 U_x}{\partial y^2}\right) - \rho\frac{\partial^2 U}{\partial t^2} = 0, \tag{2.16}$$

and

$$\frac{E}{1-\nu^2}\left(\frac{\partial^2 U_y}{\partial y^2}+\nu\frac{\partial^2 U_x}{\partial x \partial y})+G\left(\frac{\partial^2 U_x}{\partial x \partial y}+\frac{\partial^2 U_y}{\partial x^2}\right)-\rho\frac{\partial^2 U}{\partial t^2}=0, \tag{2.17}$$

where ζ and μ are coefficients for dampening characteristics, ρ is the density, E is Young's modulus, and G is the elastic shear modulus. Note that Kirchhoff-Love theory takes dampening into account and could therefore produce more realistic results in a model without making assumptions for the load q.

Chladni plates

Another option to describe the waves on the plate is using symmetry and nodal lines caused by the symmetry of the plates. The symmetry properties and observations are condensed into a set of "laws" for nodal lines as a result of the flexural wave equation on the plate [42]. The patterns on Chladni plates are often showcased by distributing a bit of sand or other small material made of small crystals. Some crystals gather on the nodal line, and other crystals gather on the anti-nodal regions to do localised low air pressures[42]. However, this should not be used to find nodal and anti nodal lines. Rather, it should only be used as demonstration since the equations of motion for the grains is heavily influenced by statistics and can result in less accurate nodal lines.

Hutchins attempts to explain the acoustics of the violin by using the Chladni plates. It even does so to the extent that the eigenmodes and the Chladni patterns compare. The paper also notices that the Chladni patterns of violins can be an indicator of the quality of the violin. Figure 16a showcases the difference between violins. There are three back plates shown with two different modes each. The upper Chladni pattern corresponds to the second mode and the lower Chladni pattern corresponds to the fifth mode. Only the left violin is of high quality. The middle one has a broadened nodal line in the upper middle part, which indicates that the plate is stiffer in that area. The right one has a slightly lower nodal line, caused by similar stiffness, and has nodal lines which do not connect into an arch. This means that the plate is thicker in that area.

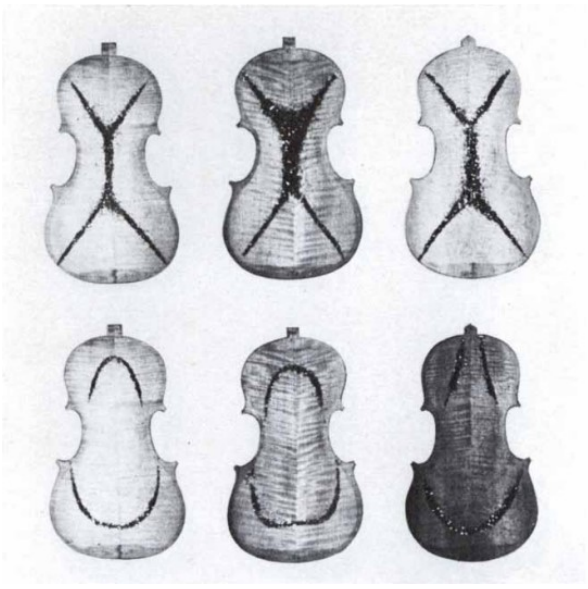

(a) Three different back plates from violins and their second(upper) and fifth(lower) modes. In the second mode, it is clearly visible that the nodal line is thicker in the middle and right violin. This indicates a localised increased stiffness in the plate. In the fifth mode, the right violin has nodal lines which do not connect to create an arch. This indicates an increased thickness of the plate.

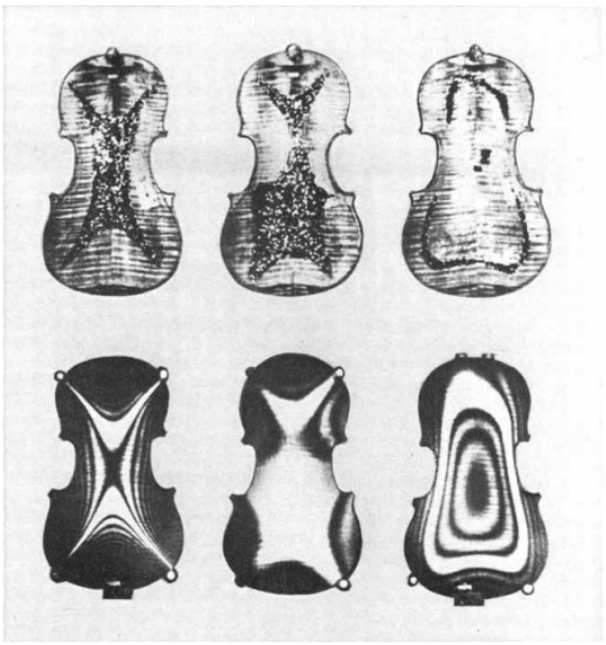

(b) Three different measured eigenmodes at different frequencies (1^{st} row) and their respective theoretical counterparts using Chladni plate theory (2^{nd} row.) The eigenmodes are laser interferograms and the method does not only show nodal, but also anti nodal lines in the form of thin black lines.

Figure 16: Two results[43] using Chladni plates to compare between violins(a) and to compare between experimental results and theoretical results(b)

Figure 16b shows the back plate of one violin. There are three eigenmodes showcased for different frequencies. Each eigenmode is accompanied by it's theoretical Chladni plate counterpart. From this image, it is clear that

the nodal lines do resemble their theory counterpart but will not be accurate enough to display thinner nodal lines. This may be due to the inherent curvature of the plate, giving the random movement of the particles an extra bias on top of the differences in air pressure.

From Figure 16a and Figure 16b, it is quite obvious that the theory and practice surrounding Chladni plates is an eligible tool to create an overview of modal lines in violin plates. However, modal analyses are to detailed for this technique to work.

An-isotropic thin plate theory

Gough (2007) offers a look at an-isotropic thin plates. The paper begins with a showcase of Chladni plates and moves on to the classical Kirchhoff theory. The equations of motion are quite different than Equation 2.5 and Equation 2.6. The paper states that

$$\rho h \frac{\partial^2 z}{\partial t^2} + B_{xx}\frac{\partial^4 z}{\partial x^4} + 2B_{xy}\frac{\partial^4 z}{\partial x^2 \partial y^2} + B_{yy}\frac{\partial^4 z}{\partial y^4} = 0 \tag{2.18}$$

with

$$B_{xx} = \frac{E_{xx}h^3}{12\rho(1-\nu_{xx}^2)} \tag{2.19}$$

,

$$B_{yy} = \frac{E_{yy}h^3}{12\rho(1-\nu_{yy}^2)} \tag{2.20}$$

and

$$B_{xy} = B_{yx} \approx (B_{xx}B_{yy})^{0.5}. \tag{2.21}$$

$E_{i,j}$ and $\nu_{i,j}$ are constants that describe the an-isotropic elasticity of the wood and h is the local thickness of the plate. The frequency on a thin plate away from localised boundary conditions is also shown to be

$$\omega \approx h\sqrt{\frac{E_{xx}}{12\rho(1-\nu_{xx}^2)}}\left(k_x^2 + \sqrt{\frac{1}{\alpha}}k_y^2\right), \tag{2.22}$$

where $\alpha = \frac{B_{xx}}{B_{yy}}$ and $k_{x,y}$ are the wave vectors in the x- and y-direction respectively. Using Equation 2.18 and Equation 2.22, the paper then showcases different modal results, using a finite element approach, with a colour scheme convention where both dark red and dark blue are maximal displacements but of opposite phase. light green means that there is little to no displacement whereas yellow is a small displacement which is in phase with red.

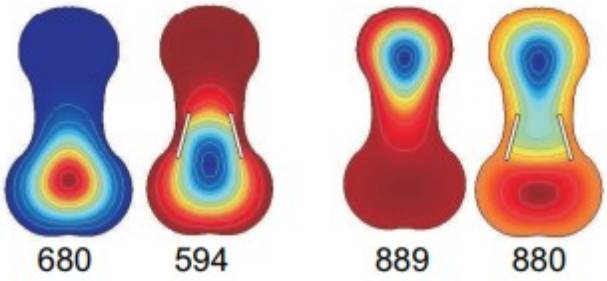

Figure 17: The selected modes of guitar shaped thin isotropic plates. There are two plates, each with a different frequency. For each plate, the modes are calculated with and without slots, representing f-holes[44].

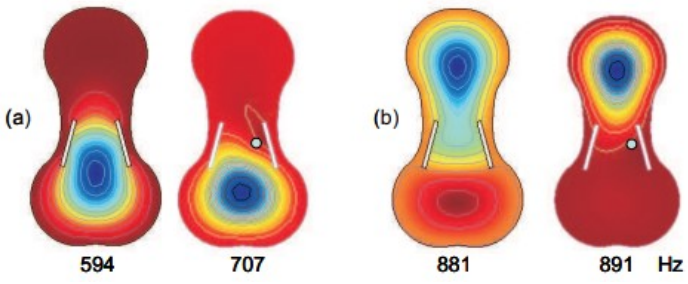

Figure 18: The selected modes of guitar shaped thin isotropic plates. The two plates have different frequencies and for each plate, the modes are calculated with and without a soundpost [44].

Figure 17 and Figure 18 show some of many results published Gough (2007). The paper includes calculated modes on an-isotropic plates and a bass bar. It is very clear from these results that the flexural wave equation for bending plates this paper uses is a good contender to analyse modes on violin plates. In later papers, the author goes into more detail on the method used and the result of the finite element analysis.

For further reading, Norris has compared the Classical Kirchhoff theory, the Kirchhoff-Rayleigh theory and two variants of the Mindlin theory with each other and has derived the dispersion relations for each of them. Besides all the aforementioned theories for bending plates, another theory also stands out: **shear deformation theory**. There are several different branches of the theory which could be useful. First order shear deformation theory accounts for in-plane displacements of the linear kind while third order shear deformation theory accounts for cubic variations of in-plane displacements[46].

2.5 Assembling the corpus in a finite element analysis

Up until now, we have only considered single plates. We will now show the coupling of the plates, as it contains interesting dynamics. Namely, the different plates and the matter in which the plates are connected provide an intricate relations between modes and frequency.

We will first look at how the finite element grid is constructed and show the normal modes of two coupled plates. These are the reoccurring modes which form the basis for every other mode.

Then, we will show the results from a finite element analysis using different coupling models in conjunction with the classical Kirchhoff theory. This includes results for the variable rib-strength and effect of the f-holes. We compare the results, using the rib-strength and the effect of the f-holes to measurements.

After the comparison from the results of the finite element method and the measurement, the finite element model is made more realistic by considering the ribs as spring with two corresponding spring constants. The effect of increasing both spring constants is then shown.

We then discuss the two remaining parts of the corpus: The soundpost and the bass bar. The influence of both parts is then shown. This concludes the results of the finite element model using the classical Kirchhoff theory as shown by Gough and Stoppani.

Lastly, two additional numerical models on of the corpus are shown. Both use a slightly different method. The grid we show in the latter will be used as inspiration for our model in the second part of this thesis.

2.5.1 Finite element model and Cavity modes

Gough (2013, 2015a, 2015b) uses the thin plate theory to set up his numerical model in *Comsol*, using its structural mechanics module[50]. He describes this Finite Element Analysis (FEA) in detail. The geometry of his model is based on the internal rib outlining from a Stradivarius violin, as shown in Figure 19.

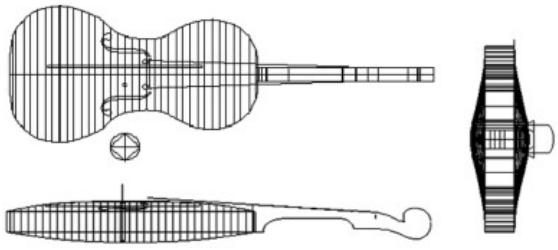

Figure 19: Internal Rib Outlining from the Titian Stradivarius[48].

This grid shows that the top and bottom plate of the violin are coupled via the ribs. When the plates of the corpus are coupled and vibrating, they can generally create twelve different kinds of modes for the corpus itself[38] for normal rib strengths. Figure 20 shows these twelve computed modes for a violin body.

Figure 20 shows an important term, Breathing. Breathing can be described as the net volume change of the corpus over time. The breathing of modes is important as it primarily determines the radiation for low frequency modes[26].

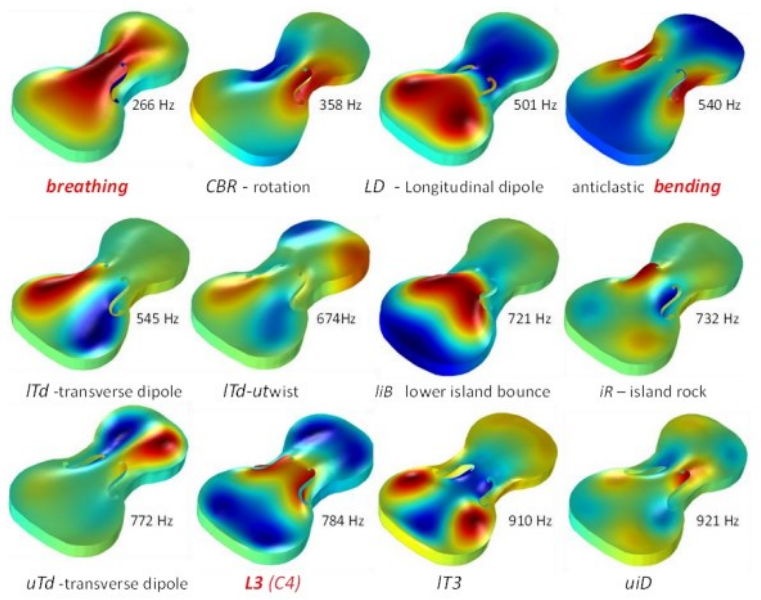

Figure 20: Twelve computed modes for an empty violin body, colour indicating the displacement with colour[38].

Another thing to notice is that the modes are always symmetric or anti-symmetric with respect to the longitudinal axis of the violin. Notice though, that almost none to no breathing at all takes place if the mode is at least anti-symmetric along one of the axes. These are called bending modes. The breathing and bending modes can always be used as orthogonal characteristics to describe the modes[26]. Using these breathing and bending modes as a basis, any latter results can be compared to this principle to check for validity.

The upper left mode is often referred to as the $A0$ mode and the upper second to left mode is often referred to as Centre Bout Rotation (CBR). These two modes are very common in vibrational violin plate analyses and we will find that these twelve modes form the basis for almost every other mode we can find by changing the type and strength of coupling between different parts of the corpus.

2.5.2 Coupling, the sound post and the bass bar

Gough (2015a) describes the influence of rib coupling on the modes in respect to frequency. In the same paper, the influence of cutting f-holes into the wood of the top plate on the modes is described. To analyse the ribs, the Young's modulus and the density are increased by several orders of magnitude. This is done to preserve longitudinal bending modes on the plates at high frequencies. The ribs, as a result, act as springs which attenuate the displacement of the plates.

The f-holes serve two important causes. The first one pertains to the openings in the wood. The two holes allow for breathing. This breathing or volume change creates a Helmholtz resonator. The second effect of the f-holes is the area between them. The wood between the f-holes has more flexibility than the rest of the top plate. This area between the f-holes is often referred to as the island area. The bridge is located on the island area which causes the island area to enhance the transmission of waves to the corpus.

The modes are plotted against the rib coupling strength and the f-hole area strength in Figure 21a and Figure 21b respectively.

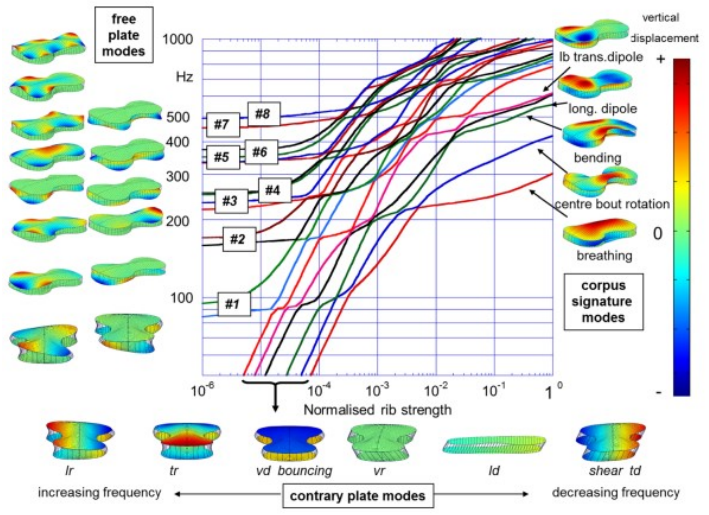

(a) Free plate plate modes plotted against normalised rib strength. Increasing the normalised rib strength yields four of the earlier found cavity modes.

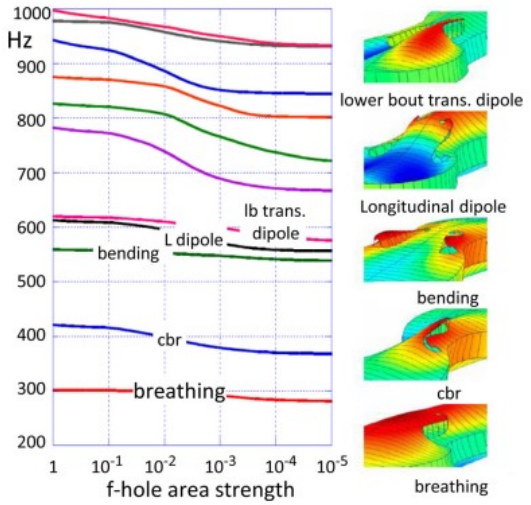

(b) Cavity modes plotted in frequency against f-hole area coupling strength.

Figure 21: Two results[48] where the transformation of the cavity modes in terms of frequency is shown against the coupling strengths of the ribs and f-holes.

Even though the relation between the rib coupling strength and the modes is quite complicated, the amplitudes from the modes become larger whenever the coupling strength of the ribs is increased. We also notice that the modes on the top and bottom plates are either in phase or in anti-phase for stronger rib coupling whereas this is not necessarily the case for weaker rib coupling. Additionally, the frequency increases if the rib coupling strength increases. This is the case since the frequency is $\sqrt{K_{rib}/M_{rib}}$, where K_{rib} is the effective linear rib coupling strength and M_{rib} is the effective mass of the rib. We must also note that modes in anti-phase with one another experience a lot of attenuation due to the extensional spring like ribs near the edges of the plates while modes in phase with one another do not experience this attenuation nearly as much. The attenuation of the displacements gets stronger if the rib coupling gets stronger and causes the frequency to increase slower than the in-phase modes. The difference between in-phase modes and anti-phase modes is clearly visible in Figure 21a.

As the rib coupling strength is increased, six new modes form on Figure 21a, these are the modes which start at the bottom of the plot. These modes are created by combinations of the twelve Assembling the corpus in a finite element analysis.

If the flexibility of the f-hole area is increased, or the flexibility of the island area is decreased, the breathing and bending components of the plate modes are barely changed. However, the f-hole area strength does decrease the frequency of the modes. Furthermore, the cavity, which is being considered as a Helmholtz resonator, couples the air inside the corpus to the plates. The coupling of the breathing modes to the air increases as the surrounding air pressure increases. Gough shows that with increasing ambient air pressure, the frequency of the breathing mode can be increased from $280Hz$ in vacuo to about $400Hz$.

The numerical solution is then compared to the average modes of six modern violins, shown in Figure 22, for four of the most important modes. Note that the measurements of the violin modes were made before the fingerboard and the soundpost were added, therefore a comparison between the numerical model and the measurements can be made. Figure 22 uses two different colour schemes. The first one is for measured modes, on the left side, where white indicates little to no displacement, light red indicates the maximum displacement and light blue indicates the maximum displacement in opposite phase to red. Similar to the previous finite element model results, dark red and dark blue indicate displacement in the opposite direction whereas green indicates little to no displacement.

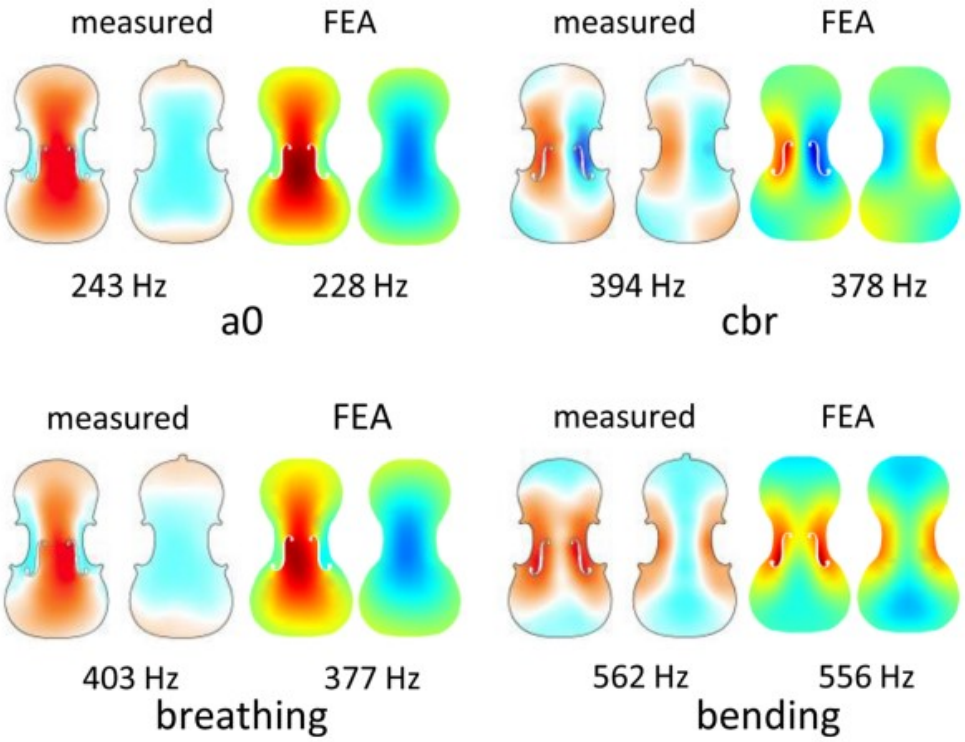

Figure 22: The results of the numerical model including the rib coupling and f-holes compared to measurements of the same modes. For each of the four modes, the top and back plate of both the measurement and of the finite element model are shown. The measurements were taken using the average mode shape of six modern violins.[48]

We see that the shape of the modes is fairly similar. However, the measured mode shapes are slightly off centre and are not completely symmetrical. This often accomplished using the sound post and the bass bar. There are still some factors which have not been incorporated into the model on top of the bass bar and soundpost. Namely, the coupling of the ribs creates bending at the edges of the plates, which can be modelled with extensional and torsional spring constants. Furthermore, an-isotropic properties are yet to be taken into account. The difference in frequency in the modes as seen in Figure 22 may be explained by the absence of the soundpost, bass bar, bending near the edges or by lack of an-isotropic properties being included.

The effects of the soundpost, bass bar, bending due to rib coupling and an-isotropic properties are also shown by Gough. Namely, Gough (2013) investigates the effect of the sound post and its placement on the modes while Gough (2015b) investigates the effects of the bass bar, an-isotropic properties and extensional and torsional spring constants. These spring constants are the effect of the plates bending near the edges due to rib coupling and may be considered an-isotropic effects. The paper also models an-isotropic effects by laying strips with the same density but with varying Young's modulus along materials to mimic elastic properties of wood.

We will start with the bending near the edges of the plates due to rib coupling, shown in Figure 23a and Figure 23b in the form of extensional and rotational spring constants. Then, the effect of the soundpost and its placement are visible in Figure 24b and Figure 24a. Lastly, the effect of the bass bar is shown in Figure 25.

Figure 23a shows the behaviour of only in plane mode plates with respect to the extensional spring constant. The extensional spring constant essentially pins together the plates for high enough rib strengths. However, the rib strength is never high enough. Therefore, the displacement at the edge of the plates is not attenuated completely. In addition to the normal modes being raised in frequency, three new "bouncing" modes are created if the extensional spring constant is high enough.

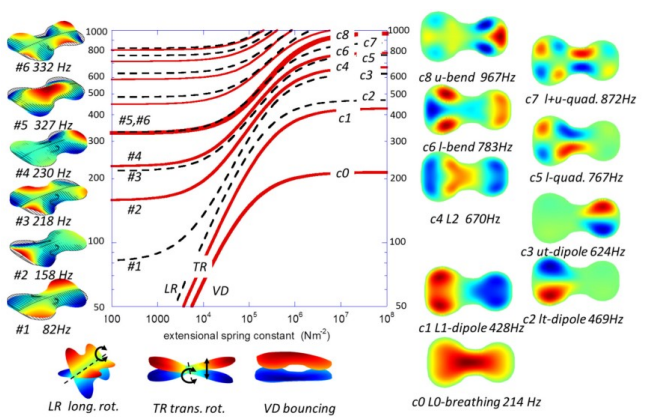

(a) The rib coupling is conceptualised as a uniform distribution of mass less springs at the boundary. The transformation of the modes is shown with regard to the extensional spring constant.

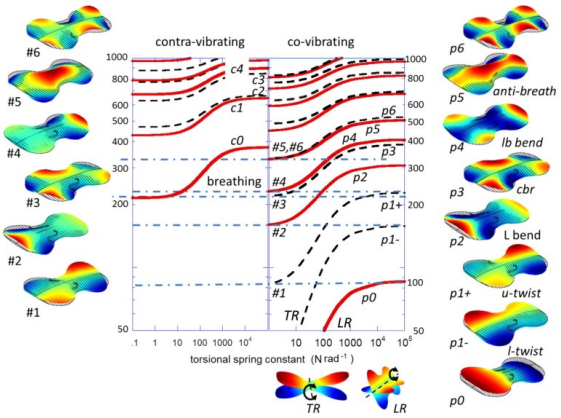

(b) The bending of the ribs yields a constraint on the rotation of the plates at the edges. This is conceptualised with a torsional spring constant to show the rotational attenuation. The transformation of the modes is shown.

Figure 23: The effect of the rib coupling and bending of the ribs of the plates on certain frequencies[49].

Figure 23b shows in-phase and anti-phase modes. At higher torsional spring constants, the effect of increasing the spring constant lessens. This is the case since the potential energy is increasingly determined by the bending of the whole plate instead of by the edge solely. Note that the torsional spring constant clamps the plates together to the rib plane if the rib strength is great enough. However, the plates are still free to move perpendicular to the plane of the ribs.

The soundpost is squeezed between the top and bottom plate of the corpus. Therefore, the two plates are coupled in yet another way. It translates the forces exerted on it by one plate almost directly to the other one. For high enough sound post strengths, the force on the soundpost on top must equal the force on the soundpost at the back plate. The soundpost also attenuates out-of-phase movements from the top and back plates. As a result, the displacements around the soundpost are significantly smaller than on the rest of the plates. As mentioned before, the bridge is located on the violin. But the soundpost, when located near the island area, attenuates the displacement extensively. It functions as a gate like structure for the bending waves.

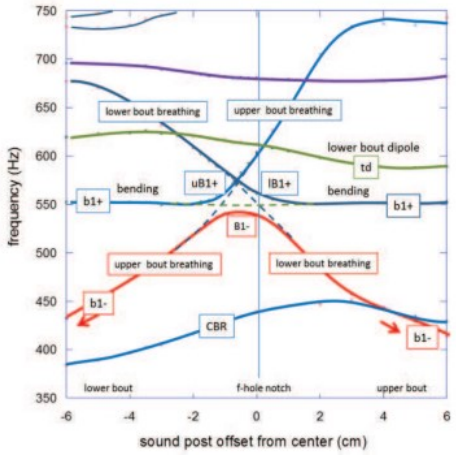

(a)

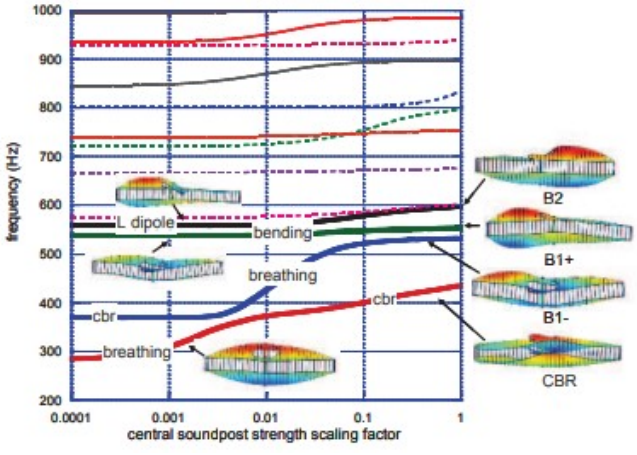

(b)

Figure 24: The effect of the soundpost and moving the soundpost away from the centre[49].

Moving the soundpost away has two effects. First, the gate like effect of the sound post is reduced and it allows the displacement of the plate to permeate through the rest of the plate. Second, it creates asymmetry in the displacement on the plate. Horizontally bowing will then result in rocking the bridge asymmetrically, resulting in strong coupling to the modes. This radiates strongly. Figure 24a shows the effect of the soundpost when it is moved across the island area (parallel to the width of the violin; along the central axis). This allows us to

identify different modes for the upper-and lower bout of the violin, without modes interacting with each other causing a phenomenon called veering.

Figure 24b shows a centrally placed soundpost which, like the ribs, is varied in elastic constant and in its density. The asymmetrical modes are not present as a centrally placed mode will only allow modes which are symmetrical about the central axis. From Figure 24b, it is shown that the most important function of the soundpost, when placed in the centre, is to increase the frequency of the breathing mode.

Figure 25 shows effect of the bass bar on three of the cavity modes. The upper row displays modes with a bass bar and the lower row displays the same modes without a bass bar. It is shown that the bass bar decreases the vibrations in amplitude a little bit and increases the frequency, for the breathing mode, by about 6%. This is because the bass bar strengthens the coupling across the island area. This effect increases for modes of higher frequency. Increased thickness of the plate will have a similar effect on modes locally. The colour scheme used in Figure 25 is that of the previous finite element methods, using dark red and dark blue as opposite displacements.

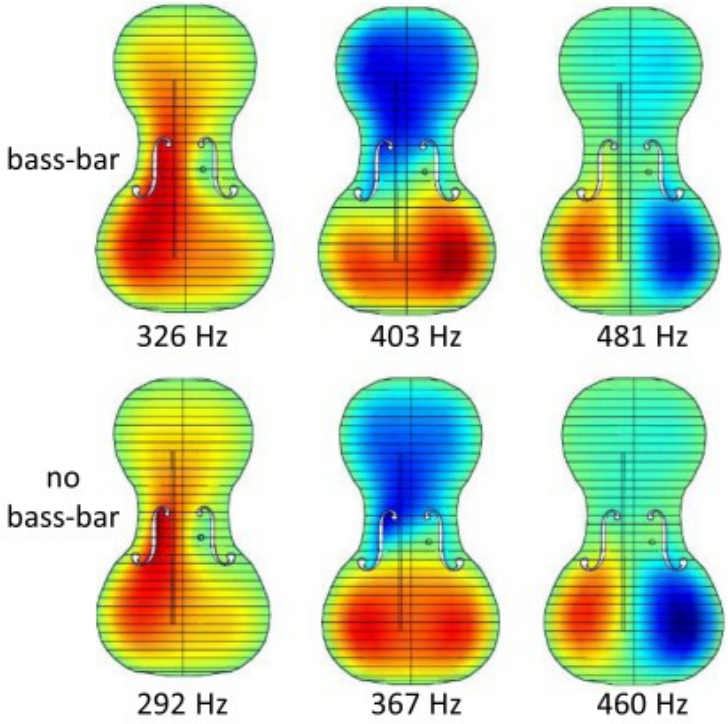

Figure 25: The influence of the bass bar on three arched top plate of a violin with f-holes.

2.5.3 Other finite element models for bending plates

Lomte uses a similar approach to Gough. However, the paper investigates the an-isotropic material properties of the wood and uses this, together with a mesh grid, to create a bending violin plate in *Comsol*. Figure 26a and Figure 26b show the mesh grid of a top plate and show one of the results respectively. The equation of motion Lomte uses is very similar equation of motion used for the optimisation of the bridge, in section 2.3.2, and is given by

$$\boldsymbol{I}\ddot{\boldsymbol{U}} + \boldsymbol{C}\dot{\boldsymbol{U}} + \boldsymbol{K}\boldsymbol{U} = \boldsymbol{f}, \tag{2.23}$$

where, $\boldsymbol{I}, \boldsymbol{C}, \boldsymbol{K}$ are the mass matrix, the damping matrix and the stiffness matrix. Moreover, $\boldsymbol{f}$ represents the external force applied to each grid element.

The results are shown in Figure 26b. Note that the plot shown is does not resemble on of the twelve cavity modes found by Gough. However, it does resemble the displacements found in Figure 18.

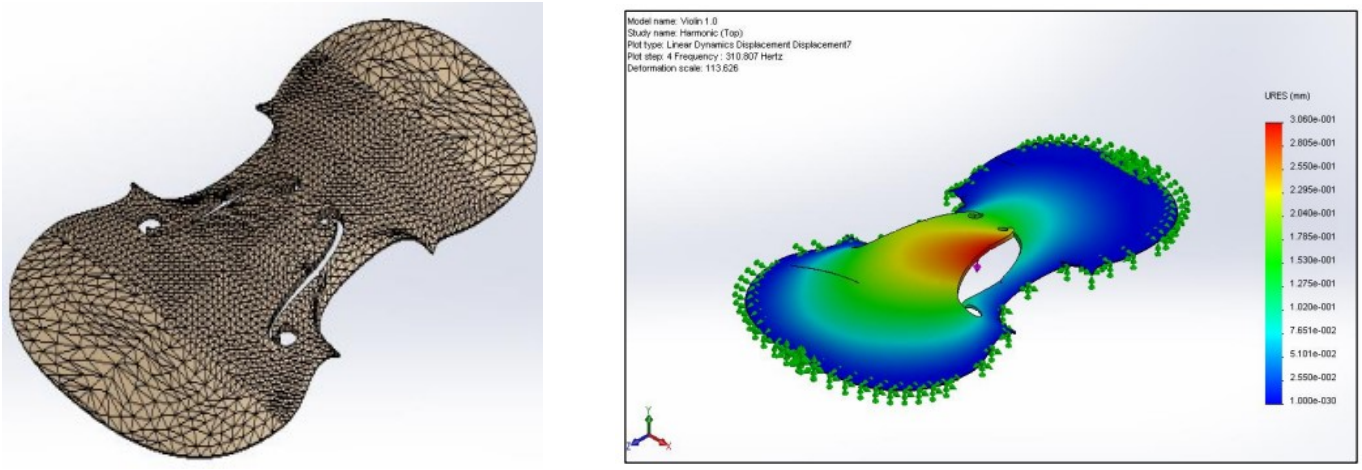

(a) (b)

Figure 26: The mesh grid (a) and the numerically calculated result (b) for the top plate of a violin using the an-isotropic properties[51].

Bretos et al. shows another numerical implementation using a software called *Abaqus*. The paper does not go into detail of the numerical method and the equations used. However, it does state that the mechanical properties of spruce wood were used in the parameters of the model. Nevertheless, the paper clearly showcases its grid. The grid, shown in Figure 27, is detailed but also attainable. Therefore, the attempts in our paper to recreate the shape of a violin will be heavily influenced by the grid used by Bretos et al.. The grid used by Lomte in Figure 26a, although detailed, is not suitable for a manual implementation. Similarly, the model used by Gough is not suitable since it is based on strips, as shown in Figure 19, and the real grid used in *Comsol* is not shown. However, since the paper performs its calculations in *Comsol*, it is likely that the internal mesh grid looks similar to Figure 26a and is too complex to manually implement.

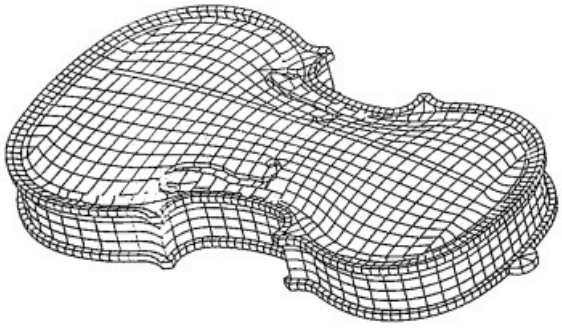

Figure 27: The grid used by Bretos et al. to create a finite element model of the corpus of a violin

2.6 Experimental findings

We have now seen three different finite element models, two have used *Comsol* and one *Abaqus* to calculate the displacement of each grid element in their respective models. Gough has compared one coupled mode to measurements to the average of a hollow corpus but we have not seen any modes on an actual violin.

Jansson et al. uses holographic interferometry. In the paper, the method used to create holographic images is discussed in detail and the violin is constructed with ready made parts such as the ribs, finger board, etc. In order to see the fringes of the interferograms, The neck and fingerboard were covered in white tape. For the holographic interferometry of the whole violin, a method called double exposure was used. In this method, the reconstruction consists of double images which are coherent with one another. Therefore, they can interfere and the deformation of the plates is then shown using the interference fringes. One of the measurements is shown in Figure 28 where the G string is held and the deformations of the violin can be seen in terms of fringes.

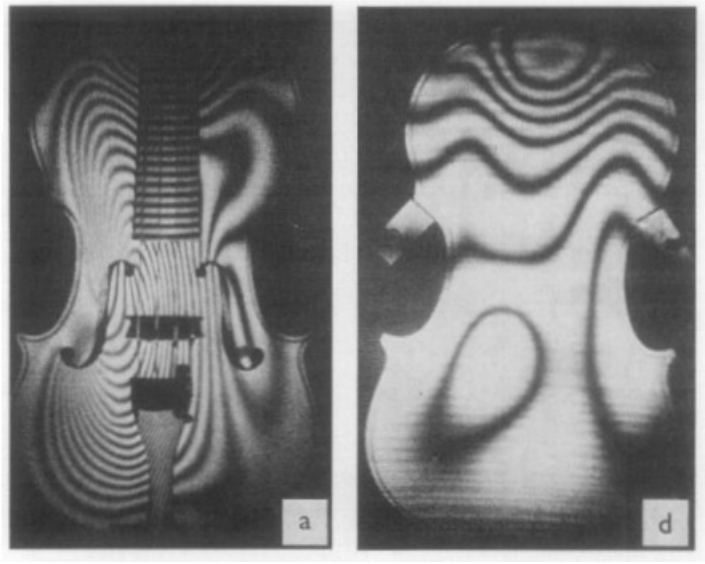

Figure 28: Deformation of the top and bottom plate of a violin while the violin is held in place. The deformation is shown using double image holographic interferometry[53].

As we can see, the mode is highly asymmetric, indicating a significant sound post strength or highly off centre bass bar. Another possibility is adding the breathing mode and centre bout rotation mode, a result likewise to Figure 28 is obtained. This shows that the finite element analysis presented by Gough is viable to model the violin. Still, Figure 28 contains many ripples whereas the every model presented by Gough describes monopole or dipole up to octupole radiation.

Another experiment with optical sensors is done by Luke. However, in this case, the experiment is made as realistic as possible since a chin rest was added and the instrument was supported at the chin rest and the neck. In addition to this, a piece of felt was put on top of the strings to dampen them slightly. Then a coil was attached to the bridge which was electromagnetically vibrated with a sinusoidal pattern. Then optical sensors with a peak sensitivity of $1\mu m$ were used to measure the deformation of the plates. Several measurements were made near resonance peaks of the corpus, resulting in standing modes. Two of these measurements are shown in Figure 29 where the light gray area indicates in phase modes and the dark gray area indicates in anti-phase modes.

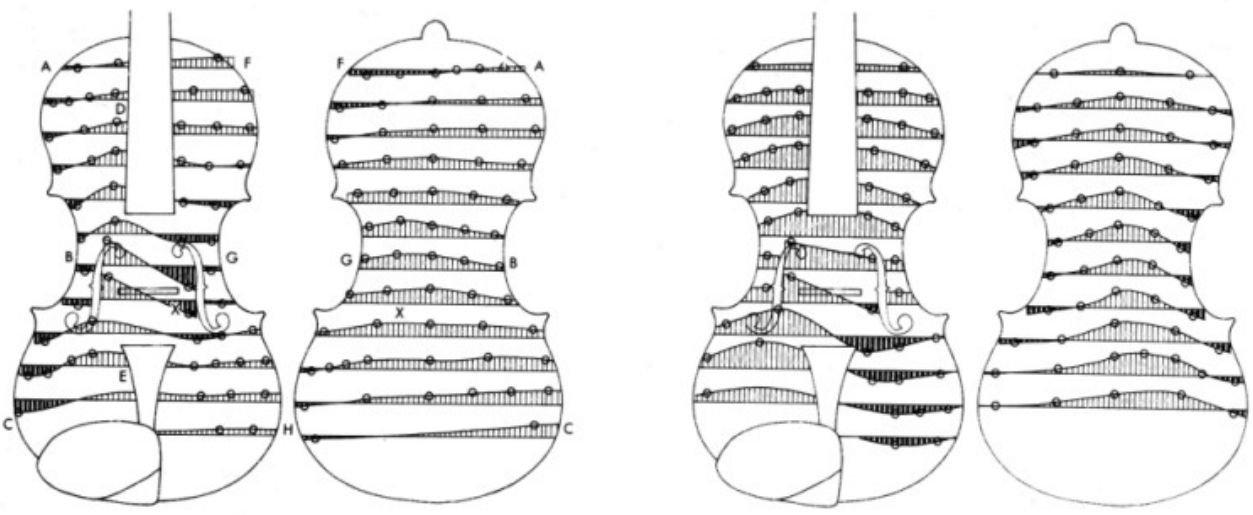

Figure 29: Two measurements of the top and back plate on a violin, made with optical sensors, at different frequency near resonance peaks. The standing wave motion is shown for frequencies of $204Hz$ (left) and $630Hz$ at the right. Light gray indicates in-phase motion and dark gray indicates anti-phase motion[54].

Now Figure 28 and Figure 29 both show vibrational patterns we have already seen in the numerical model described by Gough (2013, 2015a, 2015b, 2018). Namely, in both standing waves, we can see resemblance to the cavity modes shown in Figure 20. Figure 28 strongly resembles a slightly asymmetric form of centre bout rotation (CBR) and Figure 29 strongly resembles a breathing mode on the bottom plates and a transverse dipole on the top plates. This, once again, shows us that thin plate theory comes a long way in describing the modes of the violin.

2.7 Cantilever plate

As mentioned before, the violin resembles two coupled cantilever plates when played on an open string. So interest dictates that studying the cantilever plate and its bending behaviour may offer a look into the behaviour of a violin held at its chin rest. The first iteration of our model does exactly that and will contain a cantilever plate with its displacement induced by a spring mass system located on the plate. The paper by Chiba and Sugimoto is therefore used as a reference to check the results of the numerical implementation of the model, given in the second part of the thesis.

Chiba and Sugimoto derives the flexural wave equation on a cantilever plate with a harmonic driving source using the Lagrangian, solving the flexural wave equation afterwards. In specific, the paper discusses a thin isotropic cantilever plate with free ends. The plate has a length L, a thickness h and a width H. At some arbitrarily chosen point (x_0, y_0), on the interior of the domain in the (x, y)-plane, the plate is coupled with a mass spring system of mass m_e and has a spring constant k_e. The deviation on the plate is given by $W(x, y, t)$ and the spring mass system is driven by $z(t)$. The paper makes two assumptions:

- $W(x, y, t) = w(x, y)e^{i\Omega t}$
- $z(t) = z_0 e^{i\Omega t}$

In other words, the paper assumes that all waves in the system are constructed by harmonics of the same frequency.

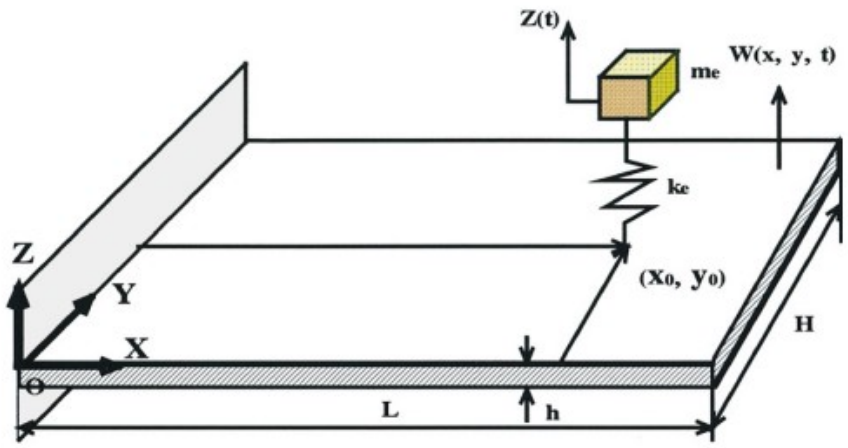

Figure 30: Schematic of a thin and isotropic cantilever plate, coupled with a spring mass system[55].

Chiba and Sugimoto first derive the Lagrangian L. To solve the spring mass system coupled to a cantilever plate, a version of eigenfunction expansion is used by making the following assumption:

$$\bar{w}(\zeta, \eta) = \sum_{m,n} \Big(a_{mn} \Phi_m \Psi_n \Big), \tag{2.24}$$

where $\zeta = \frac{x}{L}$, $\eta = \frac{y}{H}$ $\bar{w} = \frac{w}{L}$. Then classical mechanics to derive the mass matrix M and spring-constant matrix K in a simplified version of Equation 2.23 where C and F are zero. To understand the numerical solution offered by the paper, three constants must first be defined. The aspect ratio $\lambda = \frac{L}{H}$, the stiffness ratio $\alpha_{ke} = k_e \frac{L^2}{H}$ and the mass ratio $\alpha_{me} = \frac{m_e}{\rho H h L}$, where ρ is the density of the plate.

For an uncoupled system the natural frequency ω_0 of the plate changes as the aspect ratio changes, as shown in Figure 31a. Another result of the paper is shown in Figure 31b, where the vibrational modes are displayed for

a coupled system. In our paper we will try to reach similar results in our numerical model of a cantilever plate.

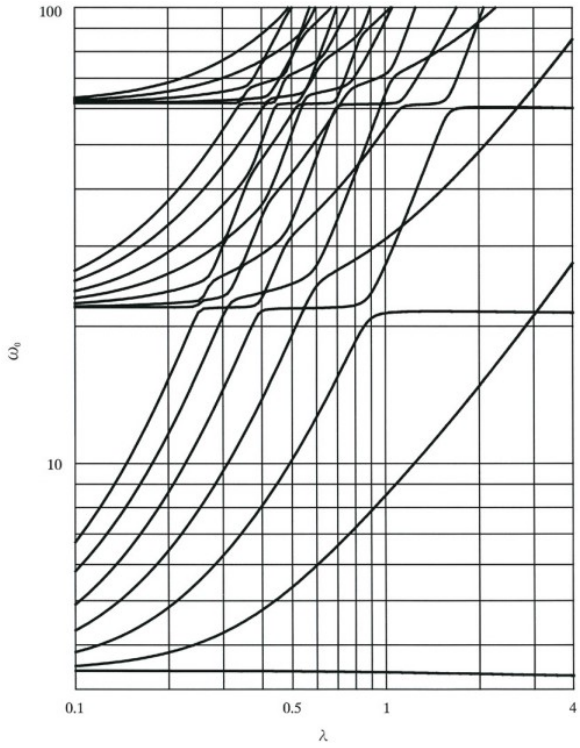

(a) The natural frequency of an uncoupled cantilever plate plotted against the aspect ratio λ.

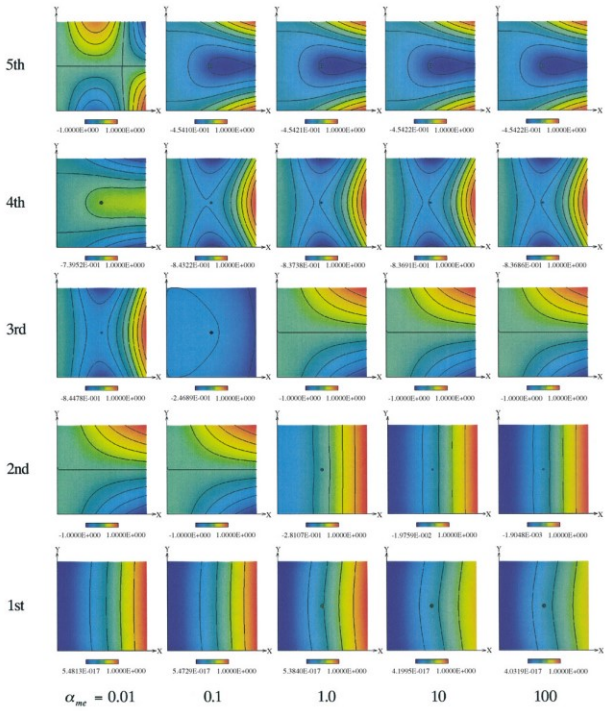

(b) The modes of a cantilever plate for the first five modes. The aspect ratio $\lambda = 1$, the stiffness ratio $\alpha_{ke} = 10$ and the mass ratio α_{me} is varied from 0.01 up to 100.

Figure 31: Two results[55], (a) showing the growing natural frequency ω_0 with respect to the aspect ratio, λ, for an uncoupled cantilever plate and (b) showing the first five vibrational modes for in a contour diagram for various mass ratios.

In Figure 31b, we see both symmetric modes and anti-symmetric modes. We also see the existence of quadrupole radiators (5_{th} mode for $\alpha_{me} = 0.01$). Additionally, the progression of the natural frequency is plotted against the aspect ratio λ, which can be tested against the results of our own model.

3 The model and its modelling cycles

In the Literature study, different models of the violin have been presented and tested using numerical packages; including *COMSOL*, *ABAQUS* and other programs. In this chapter, a create a model of the violin using the ideas, equations and methods provided by Chapter 2. The idea of the model is to start simple by dissecting the violin and consecutively simplifying the governing equations for the dynamics of the system. Through modelling cycles, increasing the realism and complexity in every iteration, we aim to get a model which will ultimately be able to point out differences between violins in relation to their radiated sound.

The violin consists of many different parts which are tightly bound or glued together; resulting in a tangled web of vibrations. As one can imagine, the components of the violin contribute in different ways to the radiated sound. Consequently, considering the most prevalent radiators solely and making the necessary assumptions, the model boils down to a relatively small selection of parts whose dynamics are governed by an adequate system of equations. This idea is coherent with most research on the radiation of the violin, which addresses one specific aspect of the violin in relation to the sound and timbre.

To construct the first iteration of the model, we will follow the following procedure:

Procedure for constructing a model of the violin

1. Introduction to the model and overview
2. Identifying parts and intertwining structures, defining the system and its subsystems
3. Making a selection of the parts, based on their individual effect on the radiated sound
4. Investigating the relation between all adjacent subsystems separately
5. Simplify the relevant subsystems and their relations to one another
6. Construct a model of the system using the simplifications

The rest of this section contains the introduction to the model and a general overview of the modelling cycle used to enhance the realism of the model. In section 3.1, the system is described with all its relevant subsystems which interact with each other. Steps 2, 3 and 4 in the modelling procedure overlap and intertwine. Hence they are discussed together, in section 3.2. The first iteration of the model is then constructed in the section 3.3.

As mentioned before, the idea is to start with an elementary model, gradually increasing the realism of the model in modelling cycles until satisfactory results are found. Doing so allows for a simple starting point which can be built upon, featuring corrections and adjustments in later versions of the model.

For the simplification of the violins' system and its subsystems (such as the corpus and the string), we make a number of assumptions for the relations between each pair of adjacent, hence coupled, subsystems and for the equations of motion. The model is made more realistic by removing the assumptions one by one in a new iteration of the model. As a result the governing equations become increasingly complex. Hence, this chapter provides a starting point, or first iteration of the model which can be built upon in later revisions of the model.

The aforementioned system contains several subsystems. Therefore, solving the equations of motions and assembling the subsystems should give us all the information needed. However, the system is more complex than meets the eye. Each "solution" to a subsystem is a variable or parameter to another subsystem due to the coupling between components. As a result, both feedback loops and intrinsic filters can exist in the system. Additionally, almost all of the governing equations for the dynamics of the individual subsystems are not analytically solvable.

Consequently, we will discuss a one dimensional form of the model, a beam, which can be used as test in the numerical model. Subsequently, we will attempt to find solutions for a bending plate numerically using the simplest version of the model in Chapter 4.

3.1 The system

The system of the violin is the collection of all its material components including its direct surroundings. Thus, the subsystems can be identified by travelling along with the signal, separating components of the violin with different vibrational behaviour.

Initially, the player bows the string, creating a signal which travels through the system where certain frequencies are amplified or damped. This can happen in several ways as the signal has multiple "ways" to reach the corpus and to eventually be turned into radiated sound.

Note that, for brevity, the far field radiated sound is reduced to a spherical symmetric plane wave. This shall be elaborated in the dissection of the subsystems

Firstly, the vibrations in the string cause differences in air pressure in the direct environment. These differences in air pressure travel radially outward and act as a source of longitudinal pressure waves (acoustic waves), as a response to the string, onto the top plate of the violin and into the corpus of the violin where the waves collide with the back plate. This causes the corpus to vibrate and consequently amplify or attenuate certain frequencies due to resonance and interference respectively. The resulting amplified acoustic waves in the corpus travel outside through the f-holes.

Secondly, the waves on the string cause tensions in the ends of the string where it is tied to the body of the violin. These tensions and the corresponding displacements on the string are then conducted to the bridge and pegs where the string is directly clamped and coiled respectively. The mechanical impedances of the bridge and pegs are dependent on the frequency. Hence, the bridge and pegs also act as a frequency filters; amplifying and attenuating the signal accordingly. The resulting vibrations will cause the corpus to vibrate and subsequently create sound waves with further amplification and attenuation.

Note that in both of these cases, the top plate, ribs and bottom plate are also connected to the environment and thus will cause acoustic waves themselves. On top of that, the acoustic waves inside the corpus continue to collide with the plates, ribs, bass bar and soundpost until they find their way out through the f-holes. In the same manner, the pegs and the bridge will also vibrate as a response to the corpus.

It follows that the system of a violin consists of five subsystems, four of which are pairwise coupled to one another. The different subsystems can be classified by their physical components and the resulting waves in the material. We denote the displacement of a material due to the transversal component of a wave as $\vec{U}$. Similarly, the pressure in a medium due to the longitudinal component of a wave is denoted as P. The system of the violin can then be summarised as follows:

System of the violin described in materials, displacements and pressures

- The string with $\vec{U_s}(x,t)$ being the displacement of the string with length L where x-axis is chosen along the unperturbed string.
- The air in a small ball encapsulating the violin at its origin, with $P_{air,str}(\vec{r},t)$ being the air pressure in the ball as a consequence of the vibrations in the string and corpus.
- The bridge, the pegs, $\vec{U}_{\partial,0}(t)$ and $\vec{U}_{\partial,L}(t)$,describing the displacement of the string at $x=0$ and $x=L$ (the boundaries of the string) as a result of tension in the string.
- The corpus with the displacement vectors $\vec{U}_{bp}, \vec{U}_{tp}, \vec{U}_{ribs}(\vec{r},t)$ of the bottom plate, the top plate and the ribs of the violin respectively.
- The far field with air pressure $P_{air,rad}(\vec{r},t)$ "far away from the violin".

Every subsystem in the system interacts with any other subsystem directly adjacent or connected to it. The interaction is always reciprocal. Hence, feedback loops are created.

Every subsystem amplifies and attenuates the signal based on the frequencies present in the signal. We construct the signal from the string with a superposition of sines. The subsystem transforming the superposition of sines is denoted by $W(f)$. The output of a system $W(f)$ can also be decomposed by a superposition of sines, if the

input is a superposition of sines.

First, the signal is initialised on the string, whereafter it travels through systems $W_1(f)$ and $W_2(f)$ as they are the direct surroundings of the string. $W_1(f)$ represents the boundaries of the string (the bridge and the pegs), connecting it to the corpus of the violin, $W_3(f)$. It follows that, $W_1(f)$ describes the mechanical impedance of the pegs and the bridge. Similarly, $W_2(f)$ is the name given to the fluidum in which the string is submersed. It serves no purpose other than to radiate the acoustic waves created by the string, boundary conditions and the corpus. A schematic of the system, showcasing the signal transfer between each subsystem, can be found in Figure 32.

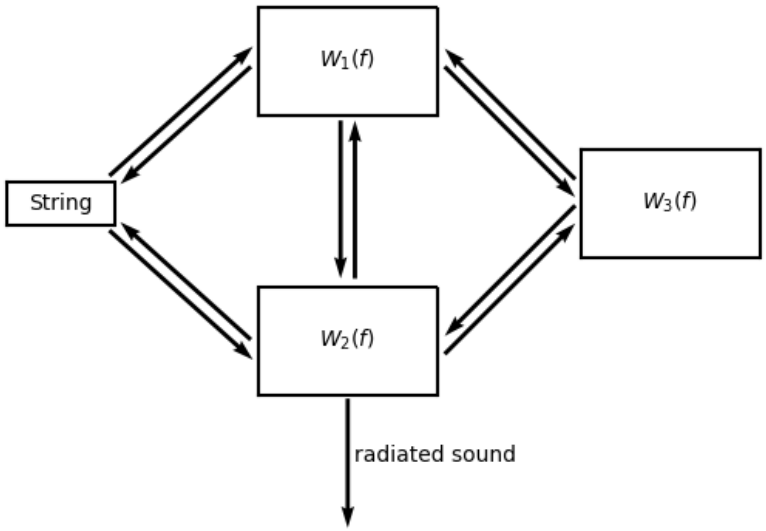

Figure 32: A schematic for the system of the violin, f is the frequency of the signal. The signal is initialised on the string. $W_1(f)$ represents the boundary conditions of the string, filtering the given frequencies of the input signal. $W_2(f)$ represents the air surrounding the string. $W_2(f)$ depends on the frequency weakly, rather it's main purpose is to radiate sound through the f-holes, into the environment of the violin. $W_3(f)$ represents the corpus of the violin. This subsystem also serves as a filter and it transforms the vibrational waves into acoustic waves.

Each subsystem is described by several equations based on the assumptions made, the coupling to other subsystems and its surroundings. Describing the systems equations and the relations between them at once will create a complicated structure of partial differential equations. Hence, describing the equations for the subsystems separately should allow us to find suitable tools for combining the subsystems and build the system in parts afterwards.

Each subsystem has an important role in the radiated sound. In theory, every ornament on the violin has an impact on the radiated sound. To simplify the system of partial differential equations describing the radiated sound, many ornaments and parts of the system are removed from the first iterations of the model. Despite the first version of the model being rather simplistic, the results should differ from the observed vibrational patterns shown in Chapter 2 too much.

3.2 Parts of interest and simplification of the system

As aforementioned, there is an important distinction to be made between the Components of the violin, to find out which are of interest and which are not. To make this distinction, we will take a look at the uniqueness of the individual violin. Namely, many components are not unique to the string family, let alone to the violin itself. An example of this is the string of the violin. Needless to say, the string of the violin is one of the most important and arguably *the* most important part of the violin. However, its material properties are not uniquely of importance in the timbre. The string can be replaced by a string with similar, but not the same, material properties without much alteration to the sound.

Similarly, there are many ways to induce waves on a string. One of which is to pluck the string. For the violin, this is called pizzicato (lit. pinched). When we pluck the string of a violin, this produces a sound. This sound is vastly different than the 'normal' sound of the violin. Therefore, vibrations in the string definitely have a significant effect of on the radiated sound. However, the aforementioned different techniques result in similar effects on different violins. Thus, whether the string should be included in the first model is still debatable. Before the decision is made, some other components must be discussed first.

We simplify the system of the violin in the following steps:

1. Argue that the air around the violin is not coupled to the violin itself and rather acts as a radiator of pressure waves only.
2. Argue that the air surrounding the violin and the far field can be merged into a single subsystem, carrying sound waves from the violin.
3. Argue that the Corpus is the main radiator of the violin.
4. Argue that the radiation can be approximated by the radiation of a point source.
5. Argue that the system does not contain feedback loops.
6. Argue that the bridge is the only conductor of waves from the string to the corpus.

Following these steps, Figure 32 is simplified to Figure 35.

1: To argue that the air around acts as a radiator of sound waves only, we note that the air surrounding the violin is also an important subsystem and it mainly serves two purposes. Firstly, it radiates the differences in air pressure, caused by vibrations in every material component of the violin directionally. This causes the directivity of the radiation mentioned in Chapter 2. Secondly, the vibrations in the material components are attenuated. Technically, the governing equation for the air pressure is coupled to the governing equations for the vibrations in the adjacent materials. However, when waves with different wave numbers interact with each other, energy is transferred and energy dissipation takes place. For a gases, such as air, the Reynolds number near vibrating plates is typically around $Re = 3300 - 17500$[56], being in the range of turbulent flow[57]. Hence, the pressure and drag force on the material is very small[58]. It follows that the coupling between the air and the plates is very weak. Thus the internal forces from the materials dominate with respect to the drag force caused by the air. In conclusion, the main purpose of the air directly surrounding the violin is to propagate the sound waves away from the vibrating subsystems.

2: Similarly, the medium around the violin can be merged with the far field since the coupling of the air with the material components of the violin is weak and the radiation of different subsystems do not influence other subsystems. As shown in Cremer, the string will not radiate sound strongly as its diameter is much smaller than the wavelength of the waves on the string. Therefore, the sound radiated by the string causes negligible vibrations in the corpus, since the internal morphological stresses of the wood dominate. Additionally, the radiated sound, caused by directly by the string, is also negligible. A similar argument can be made with respect to the bridge and the pegs. Furthermore, the bridge and pegs are directly coupled to the corpus, having the same filtering effect but strongly coupled. Hence, the medium around the violin does not propagate the radiated sound of subsystems to one another. Rather, it only radiates sound waves away from the violin and can therefore be merged with the far acoustic wave field.

3: We can consider the corpus the main radiator of the violin since the radiation caused by the string, bridge and pegs is not the only part of the system that can be removed from the system. The bridge is directly

connected to a surface which is much larger in comparison to the wavelength of the string. Thus the waves on the corpus of the violin will radiate the acoustic waves much more strongly. While not explicitly stated, the logic Cremer uses to consider radiation of the string can also be applied to most other details and ornaments on the violin. A supporting statement describing that: "'substructures'" are not proven to radiate significantly below a frequency of $4KHz$" is given by Bissinger. It follows that, in our model, the only radiation considered is now directly caused by the corpus of the violin. This means that $W_2(f)$ can be removed in the schematic of the system and the radiation can be directly connected to $W_3(f)$ without loss of generality. The revised schematic of the system, using the new assumptions and simplifications, can be found in Figure 33.

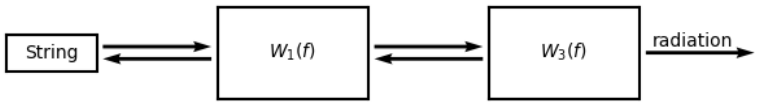

Figure 33: Schematic of the system of the violin when the air around the string and violin ($W_2(f)$) is removed as a subsystem. $W_1(f)$ is the subsystem representing the bridge and the pegs. $W_3(f)$ represents the corpus of the system.

4: As mentioned before, we must be careful when using the term "radiation". However, in the first iteration of the model, we will consider monopole radiation only. Namely, at first glance the monopole sound radiation only approximates the actual radiation taking place. This causes a problem in measuring radiated sound. However, this does not affect our system since we have argued that the corpus is the sole radiator of the violin. For plates, the most prevalent radiators at low frequency ($\leq 1kHz$)[26]: monopoles, dipoles and quadrapoles, tend to exhibit a similar behaviour. Namely, the pressure of the sound decays linearly with net distance to the sources in all three cases[59]. The only differences are the amplitude and the directivity of the dipole and quadrupole. As shown in Figure 7, the amplitude of the monopole radiation is much larger for frequencies below $\leq 1kHz$. Hence, in this iteration of the model, the directivity of sound waves is neglected. This reduces the radiation of the violin to the radiation of a point source. In later iterations of the model, the dipoles could be taken into account.

We must note that approximating the radiation with a monopole or dipole in the first versions of the model simulates most of the radiation pressure and neatly describes the radiation in modes. However, as shown in Chapter 2, (2.3.2.c), using modes to describe the perceived sound becomes less useful at higher frequencies. Namely, the radiated field cannot be described by simple poles anymore since the different acoustic wave fields will start to interfere with one another[26]. As a response, the directivity of the radiated waves cannot be approximated with methods commonly used for low frequencies. In later iterations of the model, the directivity of radiation, the statistical overlap factor and the modal overlap factor should be taken into account. However the analysis pertaining the interference of different fields is considered to be beyond the scope of this thesis.

5: Now we can argue that the system does not contain any feedback loops. Namely, Figure 33 gives a schematic of the reduced system of a violin. But it can be reduced even further. Namely, $W_1(f)$ acts as a filter for frequencies. Therefore, any allowed signal (any superposition of sine waves) that travels from $W_1(f)$ to $W_3(f)$ and back will only contain certain frequencies with amplified or attenuated amplitude. Note that this can only be true under the assumption that $W_1(f)$ and $W_3(f)$ do not alter the frequency band as a whole and only amplify or dampen the given frequencies. Another assumption is made: the mechanical impedances of the bridge and pegs are symmetrical with respect to the direction of the signal. It follows that, under the two aforementioned assumptions, the string will only receive the already filtered frequencies. Using superposition of waves on the string, the same frequencies will then be conducted back to $W_1(z)$ by the string, which pass through the filter again, with similar attenuation or amplification. Thus, it is safe to say the the feedback loops between the string, $W_1(z)$ and $W_3(z)$ as given in Figure 33 will only impact the amplitude of the already filtered frequencies but will not change the frequency band drastically. If it is assumed that the amplitudes returned by the string after coupling with the bridge and pegs are similar to the initial wave, the system can be represented without feedback loops. This is shown in Figure 34.

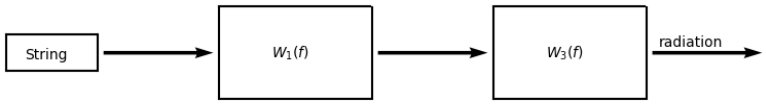

Figure 34: Schematic of the system of the violin with the feedback loops removed. $W_1(f)$ is the subsystem representing the bridge and the pegs. $W_3(f)$ represents the corpus of the system. The feedback loops can be removed using three assumptions: $W_1(f)$ and $W_3(f)$ do not alter the frequency bands, $W_1(f)$ works symmetrical and the amplitudes of waves on the string after the feedback loops are of similar magnitudes to the initial signal.

6: The last step is to remove the string and translate all the vibrations of the string directly to vibrations in the bridge, which acts as the dominant source, of bending waves, for the corpus. Because there are no feedback loops in the system, the vibrations in the string can be directly translated to vibrations in the boundary conditions. Additionally, the boundary of the vibrating string is not just given by the pegs and the bridge. At the far end from the violinist, the string is coiled around the pegs, but is also pressed against (not tied to) the fingerboard (the synthetic surface on top of the neck) due to the geometry of the violin. This means that most vibrations are transferred to the fingerboard as well as the pegs. Though, the indirect coupling of the corpus with the far end boundary of the string can be assumed to be small. Meaning that the amplitudes of the transversal waves in the string are of lesser amplitude near the far end of the string than near the bridge. Furthermore, even if the string was to be bowed or plucked near the far end, the vibrations are assumed to be attenuated enough due to the nature of the coupling with the corpus such that the vibrations through the bridge dominate. This assumption is made because the neck and fingerboard are connected to the ribs, and not to the bottom or top plates. Moreover this is coherent with the idea that the position of the bridge and the geometry of the bridge, allowing bending in the bridge itself as described in Chapter 2, cause the impedance to be smaller for certain frequencies. Hence, we assume that the vibrations conducted through bridge dominate with respect to the vibrations conducted through the pegs, which leads to the notion that, in low order approximations, the bridge is the only conductor of waves from the string to the corpus. The final schematic of the reduced system is shown in Figure 35. Note that $W_1(f)$ now only represents the bridge.

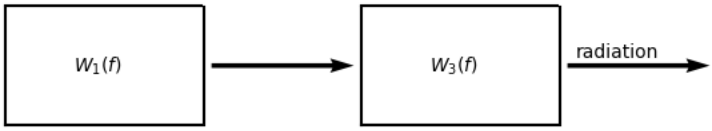

Figure 35: Schematic of the system of the violin with the feedback loops removed. $W_1(f)$ is the subsystem representing the bridge. $W_3(f)$ represents the corpus of the system. The string has been removed in the subsystems

We want to note that all assumptions made do influence the outcome for the acoustic waves. The most important assumptions made in the simplification process of the model are listed in Appendix B. With the current list of assumptions, we wouldn't be able to distinguish any two instruments from one another, as illustrated in Chapter 2. Even so, the model provides a construct to slowly but surely decrease the number of assumptions made and gradually increase the realism of the problem again, to the degree that two different instruments yield two distinguishable different results.

There are also many small parts which serve purposes such as tuning, making the violin playable, holding the violin together or are purely ornamental. Though these parts do certainly have an impact on the sound of the violin in question, they will not be considered of interest as the effect they have on the sound is rather negligible and often ambiguous.

Hence, the number of components in which we are interested is greatly reduced. These components mainly comprise the corpus and its boundary.

- the Bridge
- the Top plate
- the Back plate
- the Ribs
- the Bass bar
- the Sound post

A schematic of the components of the violin is shown in Appendix A.

Thus, we assume that the aforementioned components are the most important ones for the difference in sound. Therefore, these will parts will be the main focus when searching for the difference between a normal violin and a Stradivarius violin. Though, we must be careful. Since many parts with different contributions to the sound are not taken into account, there might be differences between the inspected instruments which we fail to observe.

3.3 Constructing the model

The most parts of the violin and the system used to describe the radiated sound have been determined. In this part, a number of decisions is made pertaining the precision of the first iteration of the model and the governing equations describing the dynamics of the violin. The previously made assumptions to simplify the model will assist in constructing the model as they provide a guideline for the vibrations.

After the signal has been initialised on the string, it is conducted to the corpus (Ansatz B.1.1). We already concluded that the bridge, described by $W_1(z)$ in Figure 35, is the most prevalent carrier of vibrations to the corpus (Ansatz B.3.1).

Since the wave on the string is solely comprised of harmonics (Ansatz B.2.1), bridge and consequently the corpus will also radiate solely with harmonics (Ansatz B.1.3). Specifically, for the first iteration of the model, we will consider a bridge which conducts a single harmonic to the corpus. The equation of motion for the bridge can be described by the bending of wood (Ansatz B.1.2). However, a better picture of its function is also described in the literature where the bridge acts as a filter and its admittance corresponds strongly to the radiated sound. To this extent, we propose that the bridge acts as either an sine wave, pressing on the top plate, or as a double mass spring system. We choose a double mass spring system because the bridge has two feet and the geometry of the 'side holes' in a bridge allow for movement with spring mass like behaviour. In both cases, the bridge is considered to have a single driving frequency which can be varied from $191Hz$ up to about $3500Hz$, which are the lowest and highest frequencies that can be played respectively.

The corpus receives a direct harmonic oscillatory pattern on the top plate. As described by the Literature study, thin plate theory is a good candidate to model a bending plate. There are two versions of the thin plate theory we have seen: isotropic plates and an-isotropic plates, where the latter is arguably a generalised version of the former. Note that the differences between Equation 2.18 and Equation 2.18 can be explained by an-isotropic except for a constant ρ, which is the density. We will touch upon this later. In the case of bending wood, it is very important to include an-isotropic properties due to the structure of wood. For this reason, we will use the adjusted version of eqs. (2.18) to (2.21) to model our plates. We will try to replicate the results shown by Gough (2013, 2015a, 2015b).

First, we will consider a rectangular plate without any attachments. Secondly, we will rectify the original shapes of the plates. Thirdly, the plates are connected using ribs. Lastly, other parts and ornaments will be added. Another result we try to replicate is are the results on the Cantilever plate (2.7). Though not entirely replicable, due to the differences in the methods used to determine a numerical solution, we will attempt to recreate the shape of the modes shown in Figure 31b.

Another result we will try to reproduce is a description of the grid for the whole body of a violin. In specific, we will try to mimic Figure 27 in an Euclidean space.

3.3.1 The bending wave equation

Suppose there exists some surface Ω in the (x, y)-plane with some function $U : \Omega \times \mathbb{R} \to \mathbb{R}$. U denotes the displacement in the z-direction on the surface over time. As aforementioned, the bending wave equation, or flexural wave equation, is given by

$$h\frac{\partial^2 U}{\partial t^2} + B_{xx}\frac{\partial^4 U}{\partial x^4} + 2B_{xy}\frac{\partial^4 U}{\partial x^2 \partial y^2} + B_{yy}\frac{\partial^4 U}{\partial y^4} = 0, \tag{3.1}$$

were, h is the thickness of the plate and B_{xx}, B_{xy} and B_{yy} are given by eqs. (2.19) to (2.21) and represent directional flexural rigidness. In a homogeneous plate, $B_{xx} = B_{xy} = B_{yy}$. If this is the case, the flexural wave equation is given by

$$\frac{\partial^2 U}{\partial t^2} + \frac{Eh^2}{12\rho(1-\nu^2)}\nabla^4 U = 0, \tag{3.2}$$

where E is Young's Modulus, h is the thickness, ρ is the density and ν is Poisson's ratio.

3.3.2 The Initial Value Problem

We have a partial differential equation. However, the initial value problem includes boundary conditions, initial conditions and external forces. Utility wise, a solution to the partial differential equation can generally be made unique by applying boundary conditions and initial conditions. We consider three different types of boundary conditions[28] for some $\vec{r}_{\partial\Omega} \in \partial\Omega$ and $t \in \mathbb{R}^+$:

1. A clamped end, where $U(\vec{r}_{\partial\Omega}, t) = 0$ and $D_{\vec{n}}U(\vec{r}_{\partial\Omega}, t) = 0$
2. A supported end, where $U(\vec{r}_{\partial\Omega}, t) = 0$ and $D^{(2)}_{\vec{n}}U(\vec{r}_{\partial\Omega}, t) = 0$
3. A free end, where $D^{(2)}_{\vec{n}}U(\vec{r}_{\partial\Omega}, t) = 0$ and $D^{(3)}_{\vec{n}}U(\vec{r}_{\partial\Omega}, t) = 0$,

where $D^{(k)}_{\vec{n}}U(\vec{r}_{\partial\Omega}, t)$ is the k_{th} directional derivative of $U(\vec{r}_{\partial\Omega}, t)$ with respect to $\vec{n} \in \mathbb{R}^2$. The vector $\vec{n}$ is always lies in the (x, y)-plane and is perpendicular to $\partial\Omega$ at the point $r_{\partial\Omega}$. The different types of boundary conditions are shown in Figure 36.

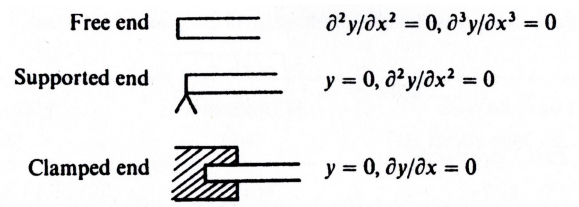

Figure 36: A schematic of the three boundary conditions used for bending bars and bending plates with the appropriate conditions imposed on the displacement y, after Neville H. Fletcher.

To avoid more complicated boundary conditions, we assume the violin to be played on an open string. Namely when considering the individual plates of the corpus, The free end and the clamped end are the most realistic for a violin played at an open string. However, the condition imposed by the hand on the fingerboard on the equation of motion is less straightforward when the violin is not being played at an open string. Since the non bowing hand does not grasp the fingerboard tightly, it cannot be described as a clamped end. The fingerboard could be said to be a supported end, however the direction of the support is dependent on the position of the hand. Even more, the corpus is directly held at the chin rest, but the non-bowing hand does not form a direct boundary condition for the corpus as the fingerboard connects the two. Thus, to prevent this ambiguity, we assume the violin to be played at an open string. This results in a free part of the boundary.

Note that the clamped end is also only true in some order of approximation since the head, shoulder and the non-bowing hand should be seen as coupled to the corpus. However, this leads to little or to no difference as opposed to the "analytically clamped" case since the mass of the head and the mass of the arm are many times greater than the mass of the total violin. Therefore, we assume that the vibrations are attenuated enough such that the coupling is not of interest.

For the initial conditions, suppose that the plate is in equilibrium at $t = 0$. This means that $\frac{\partial^i U}{\partial t^i}(\vec{r}, 0) = 0$ for every $i \in \mathbb{N}$ and $\vec{r} \in \text{int}(\Omega)$. For a plate in the (x, y)-plane without external forces, we must also have $U(\vec{r}, 0) = 0$.

If we allow for external force, such as gravity. The main governing equation is adjusted slightly. It becomes

$$h\frac{\partial^2 U}{\partial t^2} + B_{xx}\frac{\partial^4 U}{\partial x^4} + 2B_{xy}\frac{\partial^4 U}{\partial x^2 \partial y^2} + B_{yy}\frac{\partial^4 U}{\partial y^4} + hg = 0. \tag{3.3}$$

The derivation is analogous to the one given by Hörchens for bending waves in a bar. The equation of motion is based on the bending moment M over a small area with length Δx and width Δy. Therefore, when the whole equation is divided by the mass of the small area $h\rho\Delta x\Delta y$. All of the gravity which remains is the gravitational acceleration g. A better motivated version of the derivation is given in Appendix D. This result, where only the acceleration remains, can be generalised any external force.

If, instead, an oscillatory harmonic source, with Amplitude A_s, frequency ω_s and phase ϕ_s, is present at some $(x_s, y_s) \in \Omega$, the following condition is imposed on the equation of motion:

$$U(x_s, y_s, t) = A_s \sin(\omega_s t + \phi_s). \tag{3.4}$$

As mentioned before, the bridge can also function as a double mass spring system. Using the linear schematic of the system given by Figure 35, the mass spring system only drives the top plate. In that case, we have two sources. Each with slightly different amplitude, phase and frequency, denoted with an extra subscript 1 or 2 for each spring mass system respectively. The sources are then given by

$$\frac{\partial^2 U(x_{s,1}, y_{s,1}, t)}{\partial t^2} = A_{s,1} \sin(\omega_{s,1} t + \phi_{s,1}) \tag{3.5}$$

and

$$\frac{\partial^2 U(x_{s,2}, y_{s,2}, t)}{\partial t^2} = A_{s,2} \sin(\omega_{s,2} t + \phi_{s,2}) \tag{3.6}$$

respectively. This completes the initial value problem for a single plate. Consequently, we can now connect two plates to one another.

3.3.3 Coupled rectangular plates

Connecting two plates through the ribs, the soundpost and other smaller parts means that equations of motion for both plates become coupled. This coupling can happen in a multitude of ways. For example, the ribs could be incompressible. Another example is to assume the ribs have spring like behaviour, as suggested by Gough (2015a). We will will use the former option. We consider two separate plates Ω_{tp} and Ω_{bp}. Ω_{tp} is the surface of the top plate and Ω_{bp} is surface of the bottom plate. In order to keep the first iteration relatively simple, we try to neglect to coupling by choosing a leading plate and a reacting plate. The leading plate vibrates freely with the reacting plate being tied to it at the boundary by means of an incompressible material. Physically, this could mean that the top plate is magnitudes heavier than the bottom plate, causing this behaviour. Naturally, this is not the case in a violin. However, examining the behaviour of the reacting plate might give useful insight into coupling for further iterations of the model.

Using the idea of the leading and reacting plate, the top plate can be modelled with free ends. Let U_{tp} be the solution to the flexural wave equation on the top plate. The bottom plate then has clamped boundary conditions, with solution U_{bp}. The clamped boundary condition of the bottom plate, at some point $\vec{r}_{\partial\Omega} \in \partial\Omega$, is then given by

$$U_{bp}(\vec{r}_{\partial\Omega}, t) = U_{tp}(\vec{r}_{\partial\Omega}, t) \qquad D_{\bar{n}} U_{bp}(\vec{r}_{\partial\Omega}, t) = D_{\bar{n}} U_{tp}(\vec{r}_{\partial\Omega}, t). \tag{3.7}$$

For other parts of the violin, a similar condition can be imposed using the idea of a following and reacting plate. This manifolds as an external force in the bottom plate. If all the parts connecting the plates are viewed as incompressible, the bottom plate experiences a set deflection at places where the plates are connected according to the deflection of the top plate. Suppose the soundpost is set at position $\vec{r_{sp}} \in \text{int}(\Omega)$. The bottom plate can then be modelled with an extra source

$$U_{bp}(\vec{r_{sp}}, t) = U_{tp}(\vec{r_{sp}}, t). \tag{3.8}$$

3.4 Simplification to a Thin bending rod

When creating the finite difference model in Chapter 4, a one dimensional rod is considered first since the one dimensional flexural wave equation can be solved analytically in specific scenarios. The solutions found on the thin rod will be used to check whether the finite difference model of square plates yield a similar results.

Let a thin rod lay along the x-direction with length $L \in \mathbb{R}^+$, Young's modulus $E \in \mathbb{R}^+$, radius $a \in \mathbb{R}^+$, radius of gyration $K = \frac{a}{2}$ for a thin rod[28] and density $\rho \in \mathbb{R}^+$. The equation of motion for a bending rod is very similar to the equation of motion of a thin bending plate. It reads as follows[28]:

$$\frac{\partial^2 U}{\partial t^2} = -\frac{EK^2}{\rho}\frac{\partial^4 U}{\partial x^4}, \tag{3.9}$$

Where U is the displacement along the z-axis. The boundary conditions are also very similar. We assume that one end is clamped and one end is free, as is the will help us in the boundary conditions for more complex problems. To specify, at $x = 0$, there is a clamped end and at $x = L$, there is a free end. The boundary conditions thus read[28]:

$$U(0) = 0, \tag{3.10}$$

$$\frac{\partial U}{\partial x}\Big|_{x=0} = 0, \tag{3.11}$$

$$\frac{\partial^2 U}{\partial x^2}\Big|_{x=L} = 0 \tag{3.12}$$

and

$$\frac{\partial^3 U}{\partial x^3}\Big|_{x=L} = 0. \tag{3.13}$$

If we consider the steady state solution, meaning $\frac{\partial U}{\partial t} = 0$, we obtain

$$U = -\Big(\frac{\rho\hat{g}}{24EK^2}\Big)x^4 + \Big(\frac{L\rho\hat{g}}{6EK^2}\Big)x^3 - \Big(\frac{L^2\rho\hat{g}}{4EK^2}\Big)x^2. \tag{3.14}$$

4 Finite Differences and method of lines

The goal of this chapter is to use the finite difference equations, as provided in Appendix F, to simulate the dynamics of the corpus.

The numerical model is constructed in steps. This is the case to make sure that mistakes in the implementation can be traced back more easily. First, we consider a thin bending rod with length L as described by Equation 3.9 in steady state, meaning $\frac{\partial U}{\partial t} = 0$. Including gravity as the external force yields

$$\frac{EK^2}{\rho}\frac{\partial^4 U}{\partial x^4} = -g, \tag{4.1}$$

with a clamped boundary at $x = 0$ and a free boundary at $x = L$, as shown in Figure 37. This gives us the tools to check how the one dimensional time independent case compares to the analytical result. Second we consider Equation 3.3 in steady state. We obtain

$$B_{xx}\frac{\partial^4 U}{\partial x^4} + 2B_{xy}\frac{\partial^4 U}{\partial x^2 \partial y^2} + B_{yy}\frac{\partial^4 U}{\partial y^4} = -hg. \tag{4.2}$$

The schematic corresponding to the two dimensional plate is given by Figure 38, where a totally clamped plate is shown. Other configurations of the boundary conditions including free ends can also be implemented in a similar manner to Figure 37.

After both steady state solutions are shown to be accurate, we move on to the time dependent flexural wave equations. For the rod, the flexural wave equation is given by

$$\frac{\partial^2 U}{\partial t^2} + \frac{EK^2}{\rho}\frac{\partial^4 U}{\partial x^4} - \zeta\frac{\partial U}{\partial t} = f, \tag{4.3}$$

where $\zeta > 0$ is some damping constant to disperse energy from the system if needed and f is the unit force. Similarly, the bending wave equation on the plate is given by

$$h\frac{\partial^2 U}{\partial t^2} + B_{xx}\frac{\partial^4 U}{\partial x^4} + 2B_{xy}\frac{\partial^4 U}{\partial x^2 \partial y^2} + B_{yy}\frac{\partial^4 U}{\partial y^4} - \xi\frac{\partial U}{\partial t} = f, \tag{4.4}$$

with ξ a similar dampening constant and f the unit force on the plate.

In both cases, we two different unit forces. The first one caused by gravity, to inspect if the rod and plate converge to their equilibrium state. The second one caused by a source of the form

$$f(\vec{r}) = \begin{cases} A_s \sin(\omega_s t + \phi_s) & , \vec{r} = \vec{r_s}, \\ 0 & , \vec{r} \neq \vec{r_s}, \end{cases} \tag{4.5}$$

for some source point on the grid $\vec{r_s}$, amplitude A_s, frequency ω_s and phase ϕ_s. This is the simplest case of the model discussed in Chapter 3, where the bridge is assumed to conduct a perfectly harmonic signal to the top plate. The top plate is a square without f-holes and is not connected to the ribs.

4.1 Stationary cantilever beam

4.1.1 Designing the grid

To model this problem, we will use the central differences and numerical methods as described by C. Vuik and Vuik. A summary of the difference equations we needed for the model can be found in Appendix F. We divide the rod into $n \in \mathbb{N}$ parts. At each end of a part exists a node. It follows that there are $n + 1$ nodes to describe the rod, forming a one dimensional grid. The idea is to apply Equation 3.9 to each node. We can visualise the nodes as points along the x-axis where the rod exists and the rod is described by Equation 3.9 at these points. Of course, the equation of motion also holds in between the points. Therefore, in an ideal case, we should have an infinite number of points between and including $x = 0$ and $x = L$. But this is not numerically possible. For this model, we will assume each point on the grid $x_i \in [0, L]$ to be equally spaced with some distance $\Delta x = \frac{L}{n}$. It follows that $x_i = i\Delta x$ for $i \in \{0, 1, 2, ..., n-1, n\}$. A schematic of the rod is shown in Figure 37.

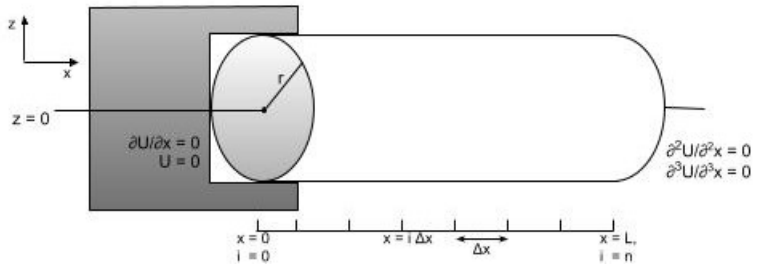

Figure 37: A schematic of the rod with its boundary conditions with the numerical grid shown beneath.

If we want to apply the central difference equation to our grid, we must be careful at the boundaries as the 4_{th} order central difference equation contains $f(x+\Delta x), f(x+2\Delta x), f(x-\Delta x), f(x-2\Delta x)$, translating to x_{n+2}, x_{n+1}, x_{-1} and x_{-2}. These points do not exist in the grid and are therefore called ghost points. If we try to directly apply the bending wave equation at the boundaries, we would either need to create new points, or we would get ambiguous results. However, this problem is solved by using the boundary conditions given by Equation 3.10.

4.1.2 The Stiffness matrix

We will loosely follow a method called "method of lines", described by van Kan. It describes how the problem

$$\frac{\partial U}{\partial t} + \frac{\partial^2 U}{\partial x^2} + q = 0, \tag{4.6}$$

where q is some sufficiently smooth function, can be described written down as

$$I\frac{\partial \vec{\omega}}{\partial t} + S\vec{\omega} + \vec{f} = 0, \tag{4.7}$$

with I the mass matrix, S the stiffness matrix, $\vec{\omega}$ the numerical approximation of y and $\vec{f}$ the approximation of q. Note that the stiffness matrix is determined by the partial differential equations, expressed in difference equations.

We rewrite Equation 4.1 to

$$S\vec{\omega} + \vec{f} = 0, \tag{4.8}$$

where $\vec{\omega} = [U_0, U_1, ..., U_{n-1}, U_n]^T$, $f = [q_0, q_1, ..., q_{n-1}, q_n]^T$ and S is the stiffness matrix. Each row in the matrix vector equation describes the numerical equation for one grid point. However, we do not have a description for every grid point yet. At both ends of the rod, the fourth order central difference equation contains points outside of the grid, ghost points. These points can be removed with using the boundary conditions to create a linear combination for points outside the grid of points in the grid. The derivation of S is given in Appendix G. For a cantilever beam, having a clamped end at $x = 0$ and a free end at $x = L$, we obtain

$$S = \frac{1}{(\Delta x)^4}\begin{bmatrix} 0 & 0 & 0 & 0 & 0 & 0 & 0 & 0 & \dots & 0 \\ 0 & 7 & -4 & 1 & 0 & 0 & 0 & 0 & \dots & 0 \\ 0 & -4 & 6 & -4 & 1 & 0 & 0 & 0 & \dots & 0 \\ 0 & 1 & -4 & 6 & -4 & 1 & 0 & 0 & \dots & 0 \\ 0 & 0 & 1 & -4 & 6 & -4 & 1 & 0 & \dots & 0 \\ \vdots & \vdots & \vdots & \vdots & \vdots & \vdots & \vdots & \vdots & \ddots & 0 \\ 0 & 0 & \dots & 0 & 1 & -4 & 6 & -4 & 1 & 0 \\ 0 & 0 & \dots & 0 & 0 & 1 & -4 & 6 & -4 & 1 \\ 0 & 0 & \dots & 0 & 0 & 0 & 1 & -4 & 5 & -2 \\ 0 & 0 & \dots & 0 & 0 & 0 & 1 & 0 & -3 & 2 \end{bmatrix}. \tag{4.9}$$

Using this stiffness matrix, we obtain a force $f_i = \frac{\rho g}{EK^2}$, where g is the constant gravitational acceleration.

4.2 Formulating the two dimensional method

We have seen a one dimensional rod in equilibrium. We are now going to consider the flexural wave equation, as given in Equation 4.2, on a thin plate. On a plate without any external forces, the flexural wave equation would be separable. Though, this implies that the displacement of the plate is zero everywhere (except in very specific cases).

The numerical implementation we have seen before does not directly apply to the two dimensional plate. For a plate, there are two spatial indices as opposed to one in the case of a one dimensional rod. This poses a problem for the matrix S as it does not allow for more than one spatial index. van Kan fixes this problem by combining the two spatial indices into one.

Let the plate be described by the surface $\Omega = \{(x, y) \in [0, L] \times [0, H]\}$ with its normal vector, in vacuo, parallel to the z-axis. The numerical grid is a constructed of equally spaced lines in the x-direction and equally spaced lines in the y-direction. The intersection of the lines are the grid points, or nodes. Let $n+1$ be the number of lines in the x-direction and $m+1$ the distance number of lines in the y-direction. Let $\Delta x = \frac{L}{n}$ and let $\Delta y = \frac{W}{m}$. We obtain $(x_i, y_j) = (i\Delta x, j\Delta y)$ for $(i, k) \in (\{0, 1, ..., n-1, n\} \times \{0, 1, ..., m-1, m\})$. The grid is shown in Figure 38. In this specific case, every boundary is clamped.

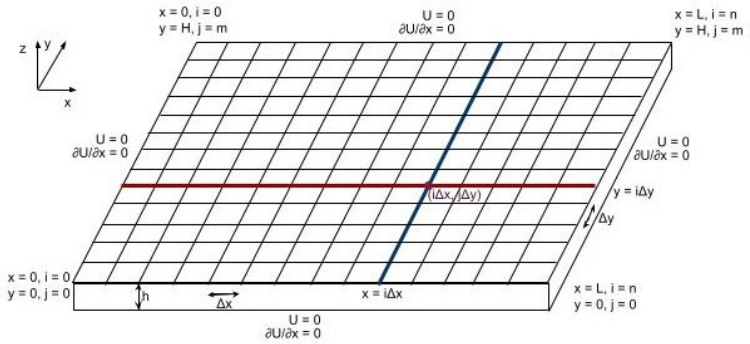

Figure 38: A schematic of the plate with clamped boundaries on the numerical grid for a plate.

Then, we renumber the grid points such that we only have one spatial index α. In essence, this can be done using any bijective map $\alpha_\infty : \mathbb{N}^2 \to \mathbb{N}$. This is the case since the index $\alpha \in \mathbb{N}$ should represent a unique combination $(i, j) \in \mathbb{N}^2$. For a finite grid, since we do not have to account for the cardinality of sets, we can construct a bijective function: $\alpha : \Omega_{num} \to \mathbb{N}$ with $\alpha = i + j(n+1)$. This is called horizontal numbering[63]. We can interpret α as walking along the path of i, then jumping to the row above it and once again, starting from the beginning and walking along the path of i. It follows that the $\alpha(i, j) - \alpha(i-1, j) = 1$, for $(i, j) \in \{1, 2, ..., n-1, n\} \times \{0, 1, ..., m-1, m\}$ and $\alpha(i, j) - \alpha(i, j-1) = n+1$ for$(i, j) \in \{0, 1, ..., n-1, n\} \times \{1, 2, ..., m-1, m\}$. With the numbering of the grid points accounted for, the two dimensional method problem is similar to the method for a one dimensional problem. The coefficients for the stiffness matrix are calculated in Appendix H in terms of the i, j-indices. The translation to α is done in the implementation of the numerical model.

4.3 Time-dependent numerical approximations

Now we are ready to implement the time dependent part of the equation. Since we have generalised the indices of the two dimensional problem to a single index, the following integration methods can be used for both the rod and the plate. Also notice that the time dependent equation contains a second order time derivative. We propose the use forward Euler integration scheme. The numerical equation is given by

$$I\frac{\partial^2 \vec{\omega}}{\partial t^2} - C\frac{\partial \vec{\omega}}{\partial t} + S\vec{\omega} + \vec{f} = 0, \tag{4.10}$$

where C is the dampening matrix. We can write this to

$$\left(I\frac{\partial}{\partial t} - C\right)\frac{\partial \vec{\omega}}{\partial t} + S\vec{\omega} + \vec{f} = 0. \tag{4.11}$$

If we let $\vec{\nu} = \frac{\partial \vec{\omega}}{\partial t}$, we can split the expression into two parts with

$$\frac{\partial \vec{\omega}}{\partial t} = \vec{\nu} \tag{4.12}$$

and

$$\left(I\frac{\partial}{\partial t} - C\right)\vec{\nu} = -S\vec{\omega} - \vec{f}. \tag{4.13}$$

We divide the time domain into steps with a duration of Δt. Thus we get $t_j = k\Delta t + t_0$. We let $t_0 = 0$. We denote the k_{th} time step with a superscript. Using the forward Euler method[61], we can rewrite Equation 4.12 and Equation 4.13 to

$$\frac{\vec{\omega}^{k+1}}{\Delta t} = \frac{\vec{\omega}^{k}}{\Delta t} + \vec{\nu}^{k} \tag{4.14}$$

and

$$I\frac{\vec{\nu}^{k+1}}{\Delta t} = \left(\frac{I}{\Delta t} + C\right)\nu^{k} - S\vec{\omega}^{k} - \vec{f}^{k}. \tag{4.15}$$

To solve this system of equations, we need two initial conditions for ω and ν. Suppose the rod begins without any deviation from its central axis. Then the initial displacement is zero and the initial velocity is zero. Hence $\vec{\omega}^0 = \vec{0}$ and $\vec{\nu}^0 = \vec{0}$ respectively.

5 Results and Discussion

Using the finite difference equations and the method of lines shown in section 4, we have generated the displacement for several plates and for a bending rod. First, the results for the steady state cantilever beam are shown. Then the results for the steady state cantilever plate and totally clamped plate are shown. Next, the time dependent results for the cantilever beam are shown whereafter the time dependent results for the cantilever plate are shown.

For the whole results and discussion, two different colour maps are used. The first colour map ranges from dark purple to green and finally to yellow, and is solely used to indicate curvature in the plot. The second colour map ranges from black to red and also to yellow. This colour map indicates displacement. The displacement is $0m$ near black and reaches $5.6 \cdot 10^{-5}m$, indicated by yellow.

5.1 Results for a cantilever beam in equilibrium

We consider a one dimensional and time independent rod. We compare the analytical solution and the numerical solution in Figure 39. In both solutions, $E = 11 \cdot 10^9 Pa$[64], $\rho = 500kg/m^3$[65], $r = 0.1m$, $K = 0.05m$ and $L = 1m$ were used. For the numerical solution, a step size of $\Delta x = 0.0002m$ was used.

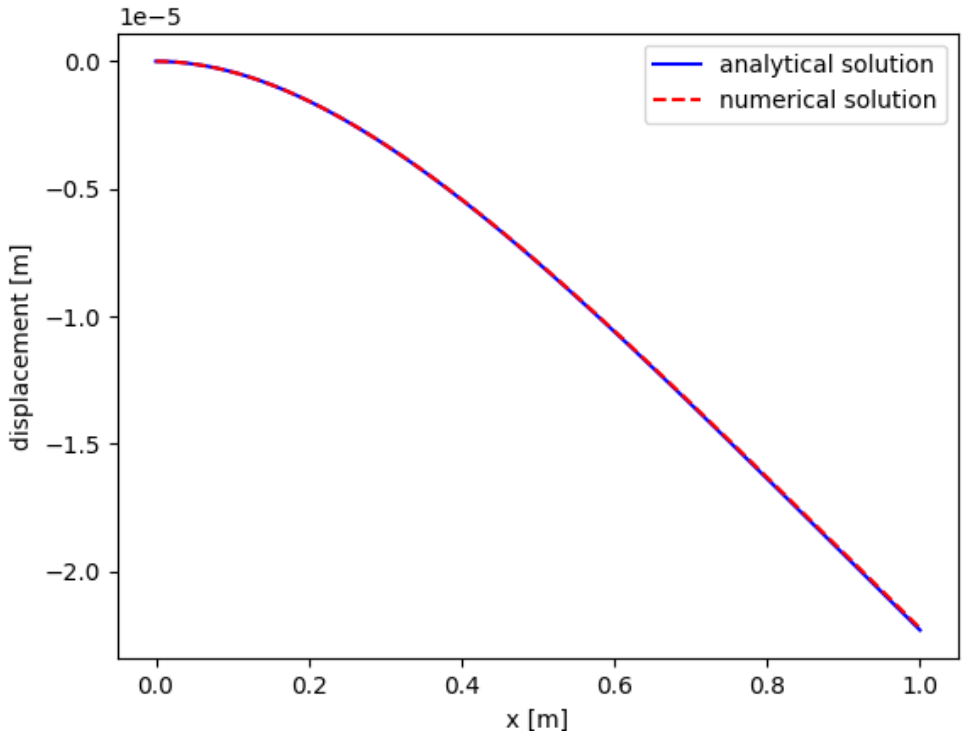

Figure 39: A plot of a cantilever beam modelled as a one dimensional rod with only gravity as an external force. The analytical solution is plotted against the numerical solution.

The numerical solution largely agrees with the analytical solution. However, the accuracy of the numerical model is dependent on a number of components. Therefore, we analyse the absolute error, $U_{analytic} - U_{numerical}$, and the relative error, $\left|\frac{U_{analytic} - U_{numerical}}{U_{analytic}}\right|$, of the numerical model in comparison to the analytical solution. Figure 40 shows the absolute error and the relative error. The left most plot shows the absolute error, the middle plot shows the relative error and the right plot shows the relative error with the first five points removed. As Figure 40 shows, the absolute error increases if we approach the free end. This is the case since the finite difference model sets the edge at 0 for a clamped end. Namely, $\omega_0 = 0$ is set without any further calculation. Thus, the absolute error at ω_0 is exactly equal to U_{x_0}, which is zero. For other nodes, the more we spatially move away from the clamped boundary, more calculations are needed. This suggests that the absolute error increases when moving away from $x = 0$ since the truncation errors of each difference equation add up with each calculation. This depends on the algorithm used to used to solve the matrix vector equation. For solving our numerical

model, we have used the linear algebra package of the *NUMPY*[66] library which uses the *LAPACK* routine[67].

The relative error is very large for ω_3, ω_4 and ω_5. This is the case since it is calculated by $e_r = |\frac{U_{analytic} - U_{numerical}}{u_{analytic}}|$, where U is the displacement with respect to the $x - axis$. The points x_3, x_4 and x_5 are very close to zero, thus we divide by a number which is very close to zero, causing a spike near the clamped end. In the right plot of Figure 40, the first five nodes are removed to avoid this behaviour. It shows that, except for nodes near the clamped boundary, the relative error is smaller than 0.01.

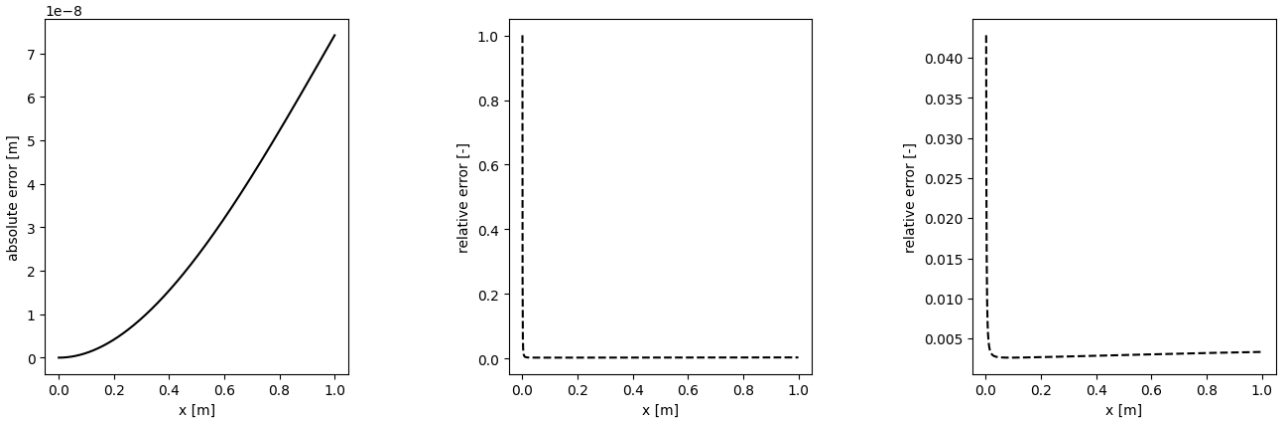

Figure 40: Plots of the absolute error (left), relative error(middle) and sliced relative error(right) for the one dimensional cantilever beam. The sliced relative error is the same as the normal relative error, but with the first five nodes removed.

The error of the numerical model is caused by several factors. In specific, there are two major factors. First and foremost, the step size of the grid, which directly impacts the accuracy of the numerical model. Figure 41 shows the evolution of the relative error along the cantilever beam over step size. Note that the smallest number of steps is four. Namely, below four, the boundary conditions cross over one another in the finite difference model and the matrix vector equation cannot always be solved.

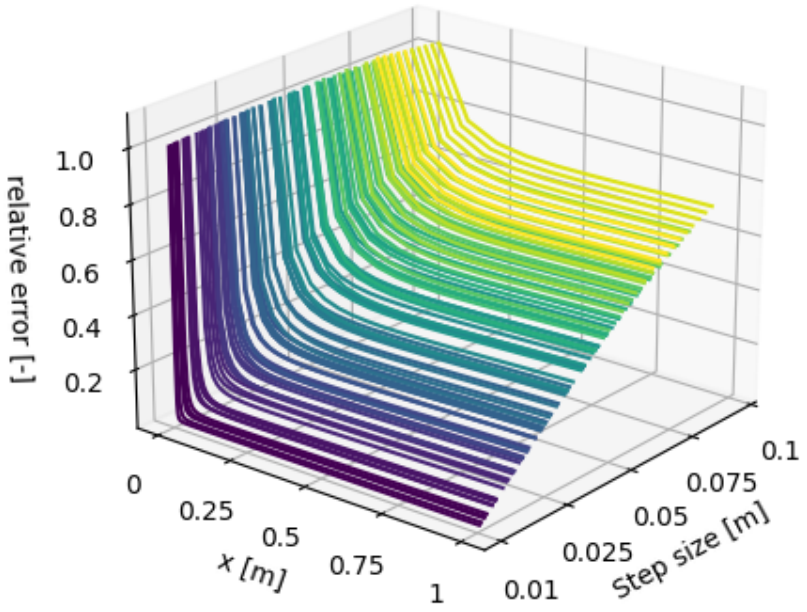

Figure 41: A plot of the step size against the relative error along the one dimensional rod. Note that the colour scheme is solely used to enhance the visibility of the curvature in the plot.

We see that, the step size is positively correlated to the relative error. This can be explained by the fact that the truncation error is $\mathcal{O}((\Delta x)^4)$. Since the elastic properties of wood do not allow for large displacements in

the wood, as we have seen by the scale in Figure 39, a step size of $\Delta x = 0.01$ yields a larger truncation error, being $\mathcal{O}(10^{-4})$, than analytical displacement, being $\mathcal{O}(10^{-5})$. This can be seen in Figure 41 at a step size of $0.1m$ with a relative error $e_r \approx 0.65$. This means that the results of the model can be up to 65 percent larger or smaller than the actual value. However for a step size of $0.001m$, the results fall within a one percent margin of the analytical solution.

We have inspected a rather small problem. For problems on a (spatially) larger scale, the ratio $\Delta x = \frac{L}{n}$ increases, causing the relative error to increase accordingly. To decrease this error, we can increase the number of grid points linearly with the spatial expansion. However, there is a second way to decrease the error, which is using difference formulas with a smaller truncation error, which is the second major factor in determining the error. This may be of advantage as computers do not always cannot always allocate enough memory for a larger number of steps. This can be especially seen since the stiffness matrix, in our dimensional problem, has size $(n+1) \times (n+1)$, but the stiffness matrix of a two dimensional problem with grid size $(m+1, n+1)$ has a stiffness matrix of size $(m+1)(n+1) \times (m+1)(n+1)$. Therefore, if we take one hundred steps in both directions, which is necessary to get within a relative error of one percent, we obtain a matrix with 10^8 elements. All of these elements are 64 bit floating point numbers, our double precision floating points, as this is automatically the case in Python. This already results in a data structure of at around 0.77 gigabytes, depending on the way the data is saved. This does not seem that large as most computers can allocate multiple gigabytes in memory if needed, but it scales with a factor 10^4 every time the grid size is decreased by a factor 10. For example, a grid with a thousand points in each direction would takes up roughly 7.41 terabytes using numpy arrays. Though, this number can decrease drastically if, for example, Sparse matrices are used to save the data.

Another reason why increasing the number of steps to decrease the error must be used with caution is that the time complexity of the *LAPACK* algorithm is $\mathcal{O}(k^3)$ for a $k \times k$ matrix. However, the matrix to be solved for a two dimensional model of a plate is $(n+1)(m+1) \times (n+1)(m+1)$. Thus the time complexity of the *LAPACK* algorithm becomes $\mathcal{O}(n^6)$ for $n \approx m$.

5.2 Results for a two dimensional plate in equilibrium

For a plate in equilibrium, we discuss three different scenarios: a totally free plate, a cantilever plate and a totally clamped plate. In all three different cases, gravity is the sole force causing a displacement at any point on the plate. For the numerical simulation of steady state plates, $E = 11 \cdot 10^9 Pa$, $\rho = 500 kg/m^3$, $\nu = 0.31$[68] and $h = 0.01m$ were used. Additionally, $L = H = 1m$ and $\Delta x = \Delta y = 0.01$.

The totally free plate yields the trivial solution, which tells us that there are no unexpected forces in the system. The numerical model has no solution to the matrix vector equation.

A cantilever plate was considered with the only free end being located at $x = 0$. As predicted beforehand, without in homogeneous forces in the y-direction, $\frac{\partial U}{\partial y} = 0$ everywhere on the plate. This is shown in Figure 42. Both plots show the same result. The left plot has an emphasis on the curvature of the plate and the right plot shows the displacement in terms of colour differences.

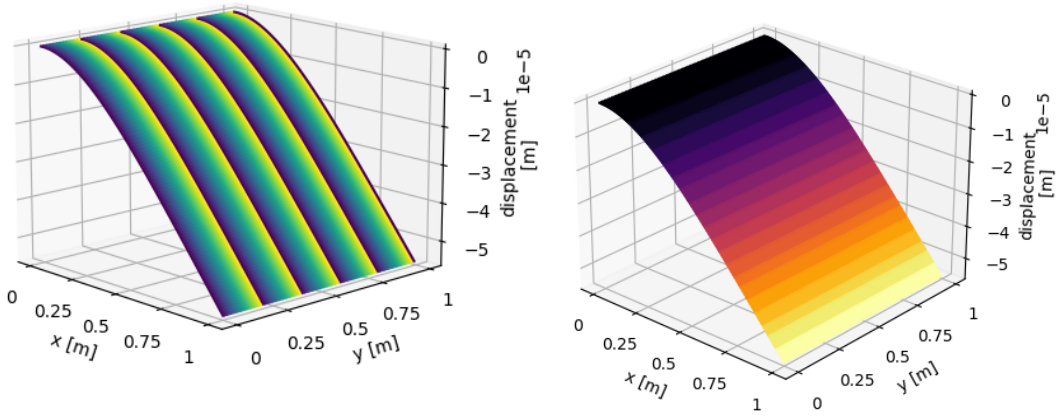

Figure 42: Numerically found displacement of a cantilever plate in a gravitational field. In the left figure, the curvature is shown and in the right figure, the displacement is shown.

For the cantilever plate, $\frac{\partial U}{\partial y} = 0$ at $x = 0$. It follows that, if no in-homogeneous force is applied to the plate and no in-homogeneous initial condition is set, $\frac{\partial U}{\partial y} = 0$ everywhere. When the external force consist solely of gravity, the plate will behave like a two dimensional extension of the one dimensional beam; one where multiple cantilever beams are glued together along the y-direction. In Figure 43, the result displacement is plotted against the x-axis. This is plotted against the analytic solution, ignoring the y-axis, and the numerical solution of the cantilever beam. The numerical solution from the rod is scaled with $3(1 - \nu^2)$ to fit the parameters in the bending wave equation.

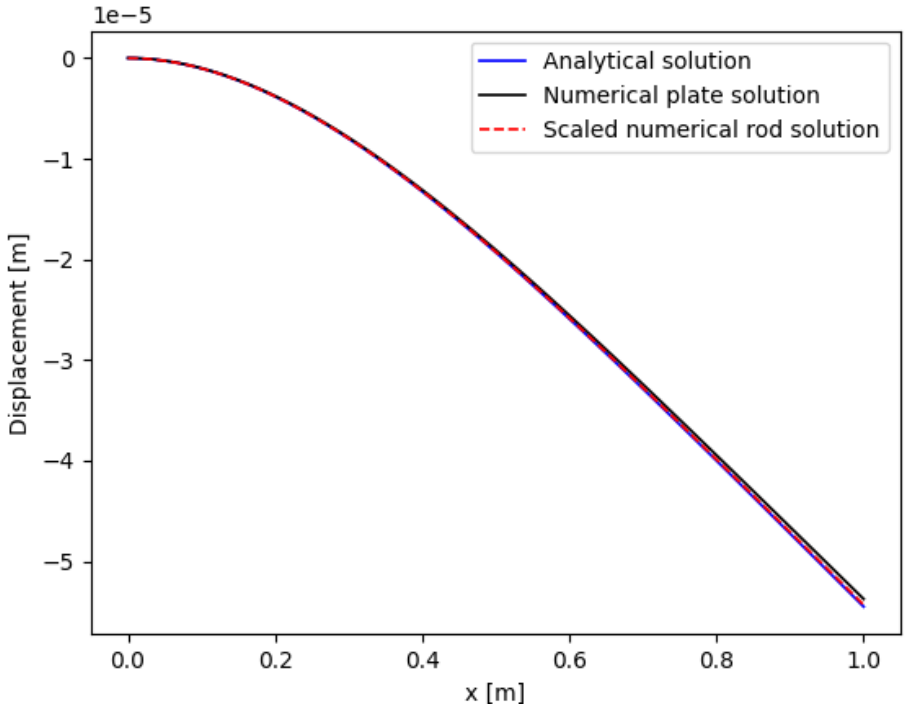

Figure 43: The numerical solution of the cantilever beam plotted against the analytic solution when the y-axis is ignored and against the solution of the cantilever beam which was scaled with $3(1 - \nu^2)$.

As we can see, both the curvature and the magnitude of the numerical solution to the cantilever plate match up with the analytical solution. However, the error of the cantilever plate with respect to the analytical solution is slightly larger than the error of the scaled cantilever beam with respect to the analytical solution. This error is shown in Figure 44.

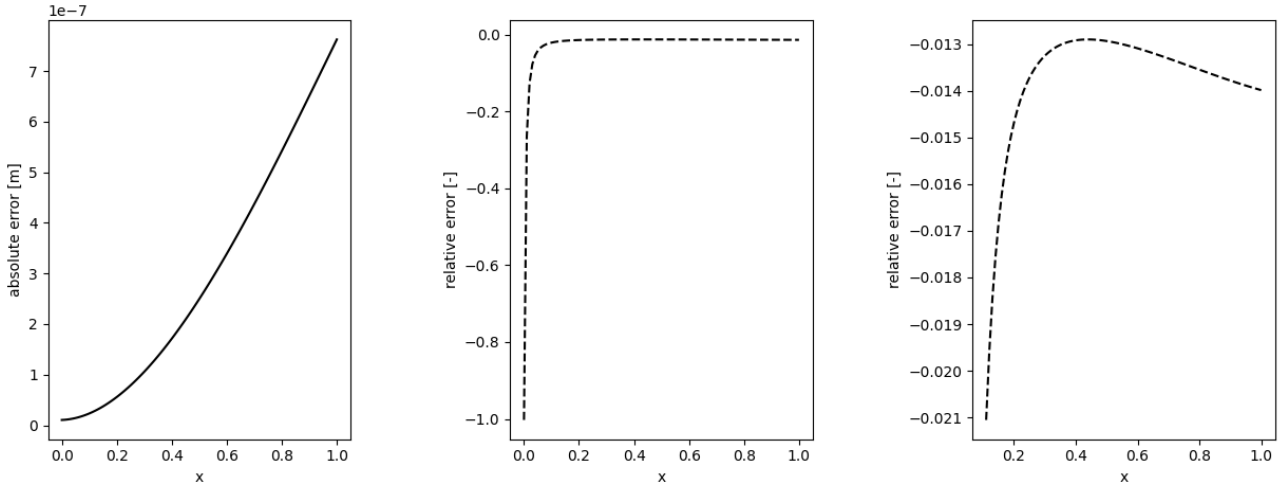

Figure 44: The absolute error and relative of the cantilever plate solution with respect to the analytical solution, disregarding the y-direction. The left plot shows the absolute error and both the middle and the right plot show the relative error. The right plot, however, has the first five points removed to increase visibility.

Once again, the error is quite small. Though, the relative error is larger than 1 percentage everywhere. Hence, there is room for improvement. This is especially the case since the spatial grid has steps of $1cm$, corresponding to a hundred steps. As shown in Figure 41, the step size makes a huge difference in error. Since the stiffness matrix was implemented using difference equations of the same truncation order error, we can quite reasonably assume that a similar relation exists for the cantilever plate. However we cannot plot this as this would take up too much space and would take a long time. To get the same plot, we would need a grid with ten times as many steps in each direction. Using the *LAPACK* algorithm, this would take 10^6 times as long. Therefore, using higher order difference equations is advised for further iterations of the model.

For the totally clamped plate, we expect the middle to have a larger displacement towards the middle. The numerical solution is shown in Figure 45.

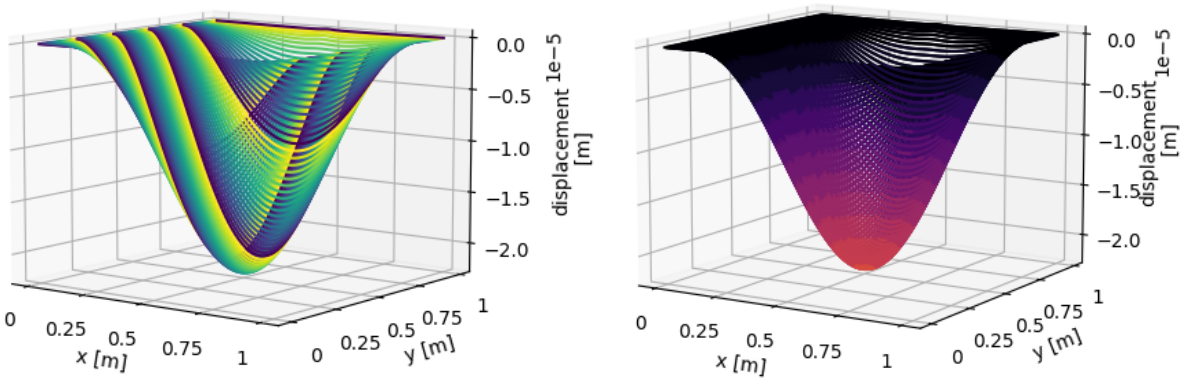

Figure 45: Numerically found displacement of a totally clamped plate in a gravitational field. The left plot indicates the curvature while the right plot shows the displacement in its colour map.

It is notable that the clamped plate shows a displacement which is a bit smaller than half of the cantilever plate. From a physical perspective, this is logical as the curve down and up in one direction are dictated, by symmetry, to take use exactly half of the plates length or width. Additionally, the plate cannot curve down completely as the derivatives with respect to the x- and y-direction of the solution are required to be continuous everywhere except for the boundary.

The steady state solutions we have seen up until now are coherent with the theory and with steady state solutions found in literature. Due to the nature of the force, the totally clamped plate resembles the breathing mode. If this force was switched in side ever so often, the breathing mode would be obtained.

5.3 Time-dependent results

There are two different versions of numerical solutions. The first kind only incorporates gravity as external force. We can compare the results to the steady state solutions. The second kind only incorporates a source in the middle of the plate. This source drives the plate with $U_s(\vec{r}_s) = A_s \sin(\omega_s t + \phi_s)$.

For the first time dependent analysis, $g = 9.81 m/s^2$ was used and for the second time dependent analysis, $A_s = 1 m/s^2$, $\omega_s = 440 Hz$ and $\phi_s = 0$ were used. The dampening constants ζ and ξ were only included to prevent divergence.

The results for the cantilever beam and cantilever plate are shown in Figure 46. The left plot shows the results for the cantilever beam. Once again, the cantilever plate is independent from the y-direction, hence only the progression at $x = 0$ is plotted.

Two things are immediately noticeable. The first is that both displacements are stretched far beyond their equilibrium solutions. Especially the cantilever plate. After only 0.1 second, it has reached $25m$ in its displacement. This shows us that the elasticity of the wood is not properly modelled. This can only be explained by a mistake in the stiffness matrices or by the integration method not being stable. The second thing to notice is that the the curves are different. The displacement of the beam starts to increase a lot, even near $x = 0$, while the displacement of the plate seems to hold in place and become steeper near the free end. This may either be a

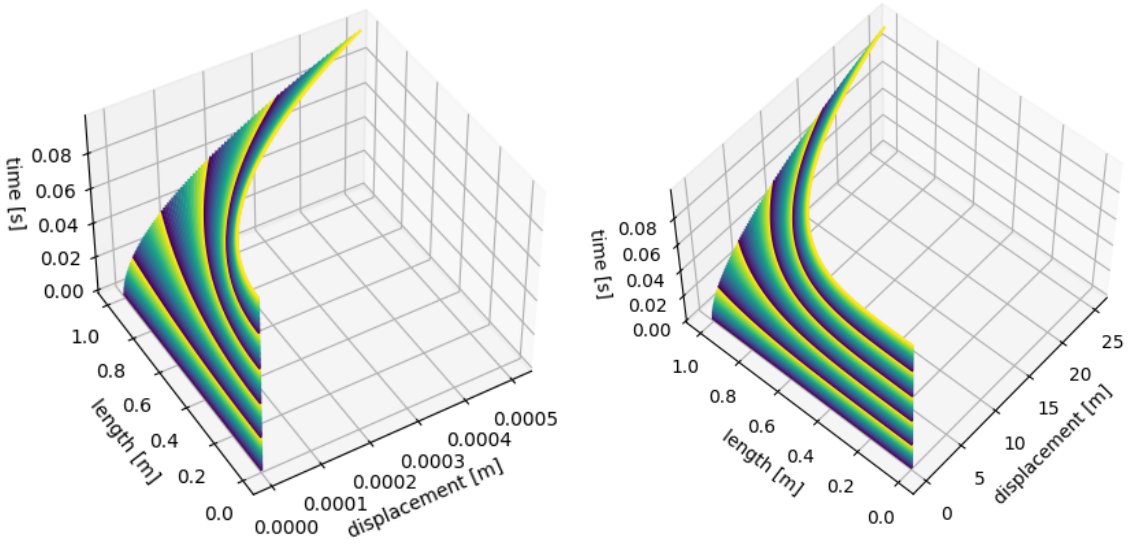

Figure 46: Numerically found displacement progressed in time of a cantilever beam (left) and cantilever plate (right). The cantilever plate yields results independent from the y-axis hence only the line at $x = 0$ is plotted. The dampening constants are given by $\zeta = \frac{EK^2}{\rho}$ and $\xi = B_{xx}$.

result of the difference in step size or may show another mistake in either the implementation of the boundary conditions or the interior of the stiffness matrix itself. Additionally, to experiment, the dampening coefficients were increased to inhibit the diverging behaviour. However, this did not help as $\zeta, > 100\frac{EK^2}{\rho}$, and $\xi, > 100B_{xx}$, had little to no impact on the curvature and amplitude of the displacement.

Now, we take a look at the totally clamped plate in gravity. The results look promising in the beginning. However, it is clear that the behaviour in the beginning, as shown in Figure 47 is not the correct behaviour. Namely, there is an oscillatory pattern in the which is never damped and keeps 'building' a higher displacement with each iteration. This is the case even though the damping constant, ξ, is taken a hundred times larger than B_{xx}. Another important note is the fact that the wave keeps propagating after a second. This is way to long and the plate should have resolved into a standing wave orders of magnitude quicker. It follows that we are, once again, lead to believe that the elasticity of the wood is not properly represented in the implemented model.

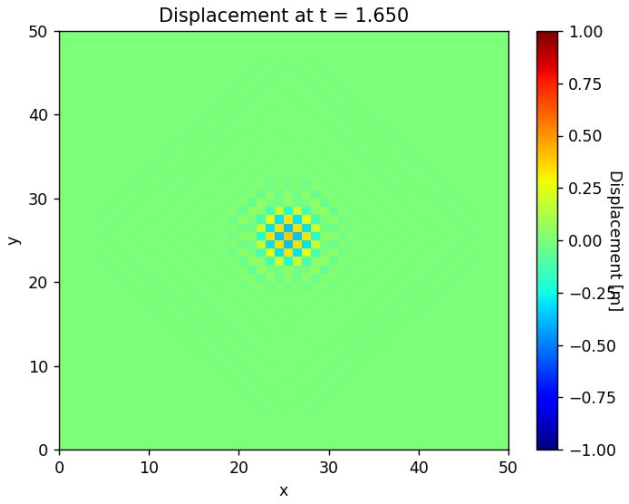

Figure 47: The time dependent results for a clamped plate experiencing gravity only at $t = 1.650s$.

A similar conclusion can be drawn from Figure 48. Namely, the wave propagation is much too slow and the displacement is much too large for a realistic model of a vibrating clamped plate. However, we must note

that the lengths of the displacement vector, while ignoring the oscillatory behaviour, does resemble that of the equilibrium solution.

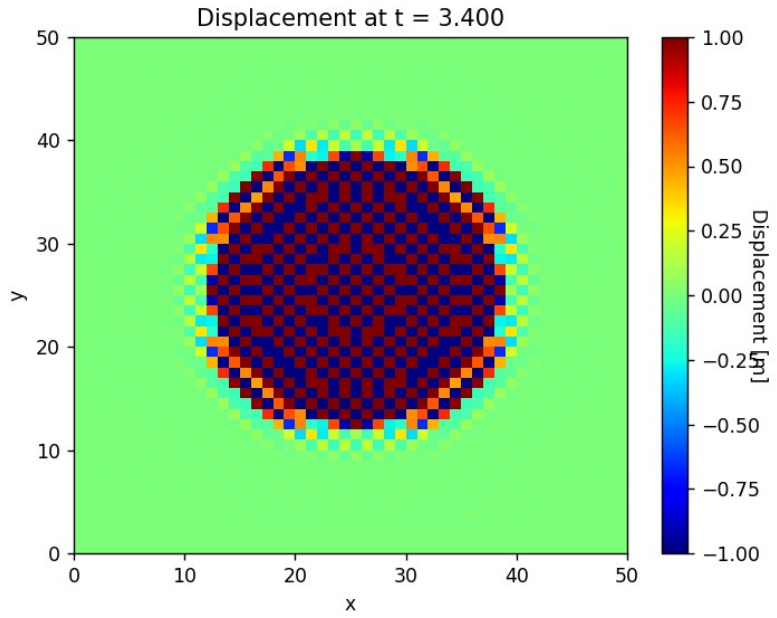

Figure 48: The time dependent results for a clamped plate experiencing gravity only at $t = 3.400s$.

The clamped plate with the sine driven source wave fairs no different. Though the Chladni patterns are visible in the numerical solution, this is not necessarily an effect of the bending wave equation. Namely, the wave propagates too slow and the displacement is too large to have any resemblance to the physical vibrations in a wooden plate. There is also still the possibility that the time integration method is unstable. However, this should not be the case as the stability criteria are met[61]. Though, we cannot rule this out without an in depth analysis on the forward Euler method in conjunction with the bending wave equation, which is outside of the scope of this thesis.

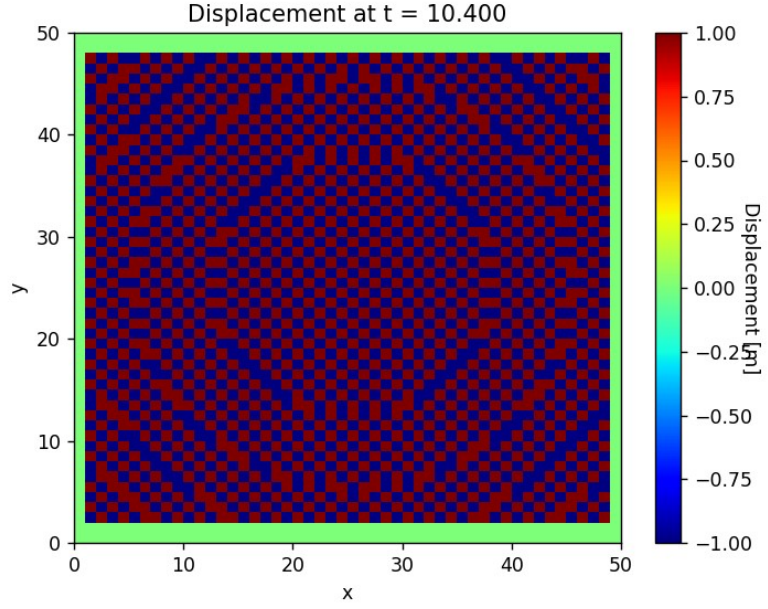

Figure 49: The time dependent results for a clamped plate with a source at $(x, y) = (L/2, H/2)$.

It is clearly visible in the simulation that nodal lines and anti-nodal lines do exist. However, they are the result of the oscillating behaviour previously shown. Similarly, the one dimensional clamped string with a source experiences standing waves with similar oscillatory behaviour, as shown in Figure 50.

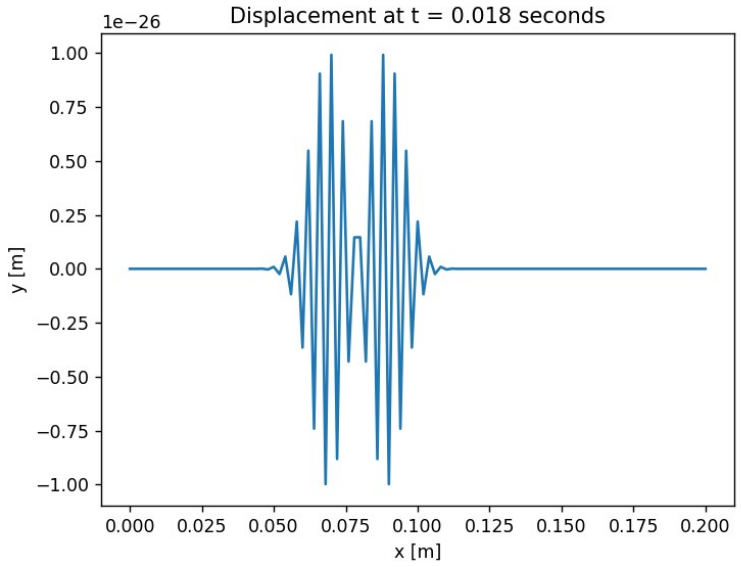

Figure 50: The time dependent results for a clamped beam with a source at $x = L/2$.

Figure 50 does show a standing mode. The oscillatory behaviour does not necessarily exclude this. However, we are led to believe that the displacement shown is not a standing mode since it does still propagate and its amplitude diverges after enough time steps.

Having seen the results of the time dependent numerical model, the time dependent part do not agree with the literature. Even though some patterns are visible, it is not clear if they are by chance or not. Only the time dependent cantilever beam and plate resemble their steady state counterparts. Unfortunately, due to the results of our own model not resembling the physics of vibrating plates, no correlation can be seen between the modes shown in the finite element models by [49] and our own finite element model.

The model can be improved using more accurate difference equations or using more grid spaces. However, this has shown to be very space and time inefficient. On top of this, the physical properties of a wooden plate differ immensely from the results in the displacements we have seen. Therefore, more research on the finite difference implementation of the bending wave equation, using the method of lines, must be done to improve the results. Only if the first iteration of the model yields results resembling the physical properties of vibrating wood, can we start another iteration of the model.

6 Conclusion and outlook

In conclusion, listeners can distinguish between Stradivari violins and non-Stradivari violins. In specific, the quality and colour can be distinguished from one another. Additionally, the semantics used to describe the timbre of a violin is coherent across listeners and can be used to describe the differences between Stradivarius and non-Stradivarius violins. The differences between violins can also be described mathematically. This can be done using the Dünnwald's timbre parameters, spectral flux and average sound pressure graphs. Investigations into spectral flux of violins shows a clear difference between historical violins, contemporary violins and violins of lower quality. The average sound pressure graphs of Stradivari violins and violins of the same period contain only slight differences, which might be picked up by attentive listeners.

The bridge is a key feature of the violin. The bridge functions as the main conductor of vibrations from the string to the corpus of the violin and vice versa. Therefore, since the corpus is the main radiator of the violin, the admittance of the bridge has a great impact on the radiated sound. This is supported by remarkable resemblance of the radiation and the admittance of the bridge shows when plotted against frequency.

The corpus and its function are described mainly in two ways. First, many forms of modal analysis are performed on the corpus. These range from theoretical Chladni patterns to experimental results using holographic interferometry. Second, numerical packages are often used to simulate the flexural wave equation. The different simulations largely have similar results and conform with the modal analyses.

The model we have constructed does agree with the numerical models found in literature in steady state. However, when using finite difference methods, a stable numerical time integration method is vital for proper results. Either the time integration method used in our numerical implementation was proven not to stable or the stiffness matrix fails to retain the physical properties of wood. As a consequence, the results do not conform with the numerical models found in literature nor resemble vibrations in a wooden plate. Therefore, further studies in numerical bending waves must repair the numerical integration schemes first and correct the first iteration of the model before adding more details.

References

[1] Michael Pyrkosz. *Reverse engineering the structural and acoustic behavior of a Stradivari violin.* PhD thesis, Michigan Technological University, 2013.

[2] Adam J Lonsdale and Adrian C North. Why do we listen to music? a uses and gratifications analysis. *British journal of psychology*, 102(1):108–134, 2011.

[3] Thomas Schäfer, Peter Sedlmeier, Christine Städtler, and David Huron. The psychological functions of music listening. *Frontiers in psychology*, 4:511, 2013.

[4] Steve Oakes. Evaluating empirical research into music in advertising: A congruity perspective. *Journal of Advertising Research*, 47(1):38–50, 2007.

[5] Michael Beverland, Elison Ai Ching Lim, Michael Morrison, and Milé Terziovski. In-store music and consumer–brand relationships: Relational transformation following experiences of (mis) fit. *Journal of Business Research*, 59(9):982–989, 2006.

[6] Naveen Kumar, Mohamad Arif Wajidi, Yong Tai Chian, S. Vishroothi, S. Swamy Ravindra, and P. Ashwini Aithal. The effect of listening to music on concentration and academic performance of the student: Cross-sectional study on medical undergraduate students. *Research Journal of Pharmaceutical, Biological and Chemical Sciences*, 7(6):1190–1195, 2016. ISSN 0975-8585.

[7] Patrick G Hunter and E Glenn Schellenberg. Music and emotion. In *Music perception*, pages 129–164. Springer, 2010.

[8] Carol A Smith and Larry W Morris. Differential effects of stimulative and sedative music on anxiety, concentration, and performance. *Psychological Reports*, 41(3_suppl):1047–1053, 1977.

[9] Linda Pring and Jane Walker. The effects of unvocalized music on short-term memory. *Current Psychology*, 13(2):165–171, 1994.

[10] Arian Musliu. The impact of music in memory. *European Journal of Social Science Education and Research*, 4(4):222–227, 2017.

[11] Pierre Salame and Alan Baddeley. Effects of background music on phonological short-term memory. *The Quarterly Journal of Experimental Psychology Section A*, 41(1):107–122, 1989.

[12] Andranick S Tanguiane. *Artificial perception and music recognition.* Springer, 1993.

[13] Marshall Long. *Architectural acoustics.* Elsevier, 2005.

[14] William Kuperman and Philippe Roux. Underwater acoustics. *Springer Handbook of Acoustics*, pages 149–204, 2007.

[15] Peter Tze-Ming Chou. Attention drainage effect: How background music effects concentration in taiwanese college students. *Journal of the Scholarship of Teaching and Learning*, 10(1):36–46, 2010.

[16] Claudia Fritz, AF Blackwell, I Cross, BCJ Moore, and J Woodhouse. Investigating english violin timbre descriptors. In *Proceedings of the 10th International Conference on Music Perception & Cognition (ICMPC 10)*, pages 638–641, 2008.

[17] Jan Stepanek. Evaluation of timbre of violin tones according to selected verbal attributes. In *32nd Int. Acoustical Conf., European Acoustics Association (EAA) Symp." Acoustics Banská Stiavnica*, pages 129–132, 2002.

[18] Anders Buen. On timbre parameters and sound levels of recorded old violins. *J. Violin Soc. Am.: VSA Papers*, 21(1):57–68, 2007.

[19] Francesco Setragno, Massimiliano Zanoni, Augusto Sarti, and Fabio Antonacci. Feature-based characterization of violin timbre. In *2017 25th European Signal Processing Conference (EUSIPCO)*, pages 1853–1857. IEEE, 2017.

[20] John Semmlow. *Signals and systems for bioengineers: a MATLAB-based introduction.* Academic Press, 2011.

[21] Carlo Andrea Rozzi, Alessandro Voltini, Fabio Antonacci, Massimo Nucci, and Massimo Grassi. A listening experiment comparing the timbre of two stradivari with other violins. *The Journal of the Acoustical Society of America*, 151(1):443–450, 2022.

[22] George Bissinger. The role of radiation damping in violin sound. *Acoustics Research Letters Online*, 5(82), 2004.

[23] Zdenek Otcenasek and Jan Stepanek. Violin sound radiation-directivity of violin timbre. *Fortschritte der Akustik*, 26:240–241, 2000.

[24] Ian Perry. *Sound radiation measurements on guitars and other stringed musical instruments*. PhD thesis, Cardiff University, 2014.

[25] Mirco Pezzoli, Antonio Canclini, Fabio Antonacci, and Augusto Sarti. A comparative analysis of the directional sound radiation of historical violins. *The Journal of the Acoustical Society of America*, 152(1): 354–367, 2022.

[26] Jim Woodhouse. The acoustics of the violin: a review. *Reports on progress in physics*, 77(11), 2014.

[27] Lothar Cremer. *The Physics of the violin*. The MIT Press, 1st edition, 1984. ISBN 978-0-262-03102-.

[28] Thomas D. Rossing Neville H. Fletcher. *The Physics of Musical Instruments*. Springer Science+Business Media, inc., 2nd edition, 2010. ISBN 978-1-4419-3120-7.

[29] Colin E Gough. Science and the stradivarius. *Physics World*, 13(4):27, 2000.

[30] Yonggyun Yu, In Gwun Jang, and Byung Man Kwak. Topology optimization for a frequency response and its application to a violin bridge. *Structural and Multidisciplinary Optimization*, 48(3):627–636, 2013.

[31] Colin E Gough. The violin bridge-island input filter. *The Journal of the Acoustical Society of America*, 143(1), 2018.

[32] Albrecht Schneider. *Studies in Musical Acoustics and Psychoacoustics*, volume 4. Springer, 2016.

[33] Anders Askenfelt. Observations on the violin bow and the interaction with the string. *STL-QPSR*, 36(2-3): 107–118, 1995.

[34] Diana Santos Young. *A methodology for investigation of bowed string performance through measurement of violin bowing technique*. PhD thesis, Citeseer, 2007.

[35] Colin E Gough. The theory of string resonances on musical instruments. *Acta Acustica united with Acustica*, 49(2):124–141, 1981.

[36] Jim Woodhouse. Body vibration of the violin–what can a maker expect to control. *Catgut acoustical society journal*, 4(5):43–49, 2002.

[37] CS Manohar and AJ Keane. Statistics of energy flows in spring-coupled one-dimensional subsystems. *Philosophical Transactions of the Royal Society of London. Series A: Physical and Engineering Sciences*, 346(1681):525–542, 1994.

[38] Colin E Gough and George Stoppani. The acoustics and historic development of string instruments. selfpublished, 2018.

[39] JE Ashton. Anisotropic plate analysis-boundary conditions. *Journal of Composite Materials*, 4(2):162–171, 1970.

[40] Chien Ming Wang, GT Lim, JN Reddy, and KH Lee. Relationships between bending solutions of reissner and mindlin plate theories. *Engineering structures*, 23(7):838–849, 2001.

[41] Takumi Asakura, Takashi Ishizuka, Tohru Miyajima, Masahiro Toyoda, and Shinichi Sakamoto. Finite-difference time-domain analysis of structure-borne sound using a plate model based on the kirchhoff-love plate theory. *Acoustical Science and Technology*, 35(3):127–138, 2014.

[42] Thomas D Rossing. Chladni's law for vibrating plates. *American Journal of Physics*, 50(3):271–274, 1982.

[43] Carleen Maley Hutchins. The acoustics of violin plates. *Scientific American*, 245(4):170–187, 1981.

[44] Colin E Gough. The violin: Chladni patterns, plates, shells and sounds. *The European Physical Journal Special Topics*, 145(1):77–101, 2007.

[45] Andrew N Norris. Flexural waves on narrow plates. *The Journal of the Acoustical Society of America*, 113 (5):2647–2658, 2003.

[46] Huu-Tai Thai and Dong-Ho Choi. A simple first-order shear deformation theory for the bending and free vibration analysis of functionally graded plates. *Composite Structures*, 101:332–340, 2013.

[47] Colin E Gough. Vibrational modes of the violin family. *Proc. SMAC2013*, pages 66–74, 2013.

[48] Colin E Gough. A violin shell model: Vibrational modes and acoustics. *The Journal of the Acoustical Society of America*, 137(3):1210–1225, 2015a.

[49] Colin E Gough. Violin plate modes. *The Journal of the Acoustical Society of America*, 137(1):139–153, 2015b.

[50] Comsol Multiphysics. Structural mechanics module, 2008.

[51] Chaitanya J Lomte. Vibration analysis of anisotropic plates, special case: Violin, 2013.

[52] Jose Bretos, C Santamarıa, and J Alonso Moral. Vibrational patterns and frequency responses of the free plates and box of a violin obtained by finite element analysis. *The Journal of the Acoustical Society of America*, 105(3):1942–1950, 1999.

[53] Erik Jansson, Nils-Erik Molin, and Harry Sundin. Resonances of a violin body studied by hologram interferometry and acoustical methods. *Physica Scripta*, 2(6):243, 1970.

[54] Jon C Luke. Measurement and analysis of body vibrations of a violin. *The Journal of the Acoustical Society of America*, 49(4B):1264–1274, 1971.

[55] M Chiba and T Sugimoto. Vibration characteristics of a cantilever plate with attached spring–mass system. *Journal of Sound and Vibration*, 260(2):237–263, 2003.

[56] M Fischer, J Jovanović, and F Durst. Reynolds number effects in the near-wall region of turbulent channel flows. *Physics of Fluids*, 13(6):1755–1767, 2001.

[57] HEA Van den Akker and RF Mudde. *Fysische transportverschijnselen I*. Delft University Press, 1998.

[58] PW Bearman. An investigation of the forces on flat plates normal to a turbulent flow. *Journal of Fluid Mechanics*, 46(1):177–198, 1971.

[59] Ya-Juan Bemmen Daniel A. Russel, Joseph P. Titlow. Acoustic monopoles, dipoles, and quadrupoles: An experiment revisited. *American Journal of Physics*, 67(660), 1999.

[60] Lars Hörchens. *Imaging of material inhomogeneities with flexural waves*. PhD thesis, Delft University of Technology, 2010.

[61] van Gijzen C. Vuik, Vermolen and M.J. Vuik. *Numerical methods for ordinary differential equations*. VSSD, 2018.

[62] Sega andKraaijevanger van Kan, Vermolen. *Numerical methods for partial differential equations*. VSSD, 2019.

[63] Vermolen van Kan, Segal. *Numerical methods in scientific computing*. VSSD, 2005.

[64] AI Jansen. *BINAS: informatieboek VWO-HAVO voor het onderwijs in de natuurwetenschappen [para]*. Wolters-Noordhoff, 1982.

[65] V Gryc and P Horáček. Variability in density of spruce (picea abies [l.] karst.) wood with the presence of reaction wood. *Journal of forest science*, 53(3):129–137, 2007.

[66] Charles R. Harris, K. Jarrod Millman, Stéfan J. van der Walt, Ralf Gommers, Pauli Virtanen, David Cournapeau, Eric Wieser, Julian Taylor, Sebastian Berg, Nathaniel J. Smith, Robert Kern, Matti Picus, Stephan Hoyer, Marten H. van Kerkwijk, Matthew Brett, Allan Haldane, Jaime Fernández del Río, Mark Wiebe, Pearu Peterson, Pierre Gérard-Marchant, Kevin Sheppard, Tyler Reddy, Warren Weckesser, Hameer Abbasi, Christoph Gohlke, and Travis E. Oliphant. Array programming with NumPy. *Nature*, 585(7825):357–362, September 2020. 10.1038/s41586-020-2649-2. URL https://doi.org/10.1038/s41586-020-2649-2.

[67] Edward Anderson, Zhaojun Bai, Christian Bischof, L Susan Blackford, James Demmel, Jack Dongarra, Jeremy Du Croz, Anne Greenbaum, Sven Hammarling, Alan McKenney, et al. *LAPACK users' guide*. SIAM, 1999.

[68] PA Smith and JR Wood. Poisson's ratio as a damage parameter in the static tensile loading of simple crossply laminates. *Composites Science and Technology*, 38(1):85–93, 1990.

[69] Ruel Churchill and James Brown. *Ebook: Complex Variables and Applications*. McGraw Hill, 2014.

[70] Neal L Carothers. *Real analysis*. Cambridge University Press, 2000.

[71] Olek C Zienkiewicz, Robert Leroy Taylor, and Jian Z Zhu. *The finite element method: its basis and fundamentals*. Elsevier, 7 edition, 2013.

[72] Ali R Hadjesfandiari, Arezoo Hajesfandiari, and Gary F Dargush. Pure plate bending in couple stress theories. *arXiv preprint arXiv:1606.02954*, 2016.

[73] Junuthula Narasimha Reddy. *An introduction to continuum mechanics*. Cambridge university press, 2013.

[74] Alan D McNaught, Andrew Wilkinson, et al. *Compendium of chemical terminology*, volume 1669. Blackwell Science Oxford, 1997.

[75] Goodrich Michael T, Tamassia Roberto, Goldwasser Michael H, et al. Data structures and algorithms in python, 2022.

Appendix

A Components of the violin

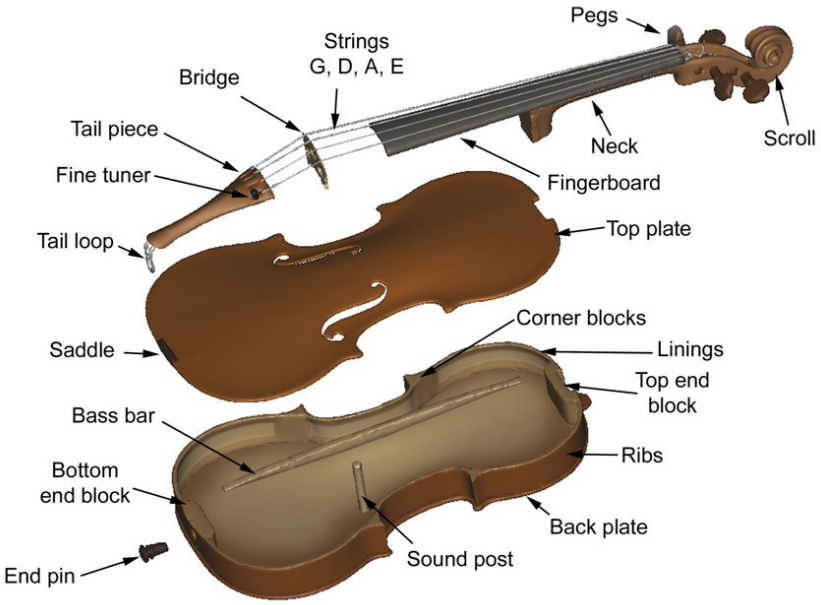

Figure 51: Schematic of the parts of a violin [1]

B A list of notable assumptions for simplification of the system

Ansatz B.1 (Assumptions for the subsystems and their relations)

B.1.1 Each subsystem is directly coupled to its neighbours only.

B.1.2 Each subsystem can be classified by its material components and the resulting behaviour of vibrations.

B.1.3 Each subsystem where the input is a superposition sines yields a superposition of sines in the output.

Ansatz B.2 (Assumptions for the string and the conductance of waves)

B.2.1 Every form of initialising a vibration in the string results in a superposition of sines in the string.

B.2.2 Vibrations initialised in the string do not dampen over time.

B.2.3 The dynamics of the string can be directly translated to the dynamics of the bridge.

B.2.4 The vibrations conducted to the string as the effect of coupling are of similar amplitude to the initial wave on the string.

Ansatz B.3 (Assumptions for the environment, bridge and corpus)

B.3.1 Vibrations conducted through the bridge to the corpus dominate with respect to the vibrations conducted through the fingerboard, neck or the pegs.

B.3.2 The coupling between the air and the material components of the violin is very weak.

B.3.3 The mechanical impedance of the bridge is symmetrical.

B.3.4 The bridge and corpus do not alter the frequency band of the signal.

B.3.5 Only the corpus radiates sound significantly.

Ansatz B.4 (Assumptions for the radiated sound)

B.4.1 The sound radiation is given by monopole, dipole and quadrapole sources.

B.4.2 The far field radiation is assumed to be a spherically symmetric plane wave with directional variation in the amplitude only.

C Defining a surface and deriving properties of the boundary conditions

This section contains four related topics, in order:

1. A definition of a surface
2. A validation that every point on the surface of a boundary is part of a simple closed curve
3. A description of the closed contour[69]
4. Generalised boundary conditions.

We determine the unit normal vector for on the boundary of a surface in $\mathbb{R}^2$ and the corresponding boundary conditions. We do this by showing that the boundaries of a closed and bounded set, which forms a pathwise connected metric space with the norm as its metric, can be described by a union of the ranges of simple closed contour in $\mathbb{R}^2$. From the contours, we can directly determine the unit normal vector using a vector field which is always tangent to the curve. We then use directional derivatives to impose conditions on the boundary.

C.1 Definitions

To define a surface, we will first need to look two other concepts: multiply pathwise connected and interior pathwise connected, both being stronger forms of pathwise connectedness, pathwise connected meaning that, between every two points $\vec{p_1}, \vec{p_2}$ in a metric space Ω, there exists a continuous curve $C : [0,1] \to \Omega$ such that $C(0) = \vec{p_1}$ and $C(1) = \vec{P_2}$[70].

A metric space being multiply pathwise connected makes sure that there exist at least two paths between every two points.

Definition C.1 (Multiply pathwise connected)
Let A be a metric space. We say A is multiply pathwise connected if at least two continuous curves $C_1, C_2 : [0,1] \to A$ such that $C_1(0) = C_2(0) = \vec{p_1}$, $C_1(1) = C_2(1) = \vec{P_2}$ and $C_1((1,2)) \cap C_2((1,2)) = \varnothing$, exist.

Interior pathwise connected is even stronger, and makes sure that, between every two points in the interior of a metric space, there exists a sequence of paths that does not intersect with the boundary that uniformly converges to the shortest path.

Definition C.2 (Interior pathwise connected)
Let A be a metric space. Let $\vec{p_1}, \vec{p_2} \in int(A) = (A \backslash \partial A)$ arbitrary. Suppose $C_{p(1,2)}$ is the set of continuous curves between $\vec{p_1}$ and $\vec{p_2}$, $C_{p(1,2)} = \left\{C : [0,1] \to A \mid C(0) = \vec{p_1},\ C(1) = \vec{p_2}\right\}$. Define the shortest path from $\vec{p_1}$ to $\vec{p_2}$: $C_{min} = \min\limits_{C \in C_{p(1,2)}} \left(\int_C \sqrt{x'(t)^2 + y'(t)^2} dt \right)$. Then define the set of "interior" paths from $\vec{p_1}$ to $\vec{p_2}$ in $int(A)$, $C_{p(1,2),int} = \{C \in C_{p(1,2)} \mid C \cap \partial A = \varnothing\}$.

We say A is interior pathwise connected if a sequence of functions $(C_n)_{C \in C_{p(1,2),int}}$ converges uniformly[70] to C_{min}. That is, for every $\epsilon > 0$, there exists an $N > 1$ such that $\sup_{t \in [0,1]} \left(d(C_n(t), C_{min}(t)) \right) < \epsilon$ for $n \geq N$.

We can now define a surface. The definition is based on the idea of a infinitely thin plate with as much realism as possible. However, we do assume the plate to be infinitely thin in order for our definition to match up with the thin plate theories we consider. The definition of a surface can be extended to three dimensions, however, it would cause some of the properties we derive to be extended to two dimensions.

Definition C.3 (Surface)
We call a set Ω in $\mathbb{R}^2$ a surface if it is closed, bounded, non-empty, has a non-empty open subset which is dense[70] in Ω and is interior pathwise connected.

In addition to a surface, we will also define encircling and interlocking sequences:

Definition C.4 (Encircling)

Let a set A be convex (meaning straight line between two points in A is fully contained by A). A is said to be encircled by set B if $\partial A \subset \partial B$.

For a non-convex set A and a pathwise connected set B, A is encircled by B if for every $a \in A$, there exist $b1, b2 \in B$ and $\delta, \epsilon > 0$ such that $B_\epsilon(b1) \cap B_\delta(b2) = \varnothing$, $B_\epsilon(b1) \cap A \neq \varnothing$, $B_\delta(b2) \cap A \neq \varnothing$ and $a \in C_{b1,b2}$ where $C : [0,1] \to (D)$ is a straight line from $b1$ to $b2$, and D is the convex cover of A and B.

Definition C.5 (Interlocking sequences)

A pair of sequences $((x_n)_{n\in\mathbb{N}}, (y_n)_{n\in\mathbb{N}})$ is interlocking on a metric (A, d) if for any $i, j \in \mathbb{N}$, $x_i \in C_{min}[0,1)$, where $C_{min} : [0,1] \to A$, is the shortest curve such that $C_0 = y_j$ and $C_1 = y_{j+1}$.

A pair of non-interlocking sequences is a pair of sequences which are not interlocked. Note that this definition does allow for two non interlocking sequences to converge to the same point.

C.2 The boundary; a union of simple closed contours

In this part, we will prove that a surface has a boundary which is composed of disjoint simple closed contours.

Theorem C.6 (Boundary of simple closed curves)

Let A be a surface and $h \in \mathbb{N}$, then $\partial A = \bigcup_{i=1}^{h} \{C_i \text{: } C_i \text{ is simple closed}\}$ such that $C_i \cap C_j = \varnothing$ for $i \neq j$.

Proof: Let $\Omega \subset \mathbb{R}^2$ be a closed set in the (x, y)-plane such that $\Omega \subset [-a, a] \times [-a, a]$ for some arbitrary $a < \infty \in \mathbb{R}$. Define $d(\vec{a}, \vec{b}) = \|\vec{a} - \vec{b}\|$ to be the distance between $\vec{a}, \vec{b} \in \Omega$. Then we have a metric space $(\Omega, \| \ \|)$, or Ω in shorter notation. Let the metric space Ω be multiply pathwise connected. Pathwise connected meaning that, between every two points $\vec{p_1}, \vec{p_2} \in \Omega$, there exists a continuous curve $C : [0,1] \to \Omega$ such that $C(0) = \vec{p_1}$ and $C(1) = \vec{P_2}$[70]. We say a set is multiply pathwise connected if at least two continuous curves $C_1, C_2 : [0,1] \to \Omega$ such that $C_1(0) = C_2(0) = \vec{p_1}$, $C_1(1) = C_2(1) = \vec{P_2}$ and $C_1((1,2)) \cap C_2((1,2)) = \varnothing$, exist. Hence, Ω cannot be empty, cannot contain isolated points and cannot contain lines which are not part of a simple closed contour. In addition, Ω cannot be split into two non empty disjointed sets which do not share a boundary.

Since Ω is closed and bounded, Ω^c can be written as the union of $h \in \mathbb{N}$ disjoint open sets: $\Omega^c = \Omega_0^c \cup \big(\bigcup_{i=1}^{h-1}(\Omega_i^c)\big)$, such that Ω_0^c encloses Ω and Ω encloses every Ω_i^c for $i \in \{1, 2, ..., h-2, h-1\}$. Thus $\partial\Omega$ can also be written as the union of disjoint closed sets: $\partial\Omega = \partial\Omega_0 \cup \big(\bigcup_{i=1}^{h-1}(\partial\Omega_i)\big)$, where $\partial\Omega_0$ is enclosed by Ω_0^c and $\partial\Omega_i$ enclose Ω_i^c respectively. Hence, each of the aforementioned disjoint closed subsets of $\partial\Omega$ can be described as a continuous curve $C_{\partial\Omega,i} : [0,1] \to \mathbb{R}^2$ such that $C_{\partial\Omega,i}(0) = C_{\partial\Omega,i}(1)$ for $i \in (\mathbb{N} \cup \{0\})$, which is a closed contour.

Furthermore, Ω must have non-empty open subset O_Ω which is dense in Ω. The closure of O_Ω is $cl(O_\Omega) = \bigcap\{G : G \text{ is closed and } O_\Omega \subset G\}$. O_Ω being dense in Ω means that $cl(O_\Omega) = O_\Omega$. It follows that Ω cannot be the empty set, cannot contain isolated points and cannot contain any lines or line segments.

Therefore, we let Ω be interior pathwise connected, directly implying that for every $x \in \Omega$, $card(\partial(\partial\Omega\backslash\{x\})) = 2$. That is, the cardinal number (the number that denotes the amount of elements in a set[70]) of the boundary of the boundary of Ω without $\{x\}$ is exactly equal to two. This is the case for three reasons:

1. Ω cannot contain any isolated points, lines or line segments.
2. if $x \in (C_{min} \cap \partial\Omega)$ then $card(\partial(\partial\Omega\backslash\{x\})) \geq 2$ since the boundary consists of at least one closed contour.
3. If for any $\vec{p_1}, \vec{p_2} \in \Omega$, there exists $x \in (C_{min} \cap \partial\Omega)$ with $card(\partial(\partial\Omega\backslash\{x\})) > 2$, there exist $\vec{p_3}, \vec{p_4} \in \Omega$ and $\epsilon > 0$ such that for every $C_{int} \in C_{p(3,4),int}$, $\sup_{t\in[0,1]}\big(\|C_{min} - C_{int}\|\big) > \epsilon$ since $(B_{\epsilon,open}(x) \cap int(\Omega))$ contains a disconnection[70], (A, B). As a direct result of the disconnection, we cannot create a continuous curve $C : [0,1] \to (A \cup B)$ with $C(0) = a \in A$ and $C(1) = b \in B$. Therefore, there exist two points such that every curve between the two points, that does not intersect the boundary, has to go around a ball with a radius of at least $\epsilon > 0$.

   (A disconnection (A,B) of a set G is a pair of disjoint non-trivial open sets such that $A \cup B = G$.)

   (to be exact, $card(\partial(\partial\Omega\backslash\{x\})) = 2 + 2l$ for $l \in \mathbb{N}$, $\partial\Omega$ being the union of continuous closed contours)

Moreover, $\partial\Omega$ cannot cross itself since, if $x \in \partial\Omega$, at a crossing of the boundary, is defined by a set S_x of pairwise non-interlocking sequences which converge to x with $card(S) > 2$. As a direct result, $card(\partial(\partial\Omega \backslash \{x\})) > 2$ for $x \in \Omega$ at a crossing of the boundary. Therefore, $x \in \partial\Omega$ at a crossing of the boundary means that Ω cannot be interior pathwise connected. Hence, by the contrapositive, since Ω is interior pathwise connected, the boundary may not cross itself. For every $x \in \partial\Omega$, $card(S_x) \leq 2$ since $\partial\Omega$ is the union of closed contours. Hence $card(S_x) = 2$. We will now refer to Ω as a surface.

Combining the fact that Ω is a closed, bounded, interior pathwise connected and contains a non-empty open set O_Ω which is dense in Ω, we can derive the following properties for Ω and $\partial\Omega$:

If Ω encircles a subset $H \subset \Omega^c$, then it encircles an open set O_{Ω^c} such that $H \subset O_{\Omega^c} \subset \Omega^c$ (Density of $O_\Omega \subset \Omega$). $\partial\Omega$ can be described by the union of the images of disjoint bijective continuous curves $C : [0,1] \to \partial\Omega$(closed, bounded and multiply connected (for bijectivity)). $\partial\Omega = \bigcup_{i \in (\mathbb{N} \cap [0, h-1])} \big(C_{\partial\Omega,i}([0,1])\big)$ where $C_{\partial\Omega,i}(t_1) = C_{\partial\Omega,i}(t_2)$ for $i \in (\mathbb{N} \cup \{0\})$ if and only if $t_1 = 0$ and $t_2 = 1$. Which is to say that $\partial\Omega$, is a union of the ranges of disjoint continuous simple closed contours (closed, bounded, density of $O_\Omega \subset \Omega$ and interior pathwise connected).

Note that the geometry of Ω is necessary to determine $\partial\Omega$. When the geometry of Ω is not analytically available, but is graphically available, we are able to determine the curves describing $\partial\Omega$ with Fourier series.

C.3 Closed contours and boundary conditions

Let $i \in (\{0, 1, 2, ..., h-2, h\})$, then suppose $C_{\partial\Omega,i} : [0,1] \to \mathbb{R}^2$ with a tangent unit vector $\vec{\tau}$. Let $\vec{r}(t) = (x(t), y(t))$ for $t \in [0,1]$ be a parametrization of $C_{\partial\Omega,i}$. It follows that the normal unit vector $\vec{n}$ at $\partial\Omega$ is defined by $\langle \vec{n}(t), \vec{\tau}(t) \rangle = 0$. Thus $\vec{n}(t) = \pm\big(\frac{-y'(t)}{\|r'(t)\|}, \frac{x'(t)}{\|r'(t)\|}\big)$, depending on the orientation of the $C_{\partial\Omega,i}$. As a convention, we take a parametrization of the form

$$\vec{r}(t) = \big(\sum_{j \in \mathbb{N}} A_{x,j} \cos(\tilde{\omega}_{x,j} t + \phi_{x,j}), \sum_{j \in \mathbb{N}} A_{y,j} \sin(\tilde{\omega}_{y,j} t + \phi_{y,j})\big), \tag{C.1}$$

rotating counter clockwise for $A_{x,j}, A_{y,j}, \tilde{\omega}_{x,j}, \tilde{\omega}_{y,j} \geq 0$ and $\phi_{x,j}, \phi_{y,j} \in [0, 2\pi]$, or any other analytical counter clockwise rotation, which agrees with the orientation, for $C_{\partial\Omega,0}$. Similarly, we take clockwise rotations for $C_{\partial\Omega,i}$ with $i \in (\mathbb{N} \cap [1, h-1])$.

In conclusion, $\vec{n}(t) \perp \vec{\tau(t)}$ and points away from Ω with $\vec{n}(t) = \big(\frac{y'(t)}{\|r'(t)\|}, \frac{-x'(t)}{\|r'(t)\|}\big)$ for $C_{\partial\Omega,0}$ and $\vec{n}(t) = \big(\frac{-y'(t)}{\|r'(t)\|}, \frac{x'(t)}{\|r'(t)\|}\big)$ for $C_{\partial\Omega,i}$ where $i \in (\mathbb{N} \cap [1, h-1])$.

As mentioned earlier, in Equations of motions (2.4.1), each part of the boundary needs to have two boundary conditions. Let $U : \Omega \to \mathbb{R}$ be the solution to Equation 2.5, then let the $\partial\Omega$ be described by the ranges of $h \in \mathbb{N}$ simple closed contours. Let $i \in \{0, 1, 2, ..., h-2, h-1\}$. It follows that every $t_{\partial\Omega,i} \in \partial\Omega_i$ needs two conditions, using directional derivatives (at the points where the directional derivatives exist), of the following form:

$$\sum_{j \in \mathbb{N}} \alpha_{j,t_{\partial\Omega,i}} D^{(j)}_{\vec{n}} U(t_{\partial\Omega,i}, t) = f_{t_{\partial\Omega,i}}(t, x_{t_{\partial\Omega}}, y_{t_{\partial\Omega}}), \tag{C.2}$$

where $\alpha_{j,t_{\partial\Omega,i}} \in \mathbb{R}$, for $j \in \mathbb{N}$, $D^{(j)}_{\vec{n}} U(t_{\partial\Omega})$ is the j_{th} directional derivative of U with respect to $\vec{n}$, at $t_{\partial\Omega} \in \partial\Omega$, and $f_{t_{\partial\Omega,i}}$ is sufficiently smooth. Also note that z is the solution to Equation 2.5, and must therefore be sufficiently smooth such that the j_{th} directional derivative, with $\alpha_{j,t_{\partial\Omega,i}} \neq 0$, of U with respect to $\vec{n}$ is defined locally at $t_{\partial\Omega,i}$ for every $t_{\partial\Omega,i} \in \partial\Omega$. Note that, if the directional derivatives do not exist at some point $t_{\partial\Omega,i}$, there must be two directional derivatives which approach from both sides on $\partial\Omega_i$. In that case, $t_{\partial\Omega,i}$ needs two boundary conditions for each of the two directional derivatives.

D Derivation of the flexural wave equation

The derivation of the flexural wave equation is based on two fundamental assumptions[71]:

1. Plane sections remain plane during deformation.
2. Stresses in the normal direction of deformations in the plate, along the z-axis, are small.

Using these assumptions, we can use a schematic to derive forces and stress resultants. The first step is to find the stresses if cylindrical bending takes place in a single direction, whether it be in the x- or y- direction. Then, we extend the problem to include more general plate kinematics. This is done by using pure bending in conjunction with Cauchy bending theory for linear isotropic media.

D.1 Bending moment for cylindrical bending of a plate

Consider an isotropic plate being wrapped around a cylinder with some radius, $r \in \mathbb{R}$, big enough such that the deflection of the plate is small. We can then divide the plate into small segments along the curvature of the plate. In each segment, a number of stresses arise as a result from the bending.

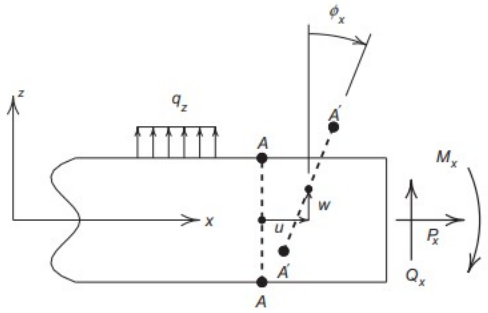

Figure 52: A schematic for the cylindrical bending of a plate[71]. M_x, P_x and Q_x are stress the resultants, A denotes the original position of the edges of the plate, A' denotes the same position after bending, ϕ is the angle of rotation, q_z is the transverse load, u is the deformation and w is the mid-plane displacement.

Figure 52 shows the (x, z)-slice of a plate segment with the directions of stress resultants. Firstly, M_x, Q_x and P_x are the bending moment, transverse shear force and axial force respectively. Secondly, q_z is a lateral load, or a force exerted on the plate normal to the (x, y)-plane. ϕ_x is the rotation with respect to the (x, y)-plane. Lastly, the deformation U is indicated as u with z-component $U_z = w$. Often w is referred to as the mid-plane displacement. Note that the subscript does not a derivative with respect to z.

To derive the displacement, consider some square cell with height Δz and width Δx. When bending takes place, we assume that the square is deformed to a symmetric trapezium, or a isosceles trapezium. The diagonals of the trapezium make a (locally constant) angle of $\frac{\phi_{xz}}{2}$ with the z-axis. Note that we assume the angle to increase linearly with the distance from the centre of the square. If we were to draw lines along the angle of rotation, we obtain a fan wave. Additionally, if $z = 0$ in the middle of the square, then the diagonals of the trapezium intersect the square at $z = 0$ exactly. If $z \neq 0$, then the trapezium is stretched, or compressed, in the x-direction. If the middle of the square is located at $z = 0$, the maximum extra distance on both sides of the trapezium is δx_z. The extra distance due to the stretching is δx_x at both sides of the trapezium.

Now suppose we have two squares directly adjacent to one another with the centres at $z = 0$. The point of rotation is denoted by $P_r(x_r, z_r)$. When bending occurs, let $P_0(x_0, z_0)$ be located at the centre of the left box. Then suppose there is some point $P_1(x_1, z_1)$ exists somewhere in the two boxes such that $x_1 > x_0$. A schematic of this scenario, such that P_1 is in the centre of the right box specifically, is given by Figure 53. In this schematic, the stretching in the x-direction is also shown with the direction of being indicated with the bending moment M.

Due to the fan wave assumption, x_1 and x_r change, even if $x_1 \leq x_0 + \frac{\Delta x}{2}$. Therefore, we denote the original position of P_1 and P_r as $P_{r,eq}(x_{r,eq}, z_{r,eq})$. Hence, if $x_1 \leq x_0 + \frac{\Delta x}{2}$, we have

$$x_1 = (x_{1,eq} - x_0) + \delta x_z = (x_{1,eq} - x_0) + z \tan\left(\frac{(x_{1,eq} - x_0)}{\Delta x/2} \frac{\phi_{xz}}{2}\right) \tag{D.1}$$

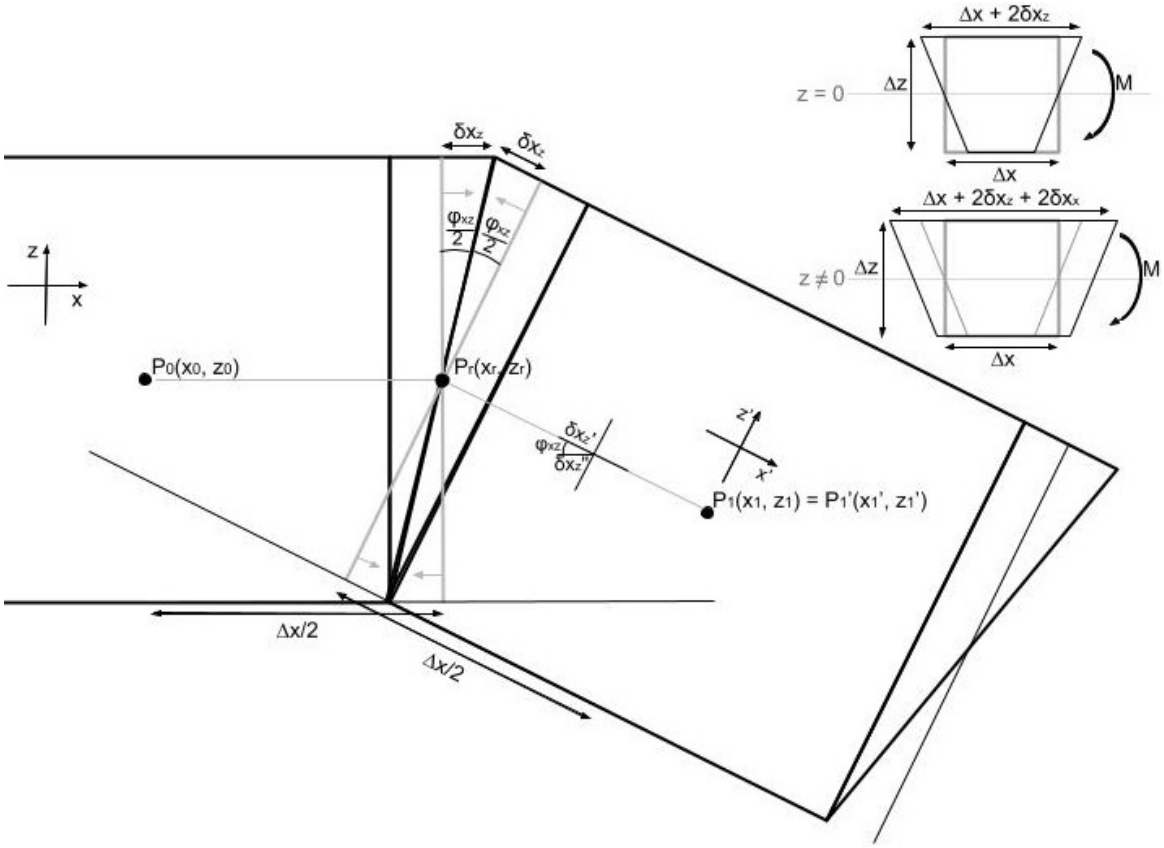

Figure 53: A schematic of the (x, z)-plane of a bending plate. Each box represents a small segment of the plate, bent with an angle ϕ_{xz} causing a displacement δx_z at the edge of each segment. The bending moment is indicated with M. After bending, the new coordinates are denoted with (x', y', z'). If the segment is located far from $z = 0$, the segment is also stretched in the x-direction with δx_x.

If $x_1 > x_0 + \frac{\Delta x}{2}$, we perform a rotational transformation using $\delta x_z'' = \delta x' \cos(\phi)$ and we can express $\delta x_z'$ with

$$\delta x_z' = \left(x_{1,eq} - x_{r,eq}\right) + z \tan\left(\frac{x_{1,eq} - x_{r,eq}}{\Delta x/2} \frac{\phi_{xz}}{2}\right) \tag{D.2}$$

for $x_{1,eq} - x_{r,eq} \in [0, \Delta x/2]$ and

$$\delta x_z' = \left(x_{1,eq} - x_{r,eq}\right) + z \tan\left(\frac{\phi_{xz}}{2}\right) + z\left(\frac{x_{1,eq} - (x_{r,eq} + \Delta x/2)}{\Delta x/2} \frac{\phi_{xz}}{2}\right) \tag{D.3}$$

for $x_{1,eq} - x_{r,eq} \in [\Delta x/2, \Delta x]$. Thus, if we place P_1 such that $x_{1,eq} = x_{r,eq} + \Delta x/2$, we get

$$\delta x_z' = \Delta x/2 + z \tan\left(\frac{\phi_{xz}}{2}\right). \tag{D.4}$$

We can now calculate x_1. taking ϕ_{xz} small, we get

$$\begin{aligned} x_1 - x_0 &= +\Delta x/2 + z \tan\left(\frac{\phi_{xz}}{2}\right) + \cos(\phi_{xz})\left[\Delta x/2 + z \tan\left(\frac{\phi_{xz}}{2}\right)\right] \\ &\approx \Delta x + z\phi_{xz}. \end{aligned} \tag{D.5}$$

The derivation of the flexural wave equation for cylindrical bending of a plate, after Zienkiewicz et al., is analogous to the derivation of a bending bar[60]. We have not yet made the assumption that the plate is thin, thus we must redefine U temporarily. U becomes $U : \Omega \times [-h/2, h/2] \times \mathbb{R} \to \mathbb{R}$. Hence, using $U(x_0, y, z_0, t)$ as a reference point to calculate the displacement in the x-direction $U_x(x, y, z, t)$. We get

$$\begin{aligned} U_x(x, y, z, t) &= (x - x_0) - (x_{eq} - x_0) + U_x(x_0, y, z_0, t) \\ &\approx (z - z_0)\phi_{xz} + U_x(x_0, y, z_0, t). \end{aligned} \tag{D.6}$$

Notice that z_0 is assumed to be 0, so the reference point is on the x-axis. Additionally phi_{xz} is only constant locally and is generally given by a function $\phi_{xz}(x, y, z, t)$. This means that the approximation of U will have a larger error the larger $z - z_0$ becomes and that there is no strain due to stretching in the x-axis.

Let $\vec{r} \in \Omega \times [-h/2, h/2]$ and $\vec{r}_\Omega \in \Omega$. It follows that $U_x(\vec{r}, t) = U_x(x_0, y, 0, t) - z\phi_{xz}(\vec{r}_\Omega, 0, t)$. ϕ_{xz} is assumed constant normal to the mid-plane section, which is taken to be the z- direction for cylindrical bending.

By definition, the strain in the x-direction is given by

$$\epsilon_x = \frac{\partial U_x}{\partial x}(x_0, y, 0, t) + z\frac{\partial \phi_{xz}}{\partial x}(\vec{r}_\Omega, 0, t). \tag{D.7}$$

Similarly, the strain in the y-direction is given by

$$\epsilon_y = \frac{\partial U_y}{\partial y}(x, y_0, 0, t) + z\frac{\partial \phi_{yz}}{\partial y}(\vec{r}_\Omega, 0, t). \tag{D.8}$$

Then let $i, j \in \{x, y\}$ with $i \neq j$. The normal stresses in the i-direction are given by

$$\sigma_i = \frac{E}{1 - \nu^2}\epsilon_i, \tag{D.9}$$

where ν is Poisson's ratio and E is Young's elasticity modulus[71]. Calculating the bending momentum for a plate, with cross section $A = [-W/2, W/2] \times [\Delta z/2, \Delta z/2]$ in direction i, yields

$$M_i = \int_A \sigma_i \tilde{z} \mathrm{dA} = \int_{-\Delta y/2}^{\Delta y/2}\int_{-\Delta z/2}^{\Delta z/2} \sigma_i \tilde{z} \mathrm{d}\tilde{z}\mathrm{d}\tilde{j} = B\left(\frac{\partial \phi_i}{\partial i}\right), \tag{D.10}$$

where $B = \frac{Eh^3\Delta y}{12(1-\nu^2)}$ is the bending rigidity. For thin plates specifically, we can neglect shear deformation, therefore, we must have $\frac{\partial U}{\partial i} = \tan(\phi_i) \approx \phi_i$[71]. Thus, for the bending moments for a thin strip, in direction i on the plate with width W, we have

$$M_i = B\left(\frac{\partial^2 U}{\partial i^2}\right). \tag{D.11}$$

Then, we can derive the equilibrium solution for a small segment of the plate. The overview of forces is shown in Figure 54

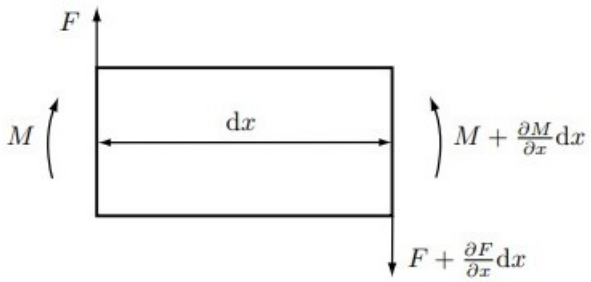

Figure 54: A schematic of the forces and the bending moment of a small plate segment with width dx, after Hörchens.

With the equilibrium equation given by

$$\vec{M} \cdot \hat{\mathbf{x}} - \left(\vec{M} \cdot \hat{\mathbf{x}} + \frac{\partial(\vec{M} \cdot \hat{\mathbf{x}})}{\partial x}\mathrm{d}x\right) - (\vec{F} \cdot \hat{\mathbf{x}})\mathrm{d}x = 0. \tag{D.12}$$

We integrate over a small segment. Since definite integrals equating to zero, we obtain a zero-valued integrand. Then, using $\vec{F} = h\rho\Delta x\Delta y\frac{\partial^2 U_z}{\partial x^2}$, we get

$$\frac{Eh^2}{12\rho(1-\nu^2)}\frac{\partial^4 U}{\partial x^4} + \frac{\partial^2 U}{\partial t^2} = 0 \tag{D.13}$$

Having obtained the bending moment for cylindrical bending, we want to generalise this bending behaviour. The first case to consider is a isotropic plate with pure bending. Pure bending makes sure that the cross strains are null. Therefore, we can use a principle of superposition to obtain the flexural wave equation for isotropic plates.

D.2 Bending moments for linear isotropic media

For more general forms of bending, the strain in the z-direction also has effect on the bending in x- and y-directions. The strain is given by

$$\epsilon_z = \frac{\nu}{1-\nu}\left(\frac{\partial \phi_x}{\partial x}(\vec{r},t) + \frac{\partial \phi_y}{\partial y}(\vec{r},t)\right), \tag{D.14}$$

where ν is Poisson's ratio. We use Cauchy elasticity theory[72], in which couple stresses are zero and the tensile stresses are symmetric. In terms of tensor components this becomes $\mu_{ij} = 0$ and $\sigma_{ij} = \sigma_{ji}$.

For linear isotropic media, meaning that the material is homogeneous and the elastic moduli are the same in every direction, the tensile stress can be given in terms of the Lamé constants[72]. Let G and λ be the shear modulus and the Lamé's first constant respectively. The tensile stress becomes

$$\sigma_{ij} = \lambda \epsilon_{zz}\delta_{ij} + 2G\epsilon_{ij}, \tag{D.15}$$

for $i, j \in \{x, y\}$ and δ_{ij} is the Kronecker Delta function for the components of the unit tensor. Additionally, the Lamé constants are related to Young's modulus of elasticity, E, and Poisson's ratio ν with

$$\lambda = \frac{\nu E}{(1+\nu)(1-2\nu)} \tag{D.16}$$

and

$$G = \frac{E}{2(1+\nu)}. \tag{D.17}$$

Using pure bending, meaning that cross strains $\epsilon_{ij} = 0$ for $i \neq j$, Hadjesfandiari et al. finds

$$\sigma_{xx} = \frac{E}{1-\nu^2}\left(\epsilon_{xx} + \nu\epsilon_{yy}\right)z, \tag{D.18}$$

$$\sigma_{yy} = \frac{E}{1-\nu^2}\left(\epsilon_{yy} + \nu\epsilon_{xx}\right)z \tag{D.19}$$

and

$$\sigma_{xy} = \sigma_{yx} = 0 \tag{D.20}$$

Thus, for the bending moments, in direction i on the thin plate with width W, we have

$$M_i = \int_{\mathrm{A}} \sigma_{ii}\tilde{z}\mathrm{dA} = \int_{-\Delta y/2}^{\Delta y/2}\int_{-\Delta z/2}^{\Delta z/2} \sigma_{ii}\tilde{z}\mathrm{d}\tilde{z}\mathrm{d}\tilde{j} = B\left(\frac{\partial \phi_i}{\partial i} + \nu\frac{\partial \phi_j}{\partial j}\right) = B\left(\frac{\partial^2 U}{\partial i^2} + \nu\frac{\partial^2 U}{\partial j^2}\right), \tag{D.21}$$

where $B' = \frac{Gh^3\Delta j}{6(1-\nu)} = \frac{Eh^3\Delta j}{12(1-\nu^2)}$ is the bending rigidity[72]. Then taking Equation D.13 in two dimensions and combining them yields the bi-harmonic equation with external force:

$$\frac{Eh^2}{12(1-\nu^2)}\nabla^4 U_z + \frac{\partial^2 U_z}{\partial t^2} = 0. \tag{D.22}$$

However, the bending of wood behaves differently depending on the direction and location of the force. Thus, the bending cannot totally be described by pure bending and the plate is not linear isotropic anymore. This is the case since the boundary conditions, though linear, are not independent of the deformation[73]. Hence, we must find another way to calculate the bending moment in other forms of bending, such as a saddle.

Though, if bending takes place in direction i only, we can use cylindrical bending without loss of generality. This can be seen by setting $\frac{\partial^2 U}{\partial j^2} = 0$ in Equation D.21.

D.3 Bending moments for thin orthotropic plates

For orthotropic materials, there exists a point such that the material properties are symmetric with respect to three orthogonal axes. This is not necessarily isotropic however is the closest we come to violin plates, approximating them as thin plates.

For a solid body, we assume that all deformations are small. Then, we can define a new strain tensor: the Green-Lagrange strain tensor (or Greens strain tensor)[73]. It is given by

$$\vec{\mathbf{E}} = \frac{1}{2}\left[\nabla_m \vec{U} + (\nabla_m \vec{U})^{\mathrm{T}} + (\nabla_m \vec{U}) \cdot (\nabla_m \vec{U})^{\mathrm{T}}\right]. \tag{D.23}$$

Notice that the notation ∇_m refers to the material coordinates. In this case, since only orthotropic plates are considered, we can choose the spatial Cartesian coordinate system in a such a way that it lines up with the material Cartesian coordinate system. Hence $\nabla_m \vec{U} = \nabla \vec{U}$. Note that this statement may not hold true for all orthotropic shells. Those with curvature in equilibrium position have mid plane sections which do not align with the z-axis. Therefore, $U_z \neq w$; as opposed to Figure 52.

Expanding Greens strain tensor gives normal strains ϵ_{ii} and shear strains E_{ij} for $i, j \in \{x, y, z\}$, $i \neq j$. We get

$$E_{ii} = \frac{\partial U_i}{\partial i} + \frac{1}{2}\left[\left(\frac{\partial U_x}{\partial x}\right)^2 + \left(\frac{\partial U_y}{\partial x}\right)^2 + \left(\frac{\partial U_z}{\partial x}\right)^2\right] \tag{D.24}$$

and

$$E_{ij} = \frac{1}{2}\left(\frac{\partial U_i}{\partial j} + \frac{\partial U_j}{\partial i} + \frac{\partial U_x}{\partial i}\frac{\partial U_x}{\partial j} + \frac{\partial U_y}{\partial i}\frac{\partial U_y}{\partial j} + \frac{\partial U_z}{\partial i}\frac{\partial U_z}{\partial j}\right). \tag{D.25}$$

To simplify this, we work with the infinitesimal strain tensor $\vec{\epsilon}$. Hence, neglecting the multiplied partial derivatives and using $\tan(\phi) \approx \phi$, we get

$$\epsilon_{ii} = \frac{\partial U_i}{\partial i} \tag{D.26}$$

and

$$\epsilon_{ij} = \frac{1}{2}\left(\frac{\partial U_i}{\partial j} + \frac{\partial U_j}{\partial i}\right). \tag{D.27}$$

This can be expressed in terms of the small angles, $\phi_{ij} : \Omega \times [-h/2, h/2] \times \mathbb{R} \to [-\pi, \pi]$, on an infinitesimal segment. Similar to the cylindrical bending, the directional deflection is dependent on the bending with respect to the z-axis. However, longitudinal stretching and bending in the x, y plane around the z-axis must also be accounted for in the bending for orthotropic plates. We describe the deformation function $U(\vec{r}, t)$ as a function which relates the deformation of $(\vec{r}, t)$ and $(\vec{r}_0, t_0)$ in three dimensions, obtaining

$$U_i(\vec{r}, t) \approx \vec{U}(\vec{r}_0, t) \cdot \hat{\mathbf{i}} + (x - x_0)\phi_{ix}(\vec{r}, t) + (y - y_0)\phi_{iy}(\vec{r}, t) + (z - z_0)\phi_{iz}(\vec{r}, t). \tag{D.28}$$

In this notation, ϕ_{ij} with $i \neq j$, is the angle of bending with the j-axis in the (i, j)-plane. In addition, ϕ_{ii} is defined to represent the fan wave stretching in the i-direction shown in Figure 53; $\frac{|x-x_0|}{\Delta x/2}\phi_{ii} \approx \tan\left(\frac{|x-x_0|}{\Delta x/2}\phi_{ii}\right) = \frac{\delta i/2}{\Delta i/2}$ for some deflection $\delta i \in \mathbb{R}$ in the i-direction. However, we must use the fact that the deflection is very small, $\delta i \ll i$. Otherwise, the domain of ϕ_{ii} is not a subset of $[-\pi, \pi]$.

For brevity, denote $\phi_{ij}(\vec{r}, t) = \phi_{ij}$. Notice that ϕ_{ij} and ϕ_{ji} describe the same bending however are oppositely defined. Hence $\phi_{ij} = -\phi_{ji}$. The components of the infinitesimal strain tensor become

$$\epsilon_{ii} \approx (x - x_0)\frac{\partial \phi_{ix}}{\partial i} + \phi_{ix} + (y - y_0)\frac{\partial \phi_{iy}}{\partial i} + (z - z_0)\frac{\partial \phi_{iz}}{\partial i} + \phi_{ii} \tag{D.29}$$

and

$$\epsilon_{ij} \approx \frac{1}{2}\left[(x - x_0)\left(\frac{\partial \phi_{ix}}{\partial j} + \frac{\partial \phi_{jx}}{\partial i}\right) + (y - y_0)\left(\frac{\partial \phi_{iy}}{\partial j} + \frac{\partial \phi_{jy}}{\partial i}\right) + (z - z_0)\left(\frac{\partial \phi_{iz}}{\partial j} + \frac{\partial \phi_{jz}}{\partial i}\right)\right] \tag{D.30}$$

Then, to obtain the stresses in the plate, an elasticity modulus is needed. For this, we use the fourth order elasticity tensor $\mathbf{C}$[73], not to be confused with the right Cauchy-Green deformation tensor. The stress and strain can bed related using

$$\vec{\sigma} = \mathbf{C}\vec{\epsilon} \qquad (\sigma_{ij} = C_{ijkl}\epsilon_{kl}), \tag{D.31}$$

where $i, j, k, l \in \{x, y, z\}$. The tensor components C_{ijkl} are the stiffness coefficients and are symmetric with respect to ij and kl, i.e. $C_{ijkl} = C_{klij}$. Even more, since Cauchy's theory of bending is used, the shear stresses are symmetric. Therefore, $\mathbf{C}$ is a 6×6 matrix, and not a 9×9 matrix. For orthotropic materials, we find

$$\begin{Bmatrix} \sigma_1 \\ \sigma_2 \\ \sigma_3 \\ \sigma_4 \\ \sigma_5 \\ \sigma_6 \end{Bmatrix} = \begin{bmatrix} C_{11} & C_{12} & C_{13} & 0 & 0 & 0 \\ C_{12} & C_{22} & C_{23} & 0 & 0 & 0 \\ C_{13} & C_{23} & C_{33} & 0 & 0 & 0 \\ 0 & 0 & 0 & C_{44} & 0 & 0 \\ 0 & 0 & 0 & 0 & C_{55} & 0 \\ 0 & 0 & 0 & 0 & 0 & C_{66} \end{bmatrix} \begin{Bmatrix} \epsilon_1 \\ \epsilon_2 \\ \epsilon_3 \\ \epsilon_4 \\ \epsilon_5 \\ \epsilon_6, \end{Bmatrix} \tag{D.32}$$

using the Voigt-Kelvin notation[73] (for example, $\sigma_{xx} \to \sigma_1, \sigma_{yy} \to \sigma_2, \sigma_{zz} \to \sigma_3, \sigma_{yz} \to \sigma_4, \sigma_{xz} \to \sigma_5, \sigma_{xy} \to \sigma_6$). Again, using the Lamé constants, relating stress and strain between different directions, we obtain

$$\begin{Bmatrix} \sigma_1 \\ \sigma_2 \\ \sigma_3 \\ \sigma_4 \\ \sigma_5 \\ \sigma_6 \end{Bmatrix} = \begin{bmatrix} \frac{E_x}{C_0}(1 - \nu_{yz}\nu_{zy}) & \frac{E_x}{C_0}(\nu_{yx} + \nu_{yz}\nu_{zx}) & \frac{E_x}{C_0}(\nu_{zx} + \nu_{yx}\nu_{yz}) & 0 & 0 & 0 \\ \frac{E_x}{C_0}(\nu_{yx} + \nu_{yz}\nu_{zx}) & \frac{E_y}{C_0}(1 - \nu_{xz}\nu_{zx}) & \frac{E_y}{C_0}(\nu_{yz} + \nu_{zx}\nu_{xy}) & 0 & 0 & 0 \\ \frac{E_x}{C_0}(\nu_{zx} + \nu_{yx}\nu_{yz}) & \frac{E_y}{C_0}(\nu_{yz} + \nu_{zx}\nu_{xy}) & \frac{E_z}{C_0}(1 - \nu_{xy}\nu_{yx}) & 0 & 0 & 0 \\ 0 & 0 & 0 & G_{yz} & 0 & 0 \\ 0 & 0 & 0 & 0 & G_{xz} & 0 \\ 0 & 0 & 0 & 0 & 0 & G_{xy} \end{bmatrix} \begin{Bmatrix} \epsilon_1 \\ \epsilon_2 \\ \epsilon_3 \\ \epsilon_4 \\ \epsilon_5 \\ \epsilon_6, \end{Bmatrix} \tag{D.33}$$

where $C_0 = 1 - \nu_{xy}\nu_{yx} - \nu_{yz}\nu_{zy} - \nu_{xz}\nu_{zx} - 2\nu_{yx}\nu_{zy}\nu_{xz}$[73]. E_i and ν_{ij} are the Young's modulus and Poisson's ratio in the respective directions. G_{ij} is the shear modulus in the (i, j)-plane. Then, we can calculate the bending moment. We define $\vec{M}_x$ to be the bending moment caused by stresses perpendicular to the x-axis. It follows that $\vec{M} = \vec{M}_x + \vec{M}_y + \vec{M}_z$ with

$$\vec{M}_i = \int_{\mathrm{A}} \left((j\hat{\mathbf{j}} + k\hat{\mathbf{k}}) \times (\sigma_{ii}\hat{\mathbf{i}} + \sigma_{ij}\hat{\mathbf{j}} + \sigma_{ik}\hat{\mathbf{k}}) \right) \mathrm{dA}. \tag{D.34}$$

Considering a plate with Length L, width W and thickness h, we can now calculate the bending moment. In cylindrical bending, the plate is wrapped around a cylinder. Therefore, ϕ_{ij} is approximately constant throughout the plate. However, in the case of more general bending, the rotation is not constant along any axis. Therefore, we take a small segment with length Δx, width Δy and height Δz. Over this segment, we assume ϕ_{ij} is constant. Additionally, we generally assume that h is small enough such that ϕ_{ij} is also constant with respect

to the normal of the mid-plane section. In the x-direction, we have

$$
\begin{aligned}
\vec{M}_x &= \int_{-\Delta y/2}^{\Delta y/2}\int_{-\Delta z/2}^{\Delta z/2}\Big[(\tilde{y}\hat{\mathbf{y}}+\tilde{z}\hat{\mathbf{z}})\times(\sigma_{xx}\hat{\mathbf{x}}+\sigma_{x\tilde{y}}\hat{\mathbf{y}}+\sigma_{x\tilde{z}}\hat{\mathbf{z}})\Big]\mathrm{d}\tilde{z}\mathrm{d}\tilde{y}\\
&= \int_{-\Delta y/2}^{\Delta y/2}\int_{-\Delta z/2}^{\Delta z/2}\Big[-\tilde{y}\sigma_{xx}\hat{\mathbf{z}}+\tilde{y}\sigma_{x\tilde{z}}\hat{\mathbf{x}}+\tilde{z}\sigma_{xx}\hat{\mathbf{y}}-\tilde{z}\sigma_{x\tilde{y}}\hat{\mathbf{x}}\Big]\mathrm{d}\tilde{z}\mathrm{d}\tilde{y}\\
&= \int_{-\Delta y/2}^{\Delta y/2}\int_{-\Delta z/2}^{\Delta z/2}\Big[-\tilde{y}(C_{11}\epsilon_{xx}+C_{12}\epsilon_{yy}+C_{13}\epsilon_{zz})\hat{\mathbf{z}}+\tilde{y}C_{55}\epsilon_{x\tilde{z}}\hat{\mathbf{x}}\\
&\qquad\qquad +\tilde{z}(C_{11}\epsilon_{xx}+C_{12}\epsilon_{yy}+C_{13}\epsilon_{zz})\hat{\mathbf{y}}-\tilde{z}C_{66}\epsilon_{x\tilde{y}}\hat{\mathbf{x}}\Big]\mathrm{d}\tilde{z}\mathrm{d}\tilde{y}\\
&= \int_{-\Delta y/2}^{\Delta y/2}\int_{-\Delta z/2}^{\Delta z/2}\Big[(\tilde{z}\hat{\mathbf{y}}-\tilde{y}\hat{\mathbf{z}})C_{11}\Big(x\frac{\partial\phi_{xx}}{\partial x}+\tilde{y}\frac{\partial\phi_{x\tilde{y}}}{\partial x}+\tilde{z}\frac{\partial\phi_{x\tilde{z}}}{\partial x}+\phi_{xx}\Big)\\
&\qquad\qquad +(\tilde{z}\hat{\mathbf{y}}-\tilde{y}\hat{\mathbf{z}})C_{12}\Big(x\frac{\partial\phi_{\tilde{y}x}}{\partial\tilde{y}}+\tilde{y}\frac{\partial\phi_{\tilde{y}\tilde{y}}}{\partial\tilde{y}}+\tilde{z}\frac{\partial\phi_{\tilde{y}\tilde{z}}}{\partial\tilde{y}}+\phi_{yy}\Big)\\
&\qquad\qquad +(\tilde{z}\hat{\mathbf{y}}-\tilde{y}\hat{\mathbf{z}})C_{13}\Big(x\frac{\partial\phi_{\tilde{z}x}}{\partial\tilde{z}}+\tilde{y}\frac{\partial\phi_{\tilde{z}\tilde{y}}}{\partial\tilde{y}}+\tilde{z}\frac{\partial\phi_{\tilde{z}\tilde{z}}}{\partial\tilde{z}}+\phi_{zz}\Big)\\
&\qquad\qquad +\frac{\tilde{y}\hat{\mathbf{x}}C_{55}}{2}\Big\{x\Big(\frac{\partial\phi_{xx}}{\partial\tilde{z}}+\frac{\partial\phi_{\tilde{z}x}}{\partial x}\Big)-\tilde{y}\Big(\frac{\partial\phi_{x\tilde{y}}}{\partial\tilde{z}}+\frac{\partial\phi_{\tilde{z}\tilde{y}}}{\partial x}\Big)+\tilde{z}\Big(\frac{\partial\phi_{x\tilde{z}}}{\partial\tilde{z}}+\frac{\partial\phi_{\tilde{z}\tilde{z}}}{\partial x}\Big)\Big\}\\
&\qquad\qquad +\frac{\tilde{z}\hat{\mathbf{x}}C_{66}}{2}\Big\{x\Big(\frac{\partial\phi_{xx}}{\partial\tilde{y}}+\frac{\partial\phi_{\tilde{y}x}}{\partial x}\Big)+\tilde{y}\Big(\frac{\partial\phi_{x\tilde{y}}}{\partial\tilde{y}}+\frac{\partial\phi_{\tilde{y}\tilde{y}}}{\partial x}\Big)+\tilde{z}\Big(\frac{\partial\phi_{x\tilde{y}}}{\partial\tilde{y}}+\frac{\partial\phi_{\tilde{y}\tilde{z}}}{\partial x}\Big)\Big\}\\
&\qquad\qquad \Big]\mathrm{d}\tilde{z}\mathrm{d}\tilde{y}.
\end{aligned}
\tag{D.35}
$$

Then, using symmetry, we can remove any odd functions in y and z. Additionally, we assume that the angles of bending do not change over a small segment, with length Δx, width Δy and height Δz. We obtain

$$
\begin{aligned}
\vec{M}_x = \int_{-\Delta y/2}^{\Delta y/2}\int_{-\Delta z/2}^{\Delta z/2}\Big[&C_{11}\Big(\hat{\mathbf{y}}\tilde{z}^2\frac{\partial\phi_{x\tilde{z}}}{\partial x}-\hat{\mathbf{z}}\tilde{y}^2\frac{\partial\phi_{x\tilde{y}}}{\partial x}\Big)+C_{12}\Big(\hat{\mathbf{y}}\tilde{z}^2\frac{\partial\phi_{\tilde{y}\tilde{z}}}{\partial\tilde{y}}-\hat{\mathbf{z}}\tilde{y}^2\frac{\partial\phi_{\tilde{y}\tilde{y}}}{\partial\tilde{y}}\Big)+C_{13}\Big(\hat{\mathbf{y}}\tilde{z}^2\frac{\partial\phi_{\tilde{z}\tilde{z}}}{\partial\tilde{z}}-\hat{\mathbf{z}}\tilde{y}^2\frac{\partial\phi_{\tilde{z}\tilde{y}}}{\partial\tilde{z}}\Big)\\
&+\frac{\tilde{y}^2\hat{\mathbf{x}}C_{55}}{2}\Big(\frac{\partial\phi_{x\tilde{y}}}{\partial\tilde{z}}+\frac{\partial\phi_{\tilde{z}\tilde{y}}}{\partial x}\Big)-\frac{\tilde{z}^2\hat{\mathbf{x}}C_{66}}{2}\Big(\frac{\partial\phi_{x\tilde{y}}}{\partial\tilde{y}}+\frac{\partial\phi_{\tilde{y}\tilde{z}}}{\partial x}\Big)\Big]\mathrm{d}\tilde{z}\mathrm{d}\tilde{y}
\end{aligned}
\tag{D.36}
$$

and

$$
\begin{aligned}
\vec{M}_x &= \Big\{\frac{C_{55}\hat{\mathbf{x}}}{2}\Big(\frac{\partial\phi_{xy}}{\partial z}+\frac{\partial\phi_{zy}}{\partial x}\Big)-\Big(C_{11}\frac{\partial\phi_{xy}}{\partial x}+C_{12}\frac{\partial\phi_{yy}}{\partial y}+C_{13}\frac{\partial\phi_{zy}}{\partial z}\Big)\hat{\mathbf{z}}\Big\}\Delta z\int_{-\Delta y/2}^{\Delta y/2}\big[\tilde{y}^2\big]\mathrm{d}\tilde{y}\\
&\quad+\Big\{\Big(C_{11}\frac{\partial\phi_{xz}}{\partial x}+C_{12}\frac{\partial\phi_{yz}}{\partial y}+C_{13}\frac{\partial\phi_{zz}}{\partial z}\Big)\hat{\mathbf{y}}-\frac{C_{66}\hat{\mathbf{x}}}{2}\Big(\frac{\partial\phi_{xy}}{\partial y}+\frac{\partial\phi_{yz}}{\partial x}\Big)\Big\}\Delta y\int_{-\Delta z/2}^{\Delta z/2}\big[\tilde{z}^2\big]\mathrm{d}\tilde{z}\\
&= \Big\{\frac{C_{55}\hat{\mathbf{x}}}{2}\Big(\frac{\partial\phi_{xy}}{\partial z}+\frac{\partial\phi_{zy}}{\partial x}\Big)-\Big(C_{11}\frac{\partial\phi_{xy}}{\partial x}+C_{12}\frac{\partial\phi_{yy}}{\partial y}+C_{13}\frac{\partial\phi_{zy}}{\partial z}\Big)\hat{\mathbf{z}}\Big\}\frac{\Delta z(\Delta y)^3}{12}\\
&\quad+\Big\{\Big(C_{11}\frac{\partial\phi_{xz}}{\partial x}+C_{12}\frac{\partial\phi_{yz}}{\partial y}+C_{13}\frac{\partial\phi_{zz}}{\partial z}\Big)\hat{\mathbf{y}}-\frac{C_{66}\hat{\mathbf{x}}}{2}\Big(\frac{\partial\phi_{xy}}{\partial y}+\frac{\partial\phi_{yz}}{\partial x}\Big)\Big\}\frac{\Delta y(\Delta z)3}{12}.
\end{aligned}
\tag{D.37}
$$

Similarly, for the y- and z- direction, we have

$$
\begin{aligned}
\vec{M}_y &= \frac{\Delta z(\Delta x)^3}{12}\Big\{\Big(C_{12}\frac{\partial\phi_{xx}}{\partial x}+C_{22}\frac{\partial\phi_{yx}}{\partial y}+C_{23}\frac{\partial\phi_{zx}}{\partial z}\Big)\hat{\mathbf{z}}-\frac{C_{44}}{2}\Big(\frac{\partial\phi_{yx}}{\partial z}+\frac{\partial\phi_{zx}}{\partial y}\Big)\hat{\mathbf{y}}\Big\}\\
&\quad+\frac{\Delta x(\Delta z)3}{12}\Big\{\frac{C_{66}}{2}\Big(\frac{\partial\phi_{xz}}{\partial y}+\frac{\partial\phi_{yz}}{\partial x}\Big)\hat{\mathbf{y}}-\Big(C_{12}\frac{\partial\phi_{xz}}{\partial x}+C_{22}\frac{\partial\phi_{yz}}{\partial y}+C_{23}\frac{\partial\phi_{zz}}{\partial z}\Big)\hat{\mathbf{x}}\Big\}
\end{aligned}
\tag{D.38}
$$

and

$$
\begin{aligned}
\vec{M}_z &= \frac{\Delta x(\Delta y)^3}{12}\Big\{\Big(C_{13}\frac{\partial\phi_{xy}}{\partial x}+C_{23}\frac{\partial\phi_{yy}}{\partial y}+C_{33}\frac{\partial\phi_{zy}}{\partial z}\Big)\hat{\mathbf{x}}-\frac{C_{55}}{2}\Big(\frac{\partial\phi_{zy}}{\partial x}+\frac{\partial\phi_{xy}}{\partial z}\Big)\hat{\mathbf{z}}\Big\}\\
&\quad+\frac{\Delta y(\Delta x)^3}{12}\Big\{\frac{C_{44}}{2}\Big(\frac{\partial\phi_{zx}}{\partial y}+\frac{\partial\phi_{yx}}{\partial z}\Big)\hat{\mathbf{z}}-\Big(C_{13}\frac{\partial\phi_{xx}}{\partial x}+C_{23}\frac{\partial\phi_{yx}}{\partial y}+C_{33}\frac{\partial\phi_{zx}}{\partial z}\Big)\hat{\mathbf{y}}\Big\}
\end{aligned}
\tag{D.39}
$$

Using $\vec{M} = \vec{M}_x + \vec{M}_y + \vec{M}_z$, we get

$$\begin{aligned}\vec{M} = &\frac{(\Delta y)^3}{12}\Bigg\{\left(C_{13}\frac{\partial\phi_{xy}}{\partial x} + C_{23}\frac{\partial\phi_{yy}}{\partial y} + C_{33}\frac{\partial\phi_{zy}}{\partial z}\right)\Delta x\hat{\mathbf{x}} - \left(C_{11}\frac{\partial\phi_{xy}}{\partial x} + C_{12}\frac{\partial\phi_{yy}}{\partial y} + C_{13}\frac{\partial\phi_{zy}}{\partial z}\right)\Delta z\hat{\mathbf{z}} \\ &+ \frac{C_{55}}{2}\left(\frac{\partial\phi_{zy}}{\partial x} + \frac{\partial\phi_{xy}}{\partial z}\right)(\Delta z\hat{\mathbf{x}} - \Delta x\hat{\mathbf{z}})\Bigg\} \\ &+\frac{(\Delta z)3}{12}\Bigg\{\left(C_{11}\frac{\partial\phi_{xz}}{\partial x} + C_{12}\frac{\partial\phi_{yz}}{\partial y} + C_{13}\frac{\partial\phi_{zz}}{\partial z}\right)\Delta x\hat{\mathbf{y}} - \left(C_{12}\frac{\partial\phi_{xz}}{\partial x} + C_{22}\frac{\partial\phi_{yz}}{\partial y} + C_{23}\frac{\partial\phi_{zz}}{\partial z}\right)\Delta y\hat{\mathbf{x}} \\ &+ \frac{C_{66}}{2}\left(\frac{\partial\phi_{xz}}{\partial y} + \frac{\partial\phi_{yz}}{\partial x}\right)(\Delta x\hat{\mathbf{y}} - \Delta y\hat{\mathbf{x}})\Bigg\} \\ &+\frac{(\Delta x)^3}{12}\Bigg\{\left(C_{12}\frac{\partial\phi_{xx}}{\partial x} + C_{23}\frac{\partial\phi_{yx}}{\partial y} + C_{23}\frac{\partial\phi_{zx}}{\partial z}\right)\Delta y\hat{\mathbf{z}} - \left(C_{13}\frac{\partial\phi_{xx}}{\partial x} + C_{23}\frac{\partial\phi_{yx}}{\partial y} + C_{23}\frac{\partial\phi_{zx}}{\partial z}\right)\Delta z\hat{\mathbf{y}} \\ &+ \frac{C_{44}}{2}\left(\frac{\partial\phi_{zx}}{\partial y} + \frac{\partial\phi_{yx}}{\partial z}\right)(\Delta y\hat{\mathbf{z}} - \Delta z\hat{\mathbf{y}})\Bigg\}.\end{aligned} \tag{D.40}$$

For thin plates and small transverse angles, ϕ_{ij} with $i \neq j$, the stretching of a small segment $\delta i_i \ll \Delta i$. Therefore, $\phi_{ii} = 0$. We have a transverse shear force

$$Q_{xz} = \int_{\mathrm{A}} \sigma_{xz}\mathrm{dA} = \frac{\kappa G_{xz}\Delta z\Delta y}{2}\left(\frac{\partial U_z}{\partial x} - y_0\frac{\partial\phi_{xy}}{\partial z} - z_0\frac{\partial\phi_{xz}}{\partial z} + \phi_{xz}\right), \tag{D.41}$$

with $\kappa \approx \frac{5}{6}$[71]. For thin plates, $G_{iz} \propto \frac{1}{\Delta x\Delta y\Delta z} \to \infty$[74], the angle does not change over z and $z_0 = 0$. Therefore, $\frac{\partial\phi_{ij}}{\partial z} = 0$. Thus for $i \in \{x, y\}$, we have

$$\frac{\partial U_z}{\partial i} = -\phi_{iz}. \tag{D.42}$$

For a vibrating plate, we assume that there are no the external forces in the x- and y-direction. Additionally, we assume that the internal forces throughout the plate are symmetric in both plane directions for transverse vibrations. Therefore, $\phi_{xy} = \phi_{yx} = 0$. Hence Equation D.40 becomes

$$\begin{aligned}\vec{M} =&\frac{(\Delta z)3}{12}\left\{\left(C_{12}\frac{\partial^2 U_z}{\partial x^2} + C_{22}\frac{\partial^2 U_z}{\partial y^2}\right)\Delta x\hat{\mathbf{x}} - \left(C_{11}\frac{\partial^2 U_z}{\partial x^2} + C_{12}\frac{\partial^2 U_z}{\partial y^2}\right)\Delta y\hat{\mathbf{y}} + G_{xy}\frac{\partial^2 U_z}{\partial x\partial y}(\Delta y\hat{\mathbf{x}} - \Delta x\hat{\mathbf{y}})\right\} \\ &+ \frac{G_{xz}(\Delta y)^3}{24}\frac{\partial^2 U_z}{\partial x\partial y}(\Delta x\hat{\mathbf{z}} - \Delta z\hat{\mathbf{x}}) + \frac{G_{yz}(\Delta x)^3}{24}\frac{\partial^2 U_z}{\partial x\partial y}(\Delta z\hat{\mathbf{y}} - \Delta y\hat{\mathbf{z}}).\end{aligned} \tag{D.43}$$

We see that, if we consider an isotropic plate, $C_{11} = C_{22} = E$ and $G_{xz} = G_{yz} = G_{xy} = G$. Then consider pure bending, meaning $G = 0$, and an incompressible material in the (x, y)-direction, meaning $\nu_{xy} = \nu_{yx} = 0$. Take $\Delta z = h$ for a thin plate and we obtain the bending moment found in Equation D.21.

Analogous to the derivation given by Neville H. Fletcher, we can find the governing partial differential equation by setting the bending moment to be the cross product of the position vector $\vec{r} = (\mathrm{d}x\hat{\mathbf{x}} + \mathrm{d}y\hat{\mathbf{y}} + \mathrm{d}z\hat{\mathbf{z}})$ with some net force $\vec{F}$. Though, we have already assumed the force in the x- and y-directions to be zero. Therefore the net force can be given by $F_z\hat{\mathbf{z}}$. The bending moment is then given by $\vec{M} = (\mathrm{d}x\hat{\mathbf{x}}+\mathrm{d}y\hat{\mathbf{y}}+\mathrm{d}z\hat{\mathbf{z}})\times F_z\hat{\mathbf{z}} = \mathrm{d}yF_z\hat{\mathbf{x}}-\mathrm{d}xF_z\hat{\mathbf{y}}$. Taking the inner product with $\hat{\mathbf{x}}$ and $\hat{\mathbf{y}}$ gives two separate equations:

$$\vec{M}\cdot\hat{\mathbf{x}} = \mathrm{d}yF_z \tag{D.44}$$

and

$$\vec{M}\cdot\hat{\mathbf{y}} = -\mathrm{d}xF_z. \tag{D.45}$$

We can express this as a derivative and combine the two equations to obtain

$$\begin{aligned}F_z =&\frac{1}{2}\left(\frac{\partial\vec{M}\cdot\hat{\mathbf{x}}}{\partial y} - \frac{\partial\vec{M}\cdot\hat{\mathbf{y}}}{\partial x}\right) \\ =&\frac{(\Delta z)^3}{24}\left[\Delta yC_{11}\frac{\partial^3 U_z}{\partial x^3} + \Delta x(C_{12}+G_{xy})\frac{\partial^3 U_z}{\partial x^2\partial y} + \Delta y(C_{12}+G_{xy})\frac{\partial^3 U_z}{\partial x\partial y^2} + \Delta xC_{22}\frac{\partial^3 U_z}{\partial y^3}\right] \\ &- \frac{\Delta z}{48}\left[G_{xz}(\Delta y)^3\frac{\partial^3 U_z}{\partial x\partial y^2} + G_{yz}(\Delta x)^3\frac{\partial^3 U_z}{\partial x^2\partial y}\right].\end{aligned} \tag{D.46}$$

Then split F_z into the terms depending on Δx and Δy respectively. We write $\Delta F_z = \Delta F_{z,\Delta x} + \Delta F_{z,\Delta y}$. Notice that the net shear force $F_{z,\Delta i}$ is not constant over j. Therefore, we can write $\Delta F_{z,\Delta i} = \left(\frac{\partial F_{z,\Delta i}}{\partial j}\right)\Delta j$. Additionally, we write $\Delta F_z = -\rho \Delta x \Delta y \Delta z \frac{\partial^2 U_z}{\partial t^2}$. To obtain the flexural wave equation for thin plates, we take $\Delta z = h$. Additionally, to simplify the equation, we take $\Delta x \approx \Delta y \approx \Delta z = h$. It follows that

$$\rho h \frac{\partial^2 U_z}{\partial t^2} + \frac{h^3}{24}\left[C_{11}\frac{\partial^4 U_z}{\partial x^4} + 2(C_{12} + G_{xy} + G_{xz}/4 + G_{yz}/4)\frac{\partial^4 U_z}{\partial x^2 \partial y^2} + C_{22}\frac{\partial^4 U_z}{\partial y^4}\right] = 0 \tag{D.47}$$

We have now obtained the bending wave equation for orthotropic plates without external force. For the flexural wave equation used in subsection 3.3, we consider a form of pure bending; hence $G_{ij} = 0$. Also, we consider the material of the plate to be symmetric with respect to Poisson's ratio, or $\nu_{ij} = \nu_{ji}$. Then we assume that the materials properties adhere to the relation

$$\nu_{xy} \approx 1 - 2\nu_{xz}\nu_{yz}. \tag{D.48}$$

Finally, we account for the external force $\vec{F}_{ext}$, as the bending moment only describes the stresses caused by deformation in the material. Similar to the net force, the external force can be written as $\vec{F}_{ext} = \rho \Delta x \Delta y \Delta z \vec{a}$, where $\vec{a}$ is the acceleration vector. It follows that the z-component is given by $F_{ext,z} = \rho \Delta x \Delta y \Delta z \mathrm{a}_z$. Now we have found the flexural wave equation in the following form:

$$\rho h \frac{\partial^2 U_z}{\partial t^2} + \frac{h^3}{24}\left[C_{11}\frac{\partial^4 U_z}{\partial x^4} + 2C_{12}\frac{\partial^4 U_z}{\partial x^2 \partial y^2} + C_{22}\frac{\partial^4 U_z}{\partial y^4}\right] + \rho h \mathrm{a}_z = 0, \tag{D.49}$$

with $C_{12} \approx \sqrt{C_{11}C_{22}}$. We find the flexural wave equation as given by Equation 3.1 if and only if C_0 can be written as

$$C_0 = \frac{1}{2}(1 - \nu_{xz}^2)(1 - \nu_{yz}^2). \tag{D.50}$$

Note that Equation D.49 is irreducible if Equation D.50 does not hold. Additionally, if Equation D.48 does not hold, $C_{12} = \frac{E_x}{C_0}(\nu_{yx} + \nu_{yz}\nu_{zx})$. Though, if both relations hold, and therefore impose physical properties on the wooden plates, we find the required form of the flexural wave equation, given by

$$\frac{\partial^2 U_z}{\partial t^2} + B_{11}\frac{\partial^4 U_z}{\partial x^4} + 2B_{12}\frac{\partial^4 U_z}{\partial x^2 \partial y^2} + B_{22}\frac{\partial^4 U_z}{\partial y^4} + \mathrm{a}_z = 0, \tag{D.51}$$

with $B_{ii} = \frac{h^2 E_i}{12\rho(1-\nu_{xz}^2)}$ and $B_{xy} = \sqrt{B_{xx}B_{yy}}$.

E The flexural wave equation on a square plate

For a rectangular plate, we know that $\Omega = \{(x, y) \mid x \in [0, L], y \in [0, W]\}$. To demonstrate the free and clamped end, we showcase three different plates:

1. A rectangular plate with solely clamped edges
2. A rectangular plate with solely free edges
3. A rectangular cantilever plate with one clamped edge and three free edges

First, consider a homogeneous rectangular plate with only clamped edges and without external forces. This means the partial differential equation[28] looks as follows:

$$\frac{\partial^2 U}{\partial t^2} + \frac{Eh^2}{12\rho(1-\nu^2)}\nabla^4 U + g = 0 \tag{E.1}$$

$$U(0, y, t) = 0 \quad \frac{\partial U}{\partial x}(0, y, t) = 0 \tag{E.2}$$

$$U(L, y, t) = 0 \quad \frac{\partial U}{\partial x}(L, y, t) = 0 \tag{E.3}$$

$$U(x, 0, t) = 0 \quad \frac{\partial U}{\partial y}(x, 0, t) = 0 \tag{E.4}$$

$$U(x, W, t) = 0 \quad \frac{\partial U}{\partial y}(x, W, t) = 0 \tag{E.5}$$

$$U(x, y, 0) = v(x, y) \quad \frac{\partial U}{\partial t}(x, y, 0) = w(x, y), \tag{E.6}$$

where U is the displacement along the z-direction, E is Young's Modulus, h is the thickness, ρ is the density and ν is Poisson's ratio. g is the gravitational acceleration and $v, w(x, y)$ are sufficiently smooth functions such that all partial derivatives shown in eqs. (E.1) to (E.5) exist. Note that, even though the plate has a thickness in the model, the set $\Omega \subset \mathbb{R}^2$ and the function $U : \Omega \to \mathbb{R}$ are still sufficient to solve the initial value problem described by eqs. (E.1) to (E.5) as long as we assume the top and bottom plates to be completely flat; without curvature of the plates in equilibrium. If this was not the case, we would need $\Omega \subset \mathbb{R}^3$ and U defined accordingly on the domain Ω.

If a cantilever plate is considered, three ends are free. Additionally, we assume that the plate is not necessarily homogeneous. This means the partial differential equation is as follows:

$$h\frac{\partial^2 U}{\partial t^2} + B_{xx}\frac{\partial^4 U}{\partial x^4} + 2B_{xy}\frac{\partial^4 U}{\partial x^2 \partial y^2} + B_{yy}\frac{\partial^4 U}{\partial y^4} + g = 0 \tag{E.7}$$

$$U(0, y, t) = 0 \quad \frac{\partial U}{\partial x}(0, y, t) = 0 \tag{E.8}$$

$$\frac{\partial^2 U}{\partial x^2}(L, y, t) = 0 \quad \frac{\partial^3 U}{\partial x^3}(L, y, t) = 0 \tag{E.9}$$

$$\frac{\partial^2 U}{\partial y^2}(x, 0, t) = 0 \quad \frac{\partial^3 U}{\partial y^3}(x, 0, t) = 0 \tag{E.10}$$

$$\frac{\partial^2 U}{\partial y^2}(x, W, t) = 0 \quad \frac{\partial^3 U}{\partial y^3}(x, W, t) = 0 \tag{E.11}$$

$$U(x, y, 0) = v(x, y) \quad \frac{\partial U}{\partial t}(x, y, 0) = w(x, y), \tag{E.12}$$

where h is the thickness, g the gravitational acceleration, $B_{xx}, B_{xy}, B_{yx}, B_{yy}$ are constants given by eqs. (2.19) to (2.21) for directivity and $v(x, y), w(x, y)$ are sufficiently smooth functions.

In the case of solely free edges, the governing equation of motion is the same as Equation E.7. However the boundary conditions become

$$\frac{\partial^2 U}{\partial x^2}(0,y,t) = 0 \quad \frac{\partial^3 U}{\partial x^3}(0,y,t) = 0 \tag{E.13}$$

$$\frac{\partial^2 U}{\partial x^2}(L,y,t) = 0 \quad \frac{\partial^3 U}{\partial x^3}(L,y,t) = 0 \tag{E.14}$$

$$\frac{\partial^2 U}{\partial y^2}(x,0,t) = 0 \quad \frac{\partial^3 U}{\partial y^3}(x,0,t) = 0 \tag{E.15}$$

$$\frac{\partial^2 U}{\partial y^2}(x,W,t) = 0 \quad \frac{\partial^3 U}{\partial y^3}(x,W,t) = 0. \tag{E.16}$$

In a similar fashion to two plates with generalised surfaces, we can also couple two rectangular plates. A schematic of the plates by means of ribs is shown in Figure 55.

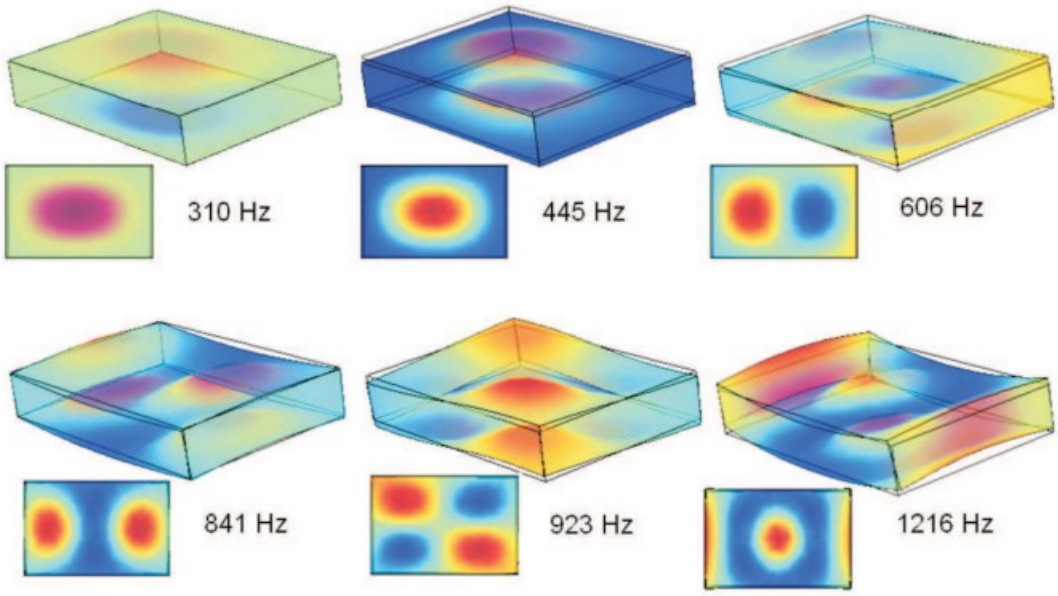

Figure 55: A schematic of two rectangular plates coupled by ribs. Additionally, some possible normal modes on the structure are shown[44].

F Difference equations

To describe an equation of motion numerically, we will descretise it. For this descretisation, we use difference equations $Q_f(h)$. The idea of a difference equation is that, if you take the limit of the distance between points on the grid $h \in \mathbb{R}$ to zero, we will obtain the derivative. For example:

$$\lim_{h\to 0} Q_f(h) = \lim_{h\to 0} \frac{f(x+h) - f(x)}{h} = f'(x), \tag{F.1}$$

for $h > 0$. However, in reality, h cannot be infinitesimally small. Therefore, $\frac{f(x+h)-f(x)}{h}$ has a truncation error. We can calculate this error by using a Taylor expansion about x. This shows that the truncation error is given by $R(h) = \frac{-h}{2} f''(\zeta)$ for $\zeta \in (x, x+h)$. This error is largely due to the linearity of the step forward we take. We can attempt a similar difference equation with a step backward:

$$\lim_{h\to 0} Q_b(h) = \lim_{h\to 0} \frac{f(x) - f(x-h)}{h} = f'(x), \tag{F.2}$$

for $h > 0$. In this case, we have a similar truncation error $R(h) = -\frac{-h}{2} f''(\zeta)$ for $\zeta \in (x-h, x)$. We can reduce the truncation error by combining both difference equations to obtain:

$$\lim_{h\to 0} Q_c(h) = \lim_{h\to 0} \frac{f(x+h) - f(x-h)}{2h} = f'(x), \tag{F.3}$$

for $h > 0$. In this equation, we evaluate the node at the centre of two other points. The resulting truncation error is given by $\frac{h^2}{6} f'''(\zeta)$ for $\zeta \in (x-h, x+h)$. We can visualise this as the forward step and the backward step somewhat compensate their errors. However, $\frac{h^2}{6} f'''(\zeta)$ is still quite large, the importance of which will become evident later on.

Equation F.3 is referred to as the central difference equation. Though, in Equation 3.9, we have got a fourth order derivative. To derive this, we will apply the central difference equation we have just found to itself three more times. We obtain:

$$Q_{c,2} = \frac{f(x+2h) - 2f(x) + f(x-2h)}{(2h)^2} \tag{F.4}$$

,

$$Q_{c,3} = \frac{f(x+3h) - 3f(x+h) + 3f(x-h) - f(x-3h)}{(2h)^3} \tag{F.5}$$

and

$$Q_{c,4} = \frac{f(x+4h) - 4f(x+2h) + 6f(x) - 4f(x-2h) + f(x-4h)}{(2h)^4}. \tag{F.6}$$

The equations of motions apply to the whole rod, thus to reduce the form of the 4_{th} order differences equation in complexity, we will create invisible grid points. Namely, between every two grid points i and $i+1$, for $i \in ([1, n] \cap \mathbb{Z})$, we will create a new grid point $i + 0.5$ such that the distance the between original two grid points and the new grid point is equal. We will then evaluate the 2_{nd} and 4_{th} order central difference equation on grid point i, but we will take into account the invisible grid points to obtain:

$$Q_{c,2} = \frac{f(x+h) - 2f(x) + f(x-h)}{h^2} \tag{F.7}$$

and

$$Q_{c,4} = \frac{f(x+2h) - 4f(x+h) + 6f(x) - 4f(x-h) + f(x-2h)}{h^4} \tag{F.8}$$

Unfortunately, we cannot not do this for the 3_{rd} order central difference equation as it contains $f(x+h)$ and $f(x-h)$. Namely, we can provide values for prior known functions at some point $x + \frac{1}{3}h$, but not f itself. If we try this, we would need to evaluate f at the invisible grid points which causes them to become visible.

G Stiffness matrix for a bending rod

Equation 4.8 describes the numerical model for the bending rod. For example, the third row reads:

$$-\frac{\partial^2 \omega_3}{\partial t} = \frac{\omega_5 - 4\omega_4 + 6\omega_1 - 4\omega_2 + \omega_1}{h^4} + f_3. \tag{G.1}$$

This result is obtained by using the fourth order central difference equation, found in Equation F.8.

In the case of a stationary bending rod with an external driving force, $I\frac{\partial^2 \vec{\omega}}{\partial t^2} = \vec{0}$. This yields a simple matrix vector equation:

$$S\vec{\omega} = -\vec{f}. \tag{G.2}$$

Note that $\vec{f}$ is the collection of all non-linear terms in the difference equations and often stands for both the external driving force and the non-linear parts of boundary conditions.

We can now describe all points on the grid to which the difference equation does not exceed the boundary, or internal grid points in S. Thus, we can fill in the whole matrix S except the first two and the bottom two rows. We obtain:

$$S = \begin{bmatrix} ? & ? & ? & ? & ? & ? & ? & \dots & ? \\ ? & ? & ? & ? & ? & ? & ? & \dots & ? \\ 1 & -4 & 6 & -4 & 1 & 0 & 0 & \dots & 0 \\ 0 & 1 & -4 & 6 & -4 & 1 & 0 & \dots & 0 \\ \vdots & \vdots & \vdots & \vdots & \vdots & \vdots & \vdots & \ddots & 0 \\ 0 & \dots & 0 & 1 & -4 & 6 & -4 & 1 & 0 \\ 0 & \dots & 0 & 0 & 1 & -4 & 6 & -4 & 1 \\ ? & \dots & ? & ? & ? & ? & ? & ? & ? \\ ? & \dots & ? & ? & ? & ? & ? & ? & ? \end{bmatrix}. \tag{G.3}$$

G.1 Boundary conditions for a clamped end

To determine the boundary conditions in finite difference form, we will first state the finite difference equations on the grid points, then discretise the boundary conditions and use them appropriately to get rid of non-existing points. The difference equations for the first two nodes read as follows:

$$\frac{\omega_3 - 4\omega_2 + 6\omega_1 - 4\omega_0 + \omega_{-1}}{h^4} = -f_1 \tag{G.4}$$

and

$$\frac{\omega_4 - 4\omega_3 + 6\omega_2 - 4\omega_1 + \omega_0}{h^4} = -f_2. \tag{G.5}$$

The first boundary condition at $x = 0$, $y(0) = 0$ gives us that $\omega_0 = 0$ directly. The second boundary condition at $x = 0$ is $\frac{\partial y}{\partial x}\Big|_{x=0} = 0$. Technically, using central differences, this is a condition for the first node relating a ghost point, ω_0, with the existing node ω_2. We obtain:

$$\frac{\omega_2 - \omega_0}{2h} = 0. \tag{G.6}$$

We can simply deduce that $\omega_2 = \omega_0$. Additionally, $\omega_0 = 0$ still holds. Plugging these results into the equation for the second node yields:

$$\frac{\omega_4 - 4\omega_3 - 4\omega_1}{h^4} = -f_2. \tag{G.7}$$

This difference equation does not contain any ghost points, thus can be fully described in the matrix S.

The first node still contains ω_{-1}. Remember that we have used a trick with invisible grid points. We will now use the same logic but in reverse. The central difference equation is evaluated with a certain step size a on both sides of the node. But if we take $a = 2h$, the central difference equation still holds. Using this for the boundary condition yield:

$$\frac{\omega_3 - \omega_{-1}}{4h} = 0. \tag{G.8}$$

Note that the n_{th} order central difference equation with $a = h$ and the n_{th} order central difference equation with $a = 2h$ appropriately approximate the n_{th} derivatives . The truncation errors are even of the same order of magnitude. This turns out to be $O(h^n)$ and $O((2h)^n)$ respectively[61]. This, by definition[75], is of the same order since the factor 2 is constant for any order central difference equation. Therefore, we can use the difference equations with any (reasonable) step size.

Thus the difference equation for the first node is as follows:

$$\frac{2\omega_3 + 6\omega_1}{h^4} = -f_1. \tag{G.9}$$

G.2 Boundary conditions for a free end

Having seen the boundary conditions for the clamped end at $x = 0$, we will attempt a similar method for the boundary conditions at $x = L$.

The difference equations for the n_{th} and $(n+1)_{th}$ nodes read as follows:

$$\frac{\omega_{n+2} - 4\omega_{n+1} + 6\omega_{n+} - 4\omega_{n-1} + \omega_{n-2}}{h^4} = -f_n \tag{G.10}$$

and

$$\frac{\omega_{n+3} - 4\omega_{n+2} + 6\omega_{n+1} - 4\omega_n + \omega_{n-1}}{h^4} = -f_{n+1}. \tag{G.11}$$

The boundary conditions for a free end at $x = L$ are $\frac{\partial^2 y}{\partial x^2}\Big|_{x=L} = 0$ and $\frac{\partial^3 y}{\partial x^3}\Big|_{x=L} = 0$. In difference equations, this yields:

$$\frac{\omega_{n+2} - 2\omega_{n+1} + \omega_n}{h^2} = 0 \tag{G.12}$$

and

$$\frac{\omega_{n+4} - 3\omega_{n+2} + 3\omega_n - \omega_{n-2}}{(2h)^3} = 0. \tag{G.13}$$

This will not fix the problem that the equation pertaining grid point $i = n, n+1$ contains a term ω_{n+3} and Equation G.13 contains a term ω_{n+4}. We can, however, fix this by using the backward difference equation, as shown in Equation F.1 once, to approximate $\frac{\partial^3 y}{\partial x^3}\Big|_{x=L} = 0$, and then applying the central difference equation twice to obtain this term. Note that this is a valid way to approximate the 3_{rd} order derivative. Though the order of the truncation error is higher[61]. We start with the forward difference equation on the $(n+1)_{th}$ node:

$$Q_b = \frac{\omega_{n+1} - \omega_n}{h}. \tag{G.14}$$

Then, applying the central difference equation twice yields the following:

$$Q_{bc} = \frac{\omega_{n+2} - \omega_{n+1} - \omega_n + \omega_{n-1}}{2h^2} \tag{G.15}$$

and

$$Q_{bcc} = \frac{\omega_{n+3} - \omega_{n+2} - 2\omega_{n+1} + 2\omega_n + \omega_{n-1} - \omega_{n-2}}{4h^3}. \tag{G.16}$$

The resulting boundary condition looks as follows:

$$\frac{\omega_{n+3} - \omega_{n+2} - 2\omega_{n+1} + 2\omega_n + \omega_{n-1} - \omega_{n-2}}{4h^3} = 0. \tag{G.17}$$

Using Equation G.11, Equation G.12 and Equation G.17 gives us:

$$\frac{2\omega_{n+1} - 3\omega_n + \omega_{n-2}}{h^3} = -f_{n+1}. \tag{G.18}$$

Now, moving on to the last unknown row of S, for the n_{th} node, we find that $\omega_{n+2} - 2\omega_{n+1} = \omega_n$ by Equation G.12. Using this, the difference equation becomes as follows:

$$\frac{\omega_{n+2} - 4\omega_{n+1} + 6\omega_n - 4\omega_{n-1} + \omega_{n-2}}{h^4} = -f_n. \tag{G.19}$$

We can plug the boundary condition in to find:

$$\frac{-2\omega_{n+1} + 5\omega_n - 4\omega_{n-1} + \omega_{n-2}}{h^4} = -f_n. \tag{G.20}$$

We now have the entire matrix vector equation for a stationary bending rod without external force ($\vec{f} = 0$):

$$\begin{bmatrix} 6 & 0 & 2 & 0 & 0 & 0 & 0 & \dots & 0 \\ -4 & 0 & -4 & 1 & 0 & 0 & 0 & \dots & 0 \\ 1 & -4 & 6 & -4 & 1 & 0 & 0 & \dots & 0 \\ 0 & 1 & -4 & 6 & -4 & 1 & 0 & \dots & 0 \\ \vdots & \vdots & \vdots & \vdots & \vdots & \vdots & \vdots & \ddots & 0 \\ 0 & \dots & 0 & 1 & -4 & 6 & -4 & 1 & 0 \\ 0 & \dots & 0 & 0 & 1 & -4 & 6 & -4 & 1 \\ 0 & \dots & 0 & 0 & 0 & 1 & -4 & 5 & -2 \\ 0 & \dots & 0 & 0 & 0 & 1 & 0 & -3 & 2 \end{bmatrix} \vec{\omega} = \vec{0}. \tag{G.21}$$

G.3 The bending rod

To consider external forces, such as gravity, we need to take a better look at the equation of motion. The equation of motion from which Equation 3.9 is derived, is as follows[28]:

$$dF = \Big(\frac{\partial F}{\partial x}\Big)dx = (\rho A dx)\frac{\partial^2 U}{\partial t^2}, \tag{G.22}$$

where F is the net force perpendicular to the axis of the bar and A the cross sectional area. In the case of a bending rod, the net force is described by bending moment and other external forces between two points x_0 and $x_0 + dx$ on the axis of the rod:

$$F = \frac{\partial \hat{M}}{\partial x} + F_{ext} = -EAK^2\frac{\partial^3 U}{\partial x^3} - \rho A a(x,t)dx, \tag{G.23}$$

with F_{ext} the external force applied to the rod and $a(x,t)$ the acceleration. Combining Equation G.22 and Equation G.23 yields:

$$\frac{\partial^2 U}{\partial t^2} + \frac{EK^2}{\rho}\frac{\partial^4 U}{\partial x^4} + a(x,t) = 0. \tag{G.24}$$

The analytical solution to Equation 4.1 for the stationary case is follows from a dummy case (using ξ as a variable):

$$\frac{\partial^4 \hat{U}}{\partial x^4} = \xi, \qquad \xi \in \mathbb{R}. \tag{G.25}$$

So

$$\hat{U} = \xi x^4 + Bx^3 + Cx^2 + Dx + E, \qquad B, C, D, E \in \mathbb{R}. \tag{G.26}$$

Then we use the boundary conditions: $\hat{y}(0) = 0$ yields $E = 0$, $\partial_x \hat{y}(0) = 0$ yields $D = 0$, $\partial^3_{xxx}\hat{y}(L) = 0$ gives $B = -4L\xi$ and $\partial^2_{xx}\hat{y}(L) = 0$ gives $C = 6L^2\xi$. For $x \in [0,1]$, it follows that:

$$U = -\Big(\frac{\rho\hat{g}}{24EK^2}\Big)x^4 + \Big(\frac{L\rho\hat{g}}{6EK^2}\Big)x^3 - \Big(\frac{L^2\rho\hat{g}}{4EK^2}\Big)x^2. \tag{G.27}$$

Consequently, this results in a constant in the difference equations which makes every equation of motion for each specific node nonlinear with $-g$, except for node 1 as this node is clamped. Hence the new matrix-vector equation for the stationary rod will look as follows:

$$\begin{bmatrix} 6 & 0 & 2 & 0 & 0 & 0 & 0 & \dots & 0 \\ -4 & 0 & -4 & 1 & 0 & 0 & 0 & \dots & 0 \\ 1 & -4 & 6 & -4 & 1 & 0 & 0 & \dots & 0 \\ 0 & 1 & -4 & 6 & -4 & 1 & 0 & \dots & 0 \\ \vdots & \vdots & \vdots & \vdots & \vdots & \vdots & \vdots & \ddots & 0 \\ 0 & \dots & 0 & 1 & -4 & 6 & -4 & 1 & 0 \\ 0 & \dots & 0 & 0 & 1 & -4 & 6 & -4 & 1 \\ 0 & \dots & 0 & 0 & 0 & 1 & -4 & 5 & -2 \\ 0 & \dots & 0 & 0 & 0 & 2 & -2 & -3 & 0 \end{bmatrix} \vec{\omega} = h^4 \begin{bmatrix} 0 \\ -\frac{\rho\hat{g}}{EK^2} \\ -\frac{\rho\hat{g}}{EK^2} \\ -\frac{\rho\hat{g}}{EK^2} \\ \vdots \\ -\frac{\rho\hat{g}}{EK^2} \\ -\frac{\rho\hat{g}}{EK^2} \\ -\frac{\rho\hat{g}}{EK^2} \\ -\frac{\rho\hat{g}}{EK^2} \end{bmatrix}. \tag{G.28}$$

H The stationary two dimensional finite element method

The stationary equation of motion for a thin plate using classical Kirchhoff theory reads:

$$B_{xx}\frac{\partial^4 U}{\partial x^4} + 2B_{xy}\frac{\partial^4 U}{\partial x^2 \partial y^2} + B_{yy}\frac{\partial^4 U}{\partial y^4} + \rho g = 0. \tag{H.1}$$

For some $(i,j) \in \Omega_{num}$, this is discretised to:

$$\begin{aligned} &B_{xx}\frac{\omega_{i+2,j} - 4\omega_{i+1,j} + 6\omega_{i,j} - 4\omega_{i-1,j} + \omega_{i-2,j}}{h^4} \\ +&2B_{xy}\frac{\omega_{i+1,j+1} - 2\omega_{i,j+1} + \omega_{i-1,j+1}}{h^4} \\ +&2B_{xy}\frac{-2\omega_{i+1,j} + 4\omega_{i,j} - 2\omega_{i-1,j}}{h^4} \\ +&2B_{xy}\frac{\omega_{i+1,j-1} - 2\omega_{i,j-1} + \omega_{i-1,j-1}}{h^4} \\ &+B_{yy}\frac{\omega_{i,j+2} - 4\omega_{i,j+1} + 6\omega_{i,j} - 4\omega_{i,j-1} + \omega_{i,j-2}}{h^4} = -f_{i,j}. \end{aligned} \tag{H.2}$$

Suppose the plate is clamped at $x = 0$ and free everywhere else on the boundary. The following conditions are then, also completely analogous to the one dimensional problem, given by:

$$\omega_{0,j} = 0, \qquad \frac{\omega_{2,j} - \omega_{0,j}}{h^2} = 0, \tag{H.3}$$

$$\frac{\omega_{n+2,j} - 2\omega_{n+1,j} + \omega_{n,j}}{h^2} = 0, \qquad \frac{-\omega_{n+3,j} + \omega_{n+2,j} + 2\omega_{n+1,j} - 2\omega_{n,j} - \omega_{n-1,j} + \omega_{n-2,j}}{4h^3} = 0, \tag{H.4}$$

$$\frac{\omega_{i,2} - 2\omega_{i,1} + \omega_{i,0}}{h^2} = 0, \qquad \frac{\omega_{i,-1} - \omega_{i,0} - 2\omega_{i,1} + 2\omega_{i,2} + \omega_{i,3} - \omega_{i,4}}{4h^3} = 0, \tag{H.5}$$

$$\frac{\omega_{i,m+2} - 2\omega_{i,m+1} + \omega_{i,m}}{h^2} = 0 \text{ and} \qquad \frac{-\omega_{i,m+3} + \omega_{i,m+2} + 2\omega_{i,m+1} - 2\omega_{i,m} - \omega_{i,m-1} + \omega_{i,m-2}}{4h^3} = 0, \tag{H.6}$$

for $(i,j) \in \Omega_{num}$. Note that, for the free boundaries at $x = n$ and $y = m$, the backwards difference equation is applied once whereafter the central difference equation is used twice. For the free end at $y = 0$, the forward difference equation is used once, then the central difference equation is used twice.

At $\partial\Omega_{num}$, we use Equation H.3-H.6 to obtain:

$$\begin{aligned} &B_{xx}\frac{2\omega_{3,j} + 6\omega_{1,j}}{h^4} - 4B_{xy}\frac{\omega_{1,j+1}}{h^4} + 8B_{xy}\frac{\omega_{1,j}}{h^4} - 4B_{xy}\frac{\omega_{1,j-1}}{h^4} \\ &+B_{yy}\frac{\omega_{1,j+2} - 4\omega_{1,j+1} + 6\omega_{1,j} - \omega_{1,j-1} + \omega_{i,j-2}}{h^4} = -f_{1,j}, \end{aligned} \tag{H.7}$$

where $i = 1$ and $j \in \{3, 4, ..., m-2, m-1\}$,

$$\begin{aligned} &B_{xx}\frac{\omega_{4,j} - 4\omega_{3,j} - 4\omega_{1,j}}{h^4} \\ +&2B_{xy}\frac{\omega_{3,j+1} + \omega_{1,j+1}}{h^4} \\ +&2B_{xy}\frac{-2\omega_{3,j} - 2\omega_{1,j}}{h^4} \\ +&2B_{xy}\frac{\omega_{3,j-1} + \omega_{1,j-1}}{h^4} = -f_{2,j}, \end{aligned} \tag{H.8}$$

where $i = 2$ and $j \in \{3, 4, ..., m-2, m-1\}$,

$$
\begin{aligned}
&B_{xx}\frac{-2\omega_{n+1,j}+5\omega_{n,j}-4\omega_{n-1,j}+\omega_{n-2,j}}{h^4}\\
+&2B_{xy}\frac{\omega_{n+1,j+1}-2\omega_{n,j+1}+\omega_{n-1,j+1}}{h^4}\\
+&2B_{xy}\frac{-2\omega_{n+1,j}+4\omega_{n,j}-2\omega_{n-1,j}}{h^4}\\
+&2B_{xy}\frac{\omega_{n+1,j-1}-2\omega_{n,j-1}+\omega_{n-1,j-1}}{h^4}\\
+&B_{yy}\frac{-2\omega_{n,j+1}+5\omega_{n,j}-4\omega_{n,j-1}+\omega_{n,j-2}}{h^4}=-f_{n,j},
\end{aligned}
\tag{H.9}
$$

where $j \in \{3,4,...,m-2,m-1\}$,

$$
\begin{aligned}
&B_{xx}\frac{2\omega_{n+1,j}-3\omega_{n,j}+\omega_{n-2,j}}{h^4}\\
+&B_{yy}\frac{-2\omega_{n+1,j+1}+5\omega_{n+1,j}-4\omega_{n+1,j-1}+\omega_{n+1,j-2}}{h^4}=-f_{n+1,j},
\end{aligned}
\tag{H.10}
$$

where $j \in \{3,4,...,m-2,m-1\}$,

$$
\begin{aligned}
&B_{xx}\frac{\omega_{i+2,1}-4\omega_{i+1,1}+6\omega_{i,1}-4\omega_{i-1,1}+\omega_{i-2,1}}{h^4}\\
+&B_{yy}\frac{\omega_{i,4}-35\omega_{i,2}+2\omega_{i,1}}{h^4}=-f_{i,1},
\end{aligned}
\tag{H.11}
$$

where $i \in \{3,4,...,n-2,n-1\}$

$$
\begin{aligned}
&B_{xx}\frac{\omega_{i+2,2}-4\omega_{i+1,2}+6\omega_{i,2}-4\omega_{i-1,2}+\omega_{i-2,2}}{h^4}\\
+&2B_{xy}\frac{\omega_{i+1,3}-2\omega_{i,3}+\omega_{i-1,3}}{h^4}\\
+&2B_{xy}\frac{-2\omega_{i+1,2}+4\omega_{i,2}-2\omega_{i-1,2}}{h^4}\\
+&2B_{xy}\frac{\omega_{i+1,1}-2\omega_{i,1}+\omega_{i-1,1}}{h^4}\\
+&B_{yy}\frac{\omega_{i,4}-4\omega_{i,3}+5\omega_{i,2}-2\omega_{i,1}}{h^4}=-f_{i,2},
\end{aligned}
\tag{H.12}
$$

where $i \in \{3,4,...,n-2,n-1\}$

$$
\begin{aligned}
&B_{xx}\frac{-2\omega_{i,m+1}+5\omega_{i,m}-4\omega_{i,m-1}+\omega_{m-2,j}}{h^4}\\
+&2B_{xy}\frac{\omega_{i+1,m+1}-2\omega_{i+1,m}+\omega_{i+1,m-1}}{h^4}\\
+&2B_{xy}\frac{-2\omega_{i,m+1}+4\omega_{i,m}-2\omega_{i,m-1}}{h^4}\\
+&2B_{xy}\frac{\omega_{i-1,m+1}-2\omega_{i-1,m}+\omega_{i-1,m-1}}{h^4}\\
+&B_{yy}\frac{\omega_{i+2,m}-4\omega_{i+1,m}+6\omega_{i,m}-4\omega_{i-1,m}+\omega_{i-2,m}}{h^4}=-f_{i,m}.,
\end{aligned}
\tag{H.13}
$$

for $i \in \{3,4,...,n-2,n-1\}$,

$$
\begin{aligned}
&B_{xx}\frac{2\omega_{i,m+1}-3\omega_{i,m}+\omega_{i,m-2}}{h^4}\\
+&B_{yy}\frac{\omega_{i+2,m+1}-4\omega_{i+1,m+1}+6\omega_{i,m+1}-4\omega_{i-1,m+1}+\omega_{i-2,m+1}}{h^4}=f_{i,m+1},
\end{aligned}
\tag{H.14}
$$

where $i \in \{3,4,...,n-2,n-1\}$,

$$
B_{xx}\frac{2\omega_{3,1}+6\omega_{1,1}}{h^4}+B_{yy}\quad\frac{\omega_{1,4}-3\omega_{1,2}+2\omega_{1,1}}{h^4}=-f_{1,1},
\tag{H.15}
$$

where $(i,j)=(1,1)$,

$$\begin{aligned} B_{xx}\frac{2\omega_{3,2}+6\omega_{1,2}}{h^4}-4B_{xy}\frac{\omega_{1,3}}{h^4}+8B_{xy}\frac{\omega_{1,2}}{h^4}-4B_{xy}\frac{\omega_{1,1}}{h^4} \\ +B_{yy}\frac{\omega_{1,4}-4\omega_{1,3}+5\omega_{1,2}-2\omega_{1,1}}{h^4}=-f_{1,2}, \end{aligned} \tag{H.16}$$

where $(i,j)=(1,2)$,

$$\begin{aligned} B_{xx}\frac{2\omega_{3,m}+6\omega_{1,m}}{h^4}-4B_{xy}\frac{\omega_{1,m+1}}{h^4}+8B_{xy}\frac{\omega_{1,m}}{h^4}-4B_{xy}\frac{\omega_{1,m-1}}{h^4} \\ +B_{yy}\frac{-2\omega_{1,m+1}+5\omega_{1,m}-\omega_{1,m-1}+\omega_{i,m-2}}{h^4}=-f_{1,m}, \end{aligned} \tag{H.17}$$

where $(i,j)=(1,m)$,

$$\begin{aligned} B_{xx}\frac{2\omega_{3,m+1}+6\omega_{1,m+1}}{h^4} \\ +B_{yy}\frac{2\omega_{1,m+1}-3\omega_{1,m}+\omega_{i,m-2}}{h^4}=-f_{1,m+1}, \end{aligned} \tag{H.18}$$

where $(i,j)=(1,m+1)$,

$$B_{xx}\frac{\omega_{4,1}-4\omega_{3,1}-4\omega_{1,1}}{h^4}=-f_{i,1}, \tag{H.19}$$

for $(i,j)=(2,1)$,

$$\begin{aligned} B_{xx}\frac{\omega_{4,2}-4\omega_{3,2}-4\omega_{1,2}}{h^4} \\ +2B_{xy}\frac{\omega_{3,3}+\omega_{1,3}}{h^4} \\ +2B_{xy}\frac{-2\omega_{3,2}-2\omega_{1,2}}{h^4} \\ +2B_{xy}\frac{\omega_{3,1}+\omega_{1,1}}{h^4}=-f_{i,2}, \end{aligned} \tag{H.20}$$

where $(i,j)=(2,2)$,

$$\begin{aligned} B_{xx}\frac{\omega_{4,m}-4\omega_{3,m}-4\omega_{1,m}}{h^4} \\ +2B_{xy}\frac{\omega_{3,m+1}+\omega_{1,m+1}}{h^4} \\ +2B_{xy}\frac{-2\omega_{3,m}-2\omega_{1,m}}{h^4} \\ +2B_{xy}\frac{\omega_{3,m-1}+\omega_{1,m-1}}{h^4}=-f_{2,m}, \end{aligned} \tag{H.21}$$

where $(i,j)=(2,m)$,

$$B_{xx}\frac{\omega_{4,m+1}-4\omega_{3,m+1}-4\omega_{1,m+1}}{h^4}=-f_{2,m+1}, \tag{H.22}$$

where $(i,j)=(2,m+1)$,

$$\begin{aligned} B_{xx}\frac{-2\omega_{n+1,1}+5\omega_{n,1}-4\omega_{n-1,1}+\omega_{n-2,1}}{h^4} \\ +B_{yy}\frac{\omega_{n,4}-3\omega_{n,2}+2\omega_{n,1}}{h^4}=-f_{n,1}, \end{aligned} \tag{H.23}$$

where $(i,j)=(n,1)$,

$$
\begin{aligned}
&B_{xx}\frac{-2\omega_{n+1,2}+5\omega_{n,2}-4\omega_{n-1,2}+\omega_{n-2,2}}{h^4}\\
+2&B_{xy}\frac{\omega_{n+1,3}-2\omega_{n,3}+\omega_{n-1,3}}{h^4}\\
+2&B_{xy}\frac{-2\omega_{n+1,2}+4\omega_{n,2}-2\omega_{n-1,2}}{h^4}\\
+2&B_{xy}\frac{\omega_{n+1,1}-2\omega_{n,1}+\omega_{n-1,1}}{h^4}\\
+&B_{yy}\frac{\omega_{n,4}-4\omega_{n,3}+5\omega_{n,2}-2\omega_{n,1}}{h^4}=f_{n,2},
\end{aligned}
\tag{H.24}
$$

where $(i,j)=(n,2)$,

$$
\begin{aligned}
&B_{xx}\frac{-2\omega_{n+1,m}+5\omega_{n,m}-4\omega_{n-1,m}+\omega_{n-2,m}}{h^4}\\
+2&B_{xy}\frac{\omega_{n+1,m+1}-2\omega_{n,m+1}+\omega_{n-1,m+1}}{h^4}\\
+2&B_{xy}\frac{-2\omega_{n+1,m}+4\omega_{n,m}-2\omega_{n-1,m}}{h^4}\\
+2&B_{xy}\frac{\omega_{n+1,m-1}-2\omega_{n,m-1}+\omega_{n-1,m-1}}{h^4}\\
+&B_{yy}\frac{-2\omega_{n,m+1}+5\omega_{n,m}-4\omega_{n,m-1}+\omega_{n,m-2}}{h^4}=f_{n,m},
\end{aligned}
\tag{H.25}
$$

where $(i,j)=(n,m)$,

$$
\begin{aligned}
&B_{xx}\frac{-2\omega_{n+1,m+1}+5\omega_{n,m+1}-4\omega_{n-1,m+1}+\omega_{n-2,m+1}}{h^4}\\
+&B_{yy}\frac{2\omega_{n,m+1}-3\omega_{n,m}+\omega_{n,m-2}}{h^4}=f_{n,m+1},
\end{aligned}
\tag{H.26}
$$

where $(i,j)=(n,m+1)$,

$$
\begin{aligned}
&B_{xx}\frac{2\omega_{n+1,1}-3\omega_{n,1}+\omega_{n-2,1}}{h^4}\\
+&B_{yy}\frac{\omega_{n+1,4}-3\omega_{n+1,2}+2\omega_{n+1,1}}{h^4}=-f_{n+1,1},
\end{aligned}
\tag{H.27}
$$

where $(i,j)=(n+1,1)$,

$$
\begin{aligned}
&B_{xx}\frac{2\omega_{n+1,2}-3\omega_{n,2}+\omega_{n-2,2}}{h^4}\\
+&B_{yy}\frac{\omega_{n+1,4}-4\omega_{n+1,3}+5\omega_{n+1,2}-2\omega_{n+1,1}}{h^4}=-f_{n+1,2},
\end{aligned}
\tag{H.28}
$$

where $(i,j)=(n+1,2)$

$$
\begin{aligned}
&B_{xx}\frac{2\omega_{n+1,m}-3\omega_{n,m}+\omega_{n-2,m}}{h^4}\\
+&B_{yy}\frac{-2\omega_{n+1,m+1}+5\omega_{n+1,m}-4\omega_{n+1,m-1}+\omega_{n+1,m-2}}{h^4}=-f_{n+1,m},
\end{aligned}
\tag{H.29}
$$

where $(i,j)=(n+1,m)$ and

$$
\begin{aligned}
&B_{xx}\frac{2\omega_{n+1,m+1}-3\omega_{n,m+1}+\omega_{n-2,m+1}}{h^4}\\
+&B_{yy}\frac{2\omega_{n+1,m+1}-3\omega_{n+1,m}+\omega_{n+1,m-2}}{h^4}=-f_{n+1,j},
\end{aligned}
\tag{H.30}
$$

where $(i,j)=(n+1,m+1)$. Now, we transform this to a single digit index α. An example for all the interior nodes is given below:

$$
\begin{aligned}
&B_{xx}\frac{\omega_{\alpha+2}-4\omega_{\alpha+1}+6\omega_{\alpha}-4\omega_{\alpha-1}+\omega_{\alpha-2}}{h^4}\\
+2&B_{xy}\frac{\omega_{\alpha+n+1}-2\omega_{\alpha+n}+\omega_{\alpha+n-1}}{h^4}\\
+2&B_{xy}\frac{-2\omega_{\alpha+1}+4\omega_{\alpha}-2\omega_{\alpha-1}}{h^4}\\
+2&B_{xy}\frac{\omega_{\alpha-n+1}-2\omega_{\alpha-n}+\omega_{\alpha-n-1}}{h^4}\\
+&B_{yy}\frac{\omega_{\alpha+2n}-4\omega_{\alpha+n}+6\omega_{\alpha}-4\omega_{\alpha-n}+\omega_{\alpha-2n}}{h^4}=f_{\alpha}.
\end{aligned}
\tag{H.31}
$$

However, translating all the boundary conditions with two indices to boundary conditions with one index is unnecessary as the notation gets increasingly more difficult. Instead, in the implementation of the method of lines, looping over all α's to implement the correct difference equations for each grid point yields exactly the same as looping over all i's and j's in a nested loop. The implementation only needs to account for that the difference between any two grid points $\alpha(i,j)-\alpha(i,j+1)=n+1$.

As in the one dimensional case, the non-linear terms are collected in f_α. It follows that $f_\alpha=\rho g$ for all $\alpha\in\{1,2,...,(n+1)(m+1)\}$. We can now compare the results to those we found analytically.